

学位論文

Wino dark matter searches in the future

(将来実験におけるウィーノ暗黒物質の検証)

平成 27年 12月 博士(理学)申請

東京大学大学院理学系研究科
物理学専攻

市川 幸史

Abstract

In this thesis, we comprehensively study the future detection of the wino dark matter. While the existence of the $\mathcal{O}(1)$ TeV wino dark matter is strongly supported by the well-motivated high scale SUSY models, it is not clear whether the heavy wino can be discovered/excluded in the future. To test the future detectability, we robustly investigate the potential of collider search and indirect detection. For collider search, we estimate the impact of the indirect search by lepton colliders where the loop contribution of the dark matter is probed through the standard model channels. The likelihood analysis including the realistic systematic errors reveals that 1 TeV center of mass energy can probe up to 650–750 GeV wino through the channel of the standard model fermion pair production. The future sensitivity reach of the gamma-ray observation of the dwarf spheroidal galaxies is also studied. Under a realistic and conservative estimation, the sensitivity reach will be expanded to 800–1000 GeV within a ten years observation. We also show the importance of the dark matter halo estimation for the dwarf galaxies. Under the precise halo estimation, the gamma-ray observation can cover the entire wino parameter region. Finally, based on the motivation above, we test the future potential of the dark matter halo estimation by considering the future kinematical survey of the member stars of the dwarf spheroidal galaxies. Here, we clarify the hidden systematic biases in the halo estimation and especially consider the treatment of the foreground contamination bias, which remains even for the future observation. It is found that the future observation will provide more than twice kinematical data, including less than 5% foreground contamination. However, the study also shows that this contamination significantly biases the halo estimation, which causes the overestimation of the gamma-ray sensitivity by factors of three. We propose a new likelihood function which include the foreground effect and show that the contamination is efficiently eliminated under the new method.

Contents

1	Introduction	3
2	Review on the high scale SUSY scenario	6
2.1	Supersymmetry	6
2.2	High scale SUSY	7
2.3	Mass spectrum	9
3	Properties of wino dark matter	11
3.1	Lagrangian	11
3.2	Annihilation cross section	12
3.3	Scattering cross section	14
3.4	Thermal relic	16
4	Current limits	18
4.1	Collider	18
4.2	Direct detection	20
4.3	Indirect detection	21
4.3.1	dSph	22
4.3.2	CMB	24
4.3.3	BBN	25
4.4	Summary of the current limits	26
5	Future constraints from collider searches	27
5.1	Review	27
5.2	Loop Corrections	28
5.3	Analysis method and detector performance	32
5.4	Results	33
5.5	Potential of future lepton colliders with large \sqrt{s}	36
5.6	Conclusion	37
6	Future constraints from indirect detections	39
6.1	Flux formula	40
6.2	Astrophysical factor	40
6.3	Backgrounds	43
6.4	Detector capabilities	45
6.5	Validating our method	49

6.6	Expected future limit	50
6.7	Conclusion	54
7	Impact of the dSphs survey in the future	54
7.1	Astrophysical factor revisited	55
7.2	Analysis	57
7.2.1	Dark Matter halo and stellar distribution	58
7.2.2	Mock dSphs	58
7.2.3	Spectrograph	60
7.2.4	Cut	61
7.2.5	Velocity dispersion	62
7.2.6	Likelihood	63
7.3	Results	64
7.4	Conclusion	67
8	Summary	68
	Appendices	70
	Appendix A Jeans equation	70
A.1	Boltzmann equation	70
A.2	Projection	72
A.3	dSph Case	73
	Appendix B Mock data of dSphs	73
	Appendix C Foreground Distribution	75

1 Introduction

In July 2012, an historical milestone has been marked by the large hadron collider (LHC) experiments [1, 2]. The discovery of higgs boson is one of the greatest triumphs of the standard model theory (SM), which have led to the Nobel Prize in 2013. Nevertheless, it is not easy to apply this framework at high energy scale as the fundamental theory. One critical reason is that in the SM framework, the higgs boson mass quadratically diverges by the radiative correction, which requires more than $\mathcal{O}(10^{30})$ parameter tuning to obtain the electroweak scale mass. Moreover, the theory does not contain the dark matter candidate, while the existence of the dark matter is solidly confirmed by various observations such as the dynamics of the clusters [3], rotation curves of the galaxies [4, 5] and gravitational lensing [6, 7, 8, 9] as well as the global fit of the Cosmic Microwave Background (CMB), Large Scale Structure (LSS), and Supernovae (SNs) observations [10].

Supersymmetric extension of SM (SUSY) is one of the most attractive beyond standard model candidate [11, 12]. The model cancels the higgs quadratic divergence by introducing superpartners of the SM particles (sparticles) and can contain the dark matter candidate at the same time. Moreover, it predicts that the gauge coupling constants are unified at a high energy scale.

Mass spectrum of the sparticles reflects the breaking scale of the SUSY and it is pointed out that higgs mass provides a striking hint to this mass scale [13, 14, 15, 16]. In the minimal SUSY extension of the SM (MSSM) framework, the tree level mass of higgs boson is less than Z boson mass and therefore the sparticle mass can be inferred from the loop contribution required to achieve the observed higgs mass.

A great impact is therefore brought by the fact that the higgs mass is heavy (126 GeV), which indicates that the typical sparticle mass can be much greater than $\mathcal{O}(1)$ TeV [17, 18]. In fact, such a high scale SUSY is compatible with null-signal results at the current collider experiment, ameliorating the dangerous SUSY contributions to the flavor-changing neutral current (FCNC) processes.

On the other hand, however, if the dark matter is the member of MSSM, the preferred mass region is $\lesssim \mathcal{O}(1)$ TeV otherwise its annihilation rate is suppressed and the mass density becomes inconsistent with the observation [10]. This fact seems to contradict to the typical sparticle mass scale required above.

In fact, this split-type mass spectrum is naturally provided in a class of supergravity mediation scenario where the SUSY breaking sector does not contain any singlets [19, 20]. In these models, the scalar sparticles can obtain the same order

masses as the gravitino via tree level supergravity interactions. On the other hand, because of the lack of the singlet field, gaugino masses are dominated by the anomaly mediated contributions [19, 21], by which the masses are one-loop suppressed compared to the scalar sparticles. ^{#1} This one-loop suppression of the gaugino mass naturally gives the splitting spectrum between gauginos and other sparticles.

One of the most interesting feature of these models is that the almost pure neutral wino (superpartner of $SU(2)_L$ gauge bosons) becomes the lightest supersymmetric particle (LSP) in most parameter space and at the same time, it can be a weakly interacting massive particle (WIMP) dark matter when its mass is of $\mathcal{O}(1)$ TeV [27, 28, 29]. Therefore, the high scale SUSY scenario with appropriate gravitino mass ($\mathcal{O}(10 - 100)$ TeV) can simultaneously obtain the observed higgs boson mass and the good dark matter candidate, wino. ^{#2} Moreover, it is found that the model is also cosmologically preferred: No gauge singlet implies no Polonyi problem [39] and heavy gravitino decays fast enough and does not pollutes Big-Bang Nucleosynthesis (BBN) [27]. For its simplicity and phenomenological consistency, the high scale SUSY scenario is one of the best-motivated SM extensions.

To check the high scale SUSY scenario, the wino dark matter detection is an ideal probe. (The other sparticles are usually beyond the reach in most cases.) ^{#3} The dark matter detection plays key role to test this scenario. There are three major wino dark matter detections: collider search, direct detection, and indirect detection.

Collider experiments provide us with robust constraints on the wino dark matter [41, 42] lower bound. Especially, LHC gives a stringent constraint by using the disappearing track [22, 43, 44, 45, 46] and its sensitivity will be stronger in the future runs [47, 48]. In the near future, although it is difficult to cover all the parameter region due to the limited beam energy, the lepton collider [49, 50] will play a crucial role for the light wino search [51, 52, 53, 54]. In the far future, we can also expect the hadron collider with 100 TeV center of mass energy [55, 56].

Direct detections of the wino dark matter are not hopeful in the near future.

^{#1} Origin of the Higgsino mass, the μ -term, is model dependent even in these models. For example, in the pure gravity mediation model [22, 23, 24] or the minimal split SUSY model [25], the μ -term is generated via a tree level interaction to the R -symmetry breaking sector [26].

^{#2} For discussions related to these models, see also, for example, the following papers [30, 31, 32, 33, 34, 35, 36, 37, 38].

^{#3} Indirect investigations of the heavy scalar sparticles through FCNC processes or electric dipole moments (EDM) of SM particles will play important roles to test some portion of the parameter space [40], though their signals depend highly on physics behind the flavor/CP structure of squarks and sleptons.

Because the interaction between the wino dark matter and a nucleon suppressed at one-loop level, its typical cross section is estimated to be about 10^{-47} cm^2 [57, 58, 59, 60, 61], and it is difficult to reach this sensitivity in the near future.

Indirect detections of the wino dark matter, on the other hand, have quite strong sensitivities because the wino annihilation is enhanced by a non-perturbative effect [62]. While most of the indirect detections suffer from the huge and unclear astrophysical uncertainties, the Milky Way dwarf spheroidal satellite galaxies (dSphs) are considered to be an ideal target because of its clean environment and dense dark matter halo. Current dSph observations have already given stringent constraints [63] and therefore it is important to investigate how it will be in the future, how to improve this sensitivity and of course, how robust it is.

In this thesis, we comprehensively investigate the future detectability of the wino dark matter. For the collider search, we focus on the heavy wino search by lepton colliders, where the mass is above the beam energy. For the indirect detection, we consider the gamma-ray observation of the dSphs and show that the wino can be discovered in the near future as long as we can improve the estimation of the dark matter halos inside the dSphs. Finally, based on the motivation above, we test the future potential of the dark matter halo estimation by considering the future kinematical survey of the member stars of the dwarf spheroidal galaxies. Here, we clarify the hidden systematic biases in the halo estimation and especially consider the treatment of the foreground contamination bias, which remains even for the future observation.

The organization of this thesis is as follows. In the first part, we review the subject of the wino dark matter (Sec. 2-4), while our studies are presented in Sec. 5-7. In Sec. 2, we introduce the high scale SUSY and its mass spectrum. In Sec. 3, the wino dark matter property is overviewed. In Sec. 4, the current constraints on the wino dark matter are summarized. In Sec. 5, the future constraints by the collider are discussed based on our work [54]. Here, we especially focus on the lepton collider search using the indirect probe and provide the precise estimation for the future sensitivity reach. In Sec. 6, we investigate the future potential of the indirect detection referring to our work [64]. The gamma-ray observation of dSphs is intensively investigated and the importance of the halo estimation of the dSphs is shown. In Sec. 7, we discuss the hidden systematics of the halo estimation of the dSphs and provide a new method to eliminate the foreground contamination, which becomes a crucial bias for the future survey. The estimation is performed referring to the capability of the future spectrograph and therefore it also gives a future prospect of

the dSphs halo survey at the same time. Finally, in Sec. 8, we summarize the current and future prospect of the wino dark matter detection.

2 Review on the high scale SUSY scenario

2.1 Supersymmetry

Although SM seems to successfully describe phenomena below the electroweak scale, the framework has a serious problem in higher energy scale. In SM framework, because the mass parameter of bosonic particle is not preserved by the chiral symmetry, the radiative correction to the higgs mass contains a quadratic divergence of the cutoff scale. If the SM is the proper theory at the Planck scale, the higgs bare mass parameter should be tuned so that it cancels the quadratic coupling and provides $\mathcal{O}(10^2)$ GeV observed mass, which requires more than $\mathcal{O}(10^{30})$ tuning. The other important problem is that the SM does not contain the dark matter candidate, while the existence of the dark matter is solidly confirmed by the various observations such as the dynamics of the clusters [3] and galaxies [4, 5], gravity lensing observations [6, 7] (especially, of the bullet clusters [8, 9]) and from the global fit of the CMB, LSS and SNs observation [10].

One of the most attractive approaches is the supersymmetric extension of SM (SUSY) [11, 12]. The supersymmetry imposes symmetry, where the SM fermion (boson) has the corresponding bosonic (fermionic) superpartner with the same quantum numbers. Especially, the minimum SUSY extension of the SM (MSSM) is one of the most attractive beyond-standard-models not only for its simplicity but also for the three prominent features below. First, SUSY can dramatically ameliorate the higgs fine tuning. Thanks to the existence of the superpartners, the SM loop contributions to the higgs mass are cancelled by the loop diagrams of the superpartners because the loop signs differ between the fermion and the boson. The second important aspect is that MSSM has the dark matter candidate. In most of the case, a discrete symmetry (R -symmetry) is imposed on MSSM where the SM particles have $+1$ R -charge while sparticles have -1 . Under the R -symmetry, because LSP cannot decay into lighter SM particles, it can be stable and therefore it is a dark matter candidate if its mass and interaction are appropriate. Finally, once the SUSY is imposed on SM, the renormalization group equations (RGEs) of the gauge coupling constants are modified by the contribution from the sparticles and the gauge coupling constants are eventually unified at the high energy scale ($\mathcal{O}(10^{16})$ GeV), which strongly

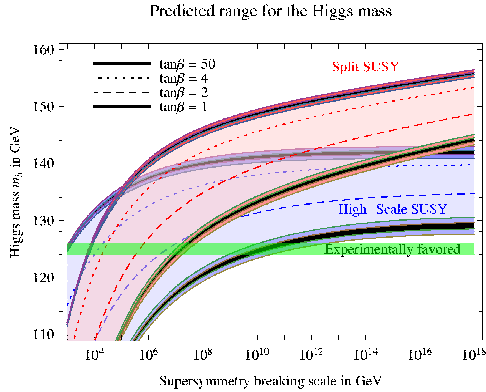


Figure 1: *The relation between the higgs mass and the sfermion masses at two-loop calculation. The figure is from Ref. [17]. In the figure, ‘High-scale SUSY’ assumes that the mass scales of the sfermions and Higgsino are equal to the SUSY breaking scale, and the soft trilinear coupling is small. On the other hand, ‘Split SUSY’ assumes that the mass scale of the supersymmetric scalars are equal to the SUSY breaking scale with the supersymmetric fermions being at the weak scale.*

suggests the existence of the gauge unified theory behind SUSY.

2.2 High scale SUSY

The mass spectrum of the sparticles is closely related to the breaking mechanism of the supersymmetry. Naively speaking, the breaking scale provides a typical scale of the sparticle masses. If the supersymmetry is preserved at a low energy scale, the symmetry predicts the existence of the sparticles with the similar mass as the corresponding SM particles. As current experiments do not find these light sparticles, the supersymmetry breaking should occur above the electroweak scale. Furthermore, the recent results of the hadron collider experiments (no beyond-standard-model signal and the discovery of the higgs boson) provide an important clue to the SUSY mass spectrum. While the former derives the rough expectation that the SUSY breaking scale is at least above $\mathcal{O}(1)$ TeV, the higgs discovery, especially its mass measurement provides more striking hints to the SUSY mass spectrum.

The LHC experiments have found the higgs boson-like excess in July 2012 [1, 2]. The experiments have measured its mass, spin, CP property and couplings and found no deviation from the SM prediction of the higgs boson [65, 66, 67, 68], providing the mass of 126 GeV. On the other hand, in the MSSM framework, the tree level higgs mass is predicted less than Z boson mass, which is enhanced by the heavy sparticle

loops [13, 14, 15, 16]. The higgs mass can be given by #4

$$m_h^2 \sim m_Z^2 \cos \beta_v + \frac{3m_t^4}{4\pi^4 v_h^4} \log \frac{m_{\tilde{t}}^2}{m_t^2}. \quad (1)$$

Here $m_h, m_Z, m_t, m_{\tilde{t}}$ represents the mass of the higgs boson, Z boson, top, and stop respectively. $v_h = 174 \text{ GeV}$ is the vacuum expectation value of the SM-like higgs and $\tan \beta_v$ is the ratio of the vacuum expectation values between up-type and down-type higgs doublet fields.#5 The first term on the left hand side denotes the tree level contribution, while the second term is the stop loop corrections. This mass relation indicates the large stop mass (i.e. large SUSY breaking scale). Higgs mass is computed at two-loop level by Ref. [18, 17], which shows that under $\mathcal{O}(1) \tan \beta_v$, $\mathcal{O}(100) \text{ TeV}$ SUSY breaking scale is required to achieve the 126 GeV higgs mass as shown in Fig. 1. In the figure, ‘High-scale SUSY’ assumes that the mass scales of the sfermions and Higgsino are equal to the SUSY breaking scale, and the soft trilinear coupling is small. On the other hand, ‘Split SUSY’ assumes that the mass scale of the supersymmetric scalars are equal to the SUSY breaking scale with the supersymmetric fermions being at the weak scale.

On the other hand, current dark matter abundance provides us with the mass information of the dark matter. The annihilation cross section of the dark matter is suppressed by $\sim 1/m_{\text{DM}}^2$, where m_{DM} denotes the dark matter mass. If m_{DM} is too large, the relic abundance of the dark matter becomes so large that it contradicts to the current observation [10]. Therefore, if the dark matter is WIMP, the preferred dark matter mass region is found to be $\lesssim \mathcal{O}(1) \text{ TeV}$.

Combining the discussion above, the preferred mass spectrum is found that the most of the sparticles masses are at around $\mathcal{O}(100) \text{ TeV}$ region, while LSP mass is $\mathcal{O}(1) \text{ TeV}$. This split-type SUSY spectrum can be realized by the anomaly mediation SUSY breaking scenario (AMSB) [19, 21]. In the next section, we will introduce this AMSB scenario and its mass spectrum.

#4 There are other corrections from the left-right mixing of stops caused by the Higgsino mass parameter and the soft trilinear coupling. The large left-right mixing term or large $\tan \beta_v$ can reduce the SUSY scale. However, as discussed in the introduction, high scale SUSY scenario is not only suitable for the higgs mass spectrum, but also favored by the dark matter mass, the flavor experiments and cosmology.

#5 For the anomaly cancellation and structure of the Yukawa terms, MSSM requires two types of higgs doublet which couples to the up-type and down-type fermion respectively. In this thesis we call former (latter) one up-type (down-type) Higgs.

2.3 Mass spectrum

In the previous section, we introduce the motivation of the high scale split SUSY scenario. Here, we briefly review how the mass spectrum is obtained in the AMSB framework. At the end of the section, wino dark matter is introduced as the most important probe of the high scale SUSY scenario.

The construction can be started by considering the models with supergravity mediation without any singlet fields in the SUSY breaking sector. Under the supergravity, scalar bosons generically obtain their soft-SUSY breaking mass terms via tree-level interactions in supergravity. With a generic Kähler potential, all the masses are expected to be of the order of the gravitino mass, which is denoted by $m_{3/2}$. Origins of the Higgsino mass parameter μ and the holomorphic bilinear soft terms of scalars (B terms) are model dependent, and we assume that they are of the order of the gravitino mass in following discussions.

For the gaugino masses, on the contrary, tree-level contributions in supergravity are extremely suppressed because of the absence of a singlet SUSY breaking field. At one-loop level, however, the gaugino masses are generated without such a singlet via anomaly mediated contributions [19, 21].^{#6} In addition, electroweak gauginos also receive other contributions from the heavy Higgsino threshold effect at one-loop level [19, 28]. Putting these one-loop contributions together, the gaugino masses at the energy scale of $\mathcal{O}(m_{3/2})$ are given by

$$M_1 = g_1^2/(16\pi^2)(33/5)(m_{3/2} + T/11) , \quad (2)$$

$$M_2 = g_2^2/(16\pi^2)(m_{3/2} + T) , \quad (3)$$

$$M_3 = g_3^2/(16\pi^2)(-3) m_{3/2} , \quad (4)$$

where subscripts ‘1, 2, 3’ correspond to the SM gauge groups $U(1)_Y$, $SU(2)_L$, and $SU(3)_c$ with g_1 , g_2 , and g_3 being corresponding gauge coupling constants, respectively. The terms proportional to $m_{3/2}$ denote the anomaly mediated contributions, while those proportional to T are the Higgsino threshold contributions:

$$T \equiv \mu \sin 2\beta_v \frac{m_A^2}{(|\mu|^2 - m_A^2)} \ln \frac{|\mu|^2}{m_A^2} . \quad (5)$$

Here, m_A denotes the mass of the pseudoscalar higgs boson. As shown in Ref. [24], typical values of $\tan \beta_v$ and T are predicted to be $\mathcal{O}(1)$ and $\mathcal{O}(m_{3/2})$, respectively, when μ and B terms are $\mathcal{O}(m_{3/2})$. As a result, we immediately find that the gaugino

^{#6} Trilinear couplings are also suppressed at tree-level in the absence of a singlet SUSY breaking field and they are dominated by anomaly mediated contributions.

masses are in hundreds GeV to a TeV range when the gravitino mass is fixed to be $\mathcal{O}(10\text{--}100)$ TeV, which corresponds to the favored SUSY breaking scale discussed in the previous section.

By integrating out the heavy particles (i.e. sfermions, Higgsinos and heavy higgs bosons) and taking care of renormalization group running down to the TeV scale, we obtain the low-energy effective lagrangian of the gauginos,

$$\mathcal{L}_{\text{eff}} = \mathcal{L}_{\text{SM}} + \bar{g}i\not{D}\tilde{g} + \bar{b}i\not{D}\tilde{b} + \bar{w}i\not{D}\tilde{w} - \frac{1}{2}(m_{\tilde{g}}\tilde{g}\tilde{g} + m_{\tilde{b}}\tilde{b}\tilde{b} + m_{\tilde{w}}\tilde{w}\tilde{w} + c.c.) + \mathcal{L}_{\text{H.O.}} . \quad (6)$$

Here, \tilde{g} , \tilde{b} , and \tilde{w} represent gluino, bino, and wino fields, respectively (Weyl representation), with \not{D} being their covariant derivatives. The standard model lagrangian is denoted by \mathcal{L}_{SM} . The term $\mathcal{L}_{\text{H.O.}}$ is composed of higher dimensional operators induced by integrating out the heavy fields. Gaugino masses, $m_{\tilde{g}, \tilde{b}, \tilde{w}}$, obtained by solving renormalization group equations with boundary conditions in equation (2)–(4) are given by,

$$m_{\tilde{g}} \simeq 2.5 \times 10^{-2} m_{3/2} (1 - 0.13 \delta_{32} - 0.04 \delta_{\text{SUSY}}) , \quad (7)$$

$$m_{\tilde{b}} \simeq 9.6 \times 10^{-3} (m_{3/2} + T/11) (1 + 0.01 \delta_{\text{SUSY}}) , \quad (8)$$

$$m_{\tilde{w}} \simeq 3.0 \times 10^{-3} (m_{3/2} + T) (1 - 0.04 \delta_{32} + 0.02 \delta_{\text{SUSY}}) . \quad (9)$$

$\delta_{\text{SUSY}} = \ln(M_{\text{SUSY}}/100 \text{ TeV})$ for all the gauginos, while $\delta_{32} = \ln(m_{3/2}/100 \text{ TeV})$ for the gluino and $\delta_{32} = \ln[(m_{3/2} + T)/100 \text{ TeV}]$ for the wino [24].

As can be seen in the above mass formulae, the wino is the LSP unless T is too large compared to $m_{3/2}$. Notice that, if T is too large and the bino is the LSP, such a parameter region has already been phenomenologically excluded, because the bino dark matter would result in too much relic density to be consistent with the observed one. ^{#7} It is also worth noting that the mixing between the bino and the wino caused by the electroweak symmetry breaking is negligibly small, since the Higgsino mass is $\mathcal{O}(m_{3/2})$ and much larger than the gaugino masses. We can therefore safely ignore the existence of the gluino and the bino as well as higher dimensional operators involved in \mathcal{L}_{eff} when physics concerns only the wino dark matter.

^{#7}When wino and the bino masses are highly degenerated, there is a parameter region consistent with the observation with the bino being dark matter. This region can be probed in another way instead of the one discussed in this article. See Ref. [69, 70, 71] for more details.

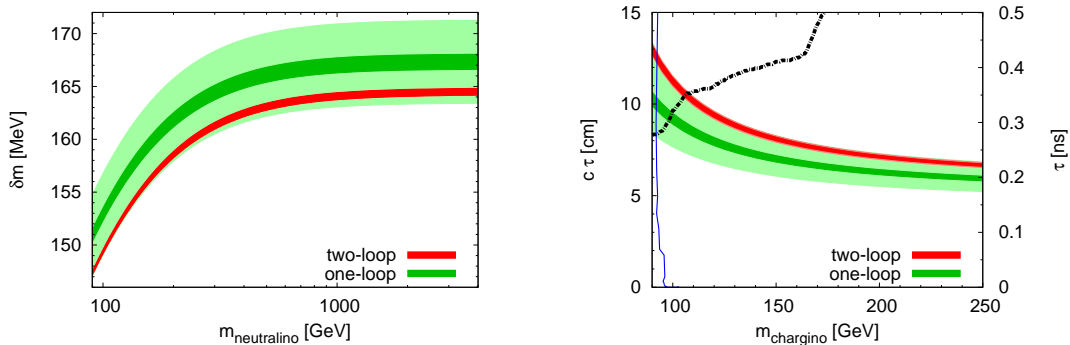


Figure 2: The mass difference between the neutral and charged wino including the two-loop contribution (left panel) and the lifetime of the charged wino (right panel). The figure is from Ref. [72].

3 Properties of wino dark matter

3.1 Lagrangian

By the discussion in the previous section, the effective lagrangian for the dark matter is then simply approximated by

$$\mathcal{L}_{\text{eff}} \simeq \mathcal{L}_{\text{SM}} + \bar{w}i\not{D}w - \frac{1}{2}(m_{\tilde{w}}\tilde{w}\tilde{w} + c.c.) , \quad (10)$$

where \mathcal{L}_{SM} denotes the standard model lagrangian. We note that this effective theory contains only one new physics parameter, $m_{\tilde{w}}$. The wino term in the lagrangian can be rewritten by the neutral Majorana field χ^0 and charged Dirac field χ^- as follows:

$$\begin{aligned} \mathcal{L}_{\text{wino}} &= \mathcal{L}_{\text{wino}}^{\text{kin}} + \mathcal{L}_{\text{wino}}^{\text{int}} \\ \mathcal{L}_{\text{wino}}^{\text{kin}} &= i\bar{\chi}^-\not{\partial}\chi^- - m_{\tilde{w}}\bar{\chi}^-\chi^- + \frac{i}{2}\bar{\chi}^0\not{\partial}\chi^0 - \frac{m_{\tilde{w}}}{2}\bar{\chi}^0\chi^0 \\ \mathcal{L}_{\text{wino}}^{\text{int}} &= -g_2\bar{\chi}^-\not{W}^-\chi^0 - g_2\bar{\chi}^0\not{W}^+\chi^- + g_2\bar{\chi}^-(c_W\not{Z} + s_W\not{A})\chi^- , \end{aligned} \quad (11)$$

Here c_W (s_W) is the cosine (sine) of the Weinberg angle.

The tree level masses of the neutral wino and charged wino are degenerated. The radiative correction resolves this degeneracy and the neutral wino becomes LSP. The one-loop contribution can be written as follows [43].

$$\delta m_{\tilde{w}} = \frac{m_{\tilde{w}}\alpha_2}{4\pi} \int_0^1 dx(2+2x) [\ln f(x, r_W) - c_W^2 \ln f(x, r_Z) - s_W^2 \ln f(x, 0)] , \quad (12)$$

where $\alpha_2 = g_2^2/4\pi$ is the $SU(2)_L$ coupling constant, $\delta m_{\tilde{w}}$ is the mass difference between the charged wino and the neutral wino after the radiative correction, and

we define $f(x, r) \equiv x^2 + (1 - x)r^2$, $r_W \equiv m_W/m_{\tilde{w}}$ and $r_Z \equiv m_Z/m_{\tilde{w}}$. Here m_W denotes the mass of the W boson. The two-loop calculation is done by Ref. [72] (Fig. 2, left panel) and shows that the mass difference is at around 165 MeV when $m_{\tilde{w}} = \mathcal{O}(1)$ TeV.

The small mass difference implies the long lifetime of the charged wino. Most of the heavy charged wino decays into the neutral wino emitting a charged pion. At tree level, the decay width can be given by

$$\Gamma(\chi^\pm \rightarrow \chi^0 \pi^\pm) = \frac{2G_F^2 f_\pi^2 c_1^2}{\pi} \delta m_{\tilde{w}}^3 \sqrt{1 - \frac{m_\pi^2}{\delta m_{\tilde{w}}^2}} \sim 3 \times 10^{-15} \text{GeV} , \quad (13)$$

Here $G_F \sim 1.17 \times 10^{-5} \text{GeV}^{-2}$ is the Fermi coupling constant, and $f_\pi \sim 130 \text{MeV}$ is the π^0 decay constant, and $c_1 \sim 0.97$ is the $u\bar{d}$ component of the Cabibo angle. The sub-leading decay is the leptonic decay with $e^\pm \nu_e$ [73] which can be written by $\Gamma(\chi^\pm \rightarrow \chi^0 e^\pm \nu_e) = 2G_F^2 \delta m_{\tilde{w}}^5 / 15\pi^3$. This decay branch is $\sim 2\%$. Due to the small decay width, the charged wino runs $\sim 5 - 10 \text{cm}$ before the decay (Fig. 2, right panel). The long-lived charged particle can be utilized to identify the wino event identification at the collider searches, which is reviewed in Sec. 4.1.

3.2 Annihilation cross section

This section is devoted to review the wino dark matter annihilation cross section. For the signal flux formula of the indirect detection, we especially focus on the non-relativistic reaction.

The wino dark matter dominantly self-annihilates into W boson pair (WW) through the process with the t -channel exchange of the charged wino. The dark matter can also annihilate into Z boson pair (ZZ), Z boson plus photon ($Z\gamma$), and two photons ($\gamma\gamma$) through one-loop processes. Annihilations into fermion pairs are, on the contrary, suppressed due to angular momentum and CP conservations. When the wino dark matter is much heavier than the weak gauge bosons, exchanging the bosons between incident wino dark matter particles causes long-range forces, which leads to the modification of incident wave functions from the plane-waves. The annihilation cross section is as a result enhanced by a few orders of magnitude compared to the leading one [62], which is called Sommerfeld enhancement. Thanks to this enhancement, the indirect detection is one of the most promising approaches for the wino dark matter discovery.

Calculation of the annihilation cross section can be written by a product of two parts: One is the calculation of perturbative annihilation amplitudes, which is the

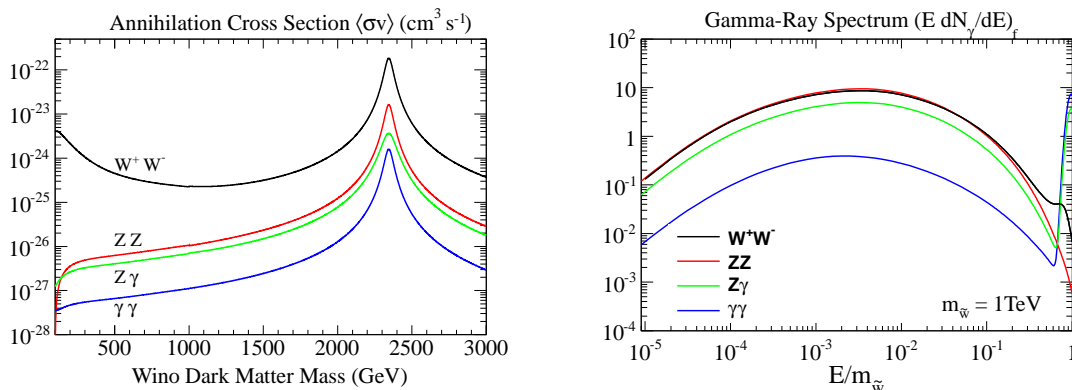


Figure 3: **Left panel:** Annihilation cross sections of the wino dark matter for processes $\chi^0\chi^0 \rightarrow WW, ZZ, Z\gamma,$ and $\gamma\gamma$ as a function of the wino mass [74]. **Right panel:** Normalized fragmentation functions, $E(dN_\gamma/dE)_f$, for final states $f = WW, ZZ, Z\gamma,$ and $\gamma\gamma$ as a function of E in unit of $m_{\tilde{w}}$. Gaussian smearing with $\Delta E/E = 0.1$ was applied.

same as the one obtained in usual perturbation theory (short-distant part). The other is the calculation of enhancement factors caused by the Sommerfeld effect, which is almost one for low mass region while much larger than one for high mass region (long-distant part). The next to leading order calculation ($\mathcal{O}(g_2^6)$) of the short-distant part is performed by Ref. [74] #8 and the resultant annihilation cross sections are shown in the left panel of Fig. 3. In the figure, $\langle\sigma v\rangle$ denotes the product of the annihilation cross section and the relative velocity and the bracket implies the current thermal average. Here, we note that $\langle\sigma v\rangle$ can be well approximated by the value in the vanishing velocity limit as long as $m_{\tilde{w}} v \ll m_{Z,W}$. #9

Weak gauge bosons from the wino dark matter annihilation first decay into quarks, charged leptons, and neutrinos. Once quarks are produced, they are fragmented into various hadrons, eventually producing stable particles such as protons, anti-protons, electrons, positrons, photons, and neutrinos. Photons therefore come as direct annihilation products via processes $Z\gamma$ and $\gamma\gamma$, or as secondary decay products of hadrons (mainly from π^0 decays). As a result, the annihilation produces monochromatic gamma-rays in the direct annihilations, whereas continuous gamma-

#8 For the line gamma-ray channel ($\gamma\gamma, Z\gamma$), this part is computed to next-to-next-to-leading logarithmic order [75]. In this thesis, we do not focus on the line signal search and therefore we use the next leading order calculation of Ref. [74].

#9 There is another region in which we cannot neglect the velocity dependence on σv ; the region where the binding energy of the wino bound state is almost zero. Since this region has already been excluded due to the huge annihilation cross section, we do not discuss it any more.

rays in the second case. The energy distribution of photons from quark fragmentations is usually calculated by a simulation code such as Pythia [76] or HERWIG [77], which includes the effect of QED and QCD final-state radiations. In addition, it has been pointed out in Ref. [78] that the final-state radiations of weak gauge bosons also give sizable contributions to the distribution. The radiations are logarithmically enhanced in their soft and collinear parts, and modify the distribution by a factor of two to ten at the photon energy of $\mathcal{O}(0.1\text{--}10)$ GeV. In this paper, we thus use the energy distribution given by Ref. [79] generated by Pythia 8.135 incorporating the above electroweak corrections. The energy-distribution of photons produced in each dark matter annihilation is summarized in so-called the fragmentation function $(dN_\gamma/dE)_f$, which is shown in the right panel of Fig. 3. Here in order to sketch a realistic photon spectrum, we have applied a Gaussian smearing to the function with the width of $\Delta E/E = 10\%$ (the typical energy resolution of gamma-ray telescopes).

3.3 Scattering cross section

In this section we provide the formulae of the scattering cross section of the wino dark matter and a nucleus based on the discussion in Ref. [61], which is utilized to the direct search reviewed in Sec. 4.2.

The elastic scattering cross section between the dark matter and nucleus can be divided into two parts: the nucleus spin dependent part (SD) and the spin-independent (SI) part. Below, we will focus on the calculation of the SI part because the sensitivity for the SD part is smaller than the SI part and moreover SD part is found to be small for wino dark matter case.

The SI cross section with nucleus is given by

$$\sigma_{\text{SI}} = \frac{4}{\pi} \left(\frac{m_{\tilde{w}} m_X}{m_{\tilde{w}} + m_X} \right)^2 (n_p f_p + n_n f_n)^2, \quad (14)$$

where f_N ($N = p, n$) denotes the effective coupling of wino and nucleon, m_X is the mass of the nucleus, and n_p (n_n) is the number of proton (neutron) in the nucleus. Thanks to the number factor n_p, n_n , the SI cross section for the heavy nucleus can be large.

The effective coupling can be obtained from the effective lagrangian between the wino dark matter, quarks and gluons. The effective lagrangian can be expressed by the two types of the operators as follows [80]:

$$\mathcal{L}_{\text{eff}} = \sum_{i=q,g} C_S^i \mathcal{O}_S^i + \sum_{i=q} \sum_{gj=1,2} C_{T_j}^i \mathcal{O}_{T_j}^i, \quad (15)$$

where $C_S^i, C_{T_j}^i$ denote the coefficients for each operator. We define the scalar operators \mathcal{O}_S^i by

$$\mathcal{O}_S^q \equiv m_q \bar{\chi}^0 \chi^0 \bar{q} q, \quad \mathcal{O}_S^g \equiv \alpha_3 \bar{\chi}^0 \chi^0 G_{\mu\nu}^a G^{a\mu\nu} / \pi, \quad (16)$$

Here, $q, m_q, G_{\mu\nu}^a$ denotes quarks ($q = u, d, s, c, b$), the mass of each quark, and the field strength tensor of the gluon with $SU(3)_c$ index 'a'. α_3 is the strong coupling constant. On the other hand, $\mathcal{O}_{T_j}^i$ is expressed by the twist-2 operator $\mathcal{O}_{\mu\nu}^i$ as follows

$$\mathcal{O}_{T_1}^i \equiv \bar{\chi}^0 i \partial^\mu \gamma^\nu \chi^0 \mathcal{O}_{\mu\nu}^i / m_{\bar{w}}, \quad \mathcal{O}_{T_2}^i \equiv \bar{\chi}^0 (i \partial^\mu) (i \partial^\nu) \chi^0 \mathcal{O}_{\mu\nu}^i / m_{\bar{w}}^2, \quad (17)$$

where each twist-2 operator is defined by $\mathcal{O}_{\mu\nu}^q \equiv i \bar{q} (D_\mu \gamma_\nu + D_\nu \gamma_\mu - g_{\mu\nu} \not{D} / 2) q / 2$, and $\mathcal{O}_{\mu\nu}^g \equiv G_{\mu\rho}^{a\rho} G_{\nu\rho}^a - g_{\mu\nu} G_{\rho\sigma}^a G^{a\rho\sigma} / 4$, respectively.

For the calculation of the scattering cross section, the nucleon matrix elements of the scalar and twist-2 type operator are required. The matrix elements for the quark scalar operator can be expressed by the mass fraction $f_{T_q}^{(N)} \equiv \langle N | m_q \bar{q} q | N \rangle / m_N$, which can be obtained from the lattice simulation [81, 82]. On the other hand, the matrix elements of the gluon scalar operator can be obtained by utilizing the trace anomaly of the energy momentum tensor [83]:

$$\langle N | \frac{\alpha_3}{\pi} G_{\mu\nu}^a G^{a\mu\nu} | N \rangle / m_N = \frac{4\alpha_3^2}{\pi\beta_3} \left[1 - (1 - \gamma_m) \sum_q f_{T_q}^{(N)} \right], \quad (18)$$

where the beta function $\beta_3 \equiv \Lambda d\alpha_3 / d\Lambda$, anomalous dimension $\gamma_m \equiv d \ln(m_q) / d \ln(\Lambda)$ for N_f flavors and N_c colors are given by

$$\beta_3 = \frac{(-11N_c + 2N_f)\alpha_3^2}{6\pi} + \frac{(-17N_c^2 + 5N_c N_f + 3C_F N_f)\alpha_3^3}{12\pi^2}, \quad (19)$$

$$\gamma_m = -\frac{3C_F \alpha_3}{2\pi}. \quad (20)$$

Here $C_F \equiv (N_c^2 - 1) / 2N_c$ is the quadratic Casimir invariant and Λ represents the energy scale of the renormalization group.

On the other hand, the matrix elements of the twist-2 type operator can be expressed by using the particle distribution functions (PDFs):

$$\langle N | \mathcal{O}_{\mu\nu}^q | N \rangle = m_N \left(\frac{p_\mu p_\nu}{m_N^2} - \frac{g_{\mu\nu}}{4} \right) (q_2^{(N)}(\mu) + \bar{q}_2^{(N)}(\mu)), \quad (21)$$

$$\langle N | \mathcal{O}_{\mu\nu}^G | N \rangle = -m_N \left(\frac{p_\mu p_\nu}{m_N^2} - \frac{g_{\mu\nu}}{4} \right) g_2^{(N)}(\mu). \quad (22)$$

Here p is the four momentum of the nucleon and we define the second moment of PDFs in the nucleon N at energy scale Λ by $P_2^{(N)}(\Lambda) = \int_0^1 dx x P^{(N)}(x, \Lambda)$ where

P denotes quark q , anti-quark \bar{q} and gluon g . The calculation in Ref. [61] uses the next leading order PDFs provided by CTEQ-Jefferson Lab collaboration [84] at the energy scale of $\Lambda = m_Z$.

In summary, by using the coefficients above, the SI coupling of wino and nucleon f_N can be expressed as follows:

$$\begin{aligned} \frac{f_N}{m_N} = & \sum_q C_S^q f_{T_q}^{(N)} + \frac{4\alpha_3^2}{\pi\beta_3(\alpha_3)} C_S^g (1 - (1 - \gamma_m) f_{T_q}^{(N)}) \\ & + \frac{3}{4} \sum_q \sum_{j=1,2} C_{T_j}^q (q_2^{(N)} + \bar{q}_2^{(N)}) + \frac{3}{4} \sum_{j=1,2} C_{T_j}^g g_2^{(N)}. \end{aligned} \quad (23)$$

The Wilson coefficients $C_S^i, C_{T_j}^i$ are obtained from the 4 point function of 2 winos and qq or gg . For the wino case, it is pointed out that the loop contributions are not suppressed by the wino mass and it can be large [85]. However, at the same time, an accidental cancellation between qq and gg diagram reduces the cross section. The leading order calculation has been presented by [57, 58, 59, 60] and shown $\sigma_{\text{SI}} \sim 10^{-47} \text{cm}^2$. However, recent study points out that the leading order calculation is largely affected by the uncertainty coming from the higher order correction of the Wilson coefficients, rather than that from the nucleon matrix elements [86]. The next leading order calculation in α_3/π is performed in Ref. [61]. They provide

$$\sigma_{\text{SI}}^p = 2.3 \begin{matrix} +0.2 \\ -0.3 \end{matrix} \begin{matrix} +0.5 \\ -0.4 \end{matrix} \times 10^{-47} \text{ cm}^2, \quad (24)$$

in the limit of a large wino mass. Here, the first and second errors show the contributions from the perturbative calculation and input parameters respectively.

The SD cross section is also calculated and found to be 10^{-46}cm^2 for the pure wino case [60]. Current experiments reach a SD cross section of 10^{-39}cm^2 and the sensitivities will be $\lesssim 10^{-43} \text{cm}^2$ in the future. Therefore, for the pure wino case, the SD direct detection requires further breakthroughs.

3.4 Thermal relic

As the dark matter, the wino abundance should be consistent with the current observation. Naively speaking, the heavier dark matter has smaller annihilation cross section (without considering the non-perturbative effect) and therefore the discussion on the dark matter production in the early universe provides the important constraints on the wino mass, especially on its upper bound.

Here, we consider two possibilities of the production process: The conventional thermal production and the non-thermal production from the late-time decay of

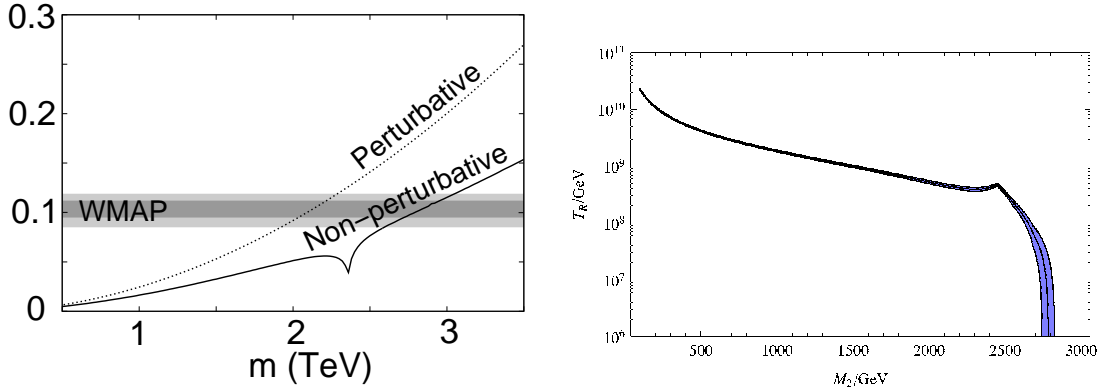


Figure 4: **Left panel:** The relation between the thermal abundance and the wino mass. **Right panel:** The reheating temperature required by the current dark matter abundance. While the low reheating temperature is required so that the thermal wino dominates, the temperature can be high ($\mathcal{O}(10^9)$ GeV) if we consider the non-thermal production. The figure is from [29] (left) and [23] (right).

gravitinos into winos. The thermal contribution to the wino relic abundance, $\Omega_{\text{TH}}h^2$, has been estimated in Ref. [29, 87], where all coannihilation processes as well as the Sommerfeld effect were taken into account. It then turns out that $\Omega_{\text{TH}}h^2$ explains the observed abundance when $m_{\tilde{w}}$ is 2.8–2.9 TeV as shown in the left panel of Fig. 4. The non-thermal contribution to the abundance, $\Omega_{\text{NT}}h^2$, on the other hand, depends not only on the wino mass $m_{\tilde{w}}$ but also on the reheating temperature T_R after inflation. When the temperature is higher, the more gravitino is produced, and hence, the contribution is larger. $\Omega_{\text{NT}}h^2$ is quantitatively estimated to be $\Omega_{\text{NT}}h^2 \simeq 0.16 (m_{\tilde{w}}/300 \text{ GeV}) (T_R/10^{10} \text{ GeV})$ [27, 28].

As a minimal setup, we assume that the wino dark matter produced either thermally or non-thermally by the gravitino decay explains the observed dark matter density, i.e. $\Omega_{\text{TH}}h^2 + \Omega_{\text{NT}}h^2 = \Omega_{\text{DM}}^{(\text{obs.})}h^2$, and assume no entropy production in the universe at the later time. For $m_{\tilde{w}} \simeq 2.8$ –2.9 TeV, the reheating temperature is required to be low so that the thermally produced wino dominates the dark matter density. For a lighter wino, on the other hand, the non-thermally produced wino dominates the dark matter density by setting T_R appropriately (see the right panel of Fig. 4). From these arguments, we immediately find an upper limit on $m_{\tilde{w}}$,

$$m_{\tilde{w}} < 2.9 \text{ TeV} , \quad (95\% \text{ C.L.}) , \quad (25)$$

where we imposed the latest result on $\Omega_{\text{DM}}^{(\text{obs.})}h^2$ [10].

It is also worth pointing out that the upper limit becomes stronger down to

$m_{\tilde{w}} \lesssim 1$ TeV when we impose T_R to be higher than about 2×10^9 GeV as required by the conventional scenario of thermal leptogenesis [88], although much lower reheating temperature is allowed in more generic baryogenesis scenarios.

4 Current limits

In this section, we will review the current constraints from colliders, direct detections and indirect detections. The most robust lower limit is given by the collider search. Especially, LHC experiments give a stringent constraint by utilizing the long-lived charged wino tracks. The direct detections, on the other hand, do not provide competitive constraints because the scattering cross section is small as we have seen in the previous section. Still, the future direct experiments have promising sensitivity to detect $O(1)$ TeV wino. The indirect detection is a strong probe to the heavy dark matter above the collider energy scale. However, the cosmic-ray observation suffers from the astrophysical uncertainties such the dark matter distribution, cosmic-ray propagation, and backgrounds. Among them, constraints from the gamma-ray observation of the dSphs can be considered as the most conservative. In addition, conservative constraints can also be obtained from the probe to the early universe such as CMB, primordial abundance of the light elements (such as ^4He , ^3He , D, ^6Li , ^7Li), which is free from the major astrophysical uncertainties above.

4.1 Collider

The large electron positron collider (LEP) experiment started the operation in 1985 and shut down at the end of 2000. LEP has searched the long-lived chargino with the center of mass energy \sqrt{s} up to 209 GeV and the integrated luminosity $L \sim 630 \text{ pb}^{-1}$ [89, 91]. Different search is adopted with respect to the lifetime of the chargino. The stable chargino is searched by utilizing its charged track. For the short-lived chargino search, missing energy search is performed by using the emitted charged particle as the event trigger. The chargino with an intermediate lifetime can be searched by using the missing energy event tagged by the initial state radiation from the incoming e^+e^- . The left panel of Fig. 5 shows the combined limit. For the wino dark matter case ($\delta m \sim 145 - 165 \text{ MeV}$), the lower bound can be found at

$$m_{\tilde{w}} \gtrsim 90 \text{ GeV} \quad (95\% \text{ C.L.}) . \quad (26)$$

On the other hand, current large hadron collider (LHC) experiment also searches the long-lived chargino. The first run of LHC (Run 1) provides $L \sim 5 \text{ fb}^{-1}$ at $\sqrt{s} = 7$

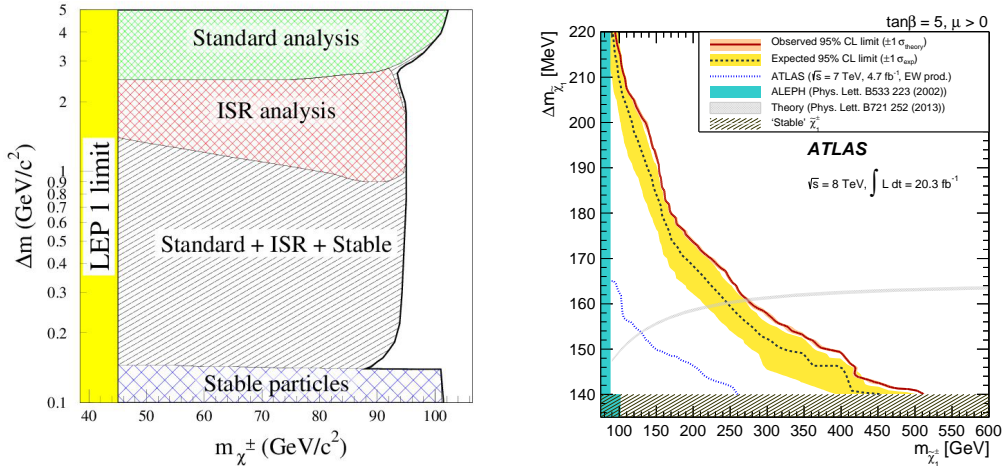


Figure 5: **Left panel:** The 95% exclusion region of the chargino mass by ALEPH collaboration of LEP experiment [89]. Here it is assumed that the lightest chargino is gaugino and Higgsino is much heavier than the gaugino. **Right panel:** The long-lived chargino mass limit by LHC [90]. The gray curve shows the lifetime of the pure wino case.

TeV in 2010, 2011 and $L \sim 20\text{fb}^{-1}$ at $\sqrt{s} = 8$ TeV in 2012. Broadly speaking, there are two possible ways to produce the wino by the LHC experiment. First one is the pair production of the gluino and its subsequent decay into two quarks and a charged/neutral wino, which leads to a conventional multiple jets plus missing transverse energy signature. This process, however, gives a limit on the gluino mass rather than the wino mass. In other words, if the gluino mass is heavier than 2.3 TeV, we do not have any limit on $m_{\tilde{w}}$ even at 14 TeV running [42]. A more distinctive possibility comes from the direct wino production through electroweak interactions, namely the Drell-Yan process, $pp \rightarrow g/q + \tilde{w}^0 \tilde{w}^\pm$ ($\tilde{w}^\pm \tilde{w}^\mp$), where g/q is utilized as the event trigger. As mentioned in Sec. 3.1, the charged wino decays mainly into a neutral wino emitting a soft pion (that is hardly detected at the LHC). Its decay length (without the Lorentz boost factor) is estimated to be about 7 cm. Thus, once the charged wino is produced, it can travel about $\mathcal{O}(10)$ cm before it decays, leaving disappearing charged track(s) inside inner detectors. As a result, the process predicts a mono-jet plus missing transverse energy signature accompanied by disappearing charged track(s) caused by the charged wino(s). The ATLAS collaboration reports an analysis on this process using 20.5 fb^{-1} data at the 8 TeV running [45]. The absence of significant deviation from SM backgrounds puts a limit:

$$m_{\tilde{w}} > 270 \text{ GeV} \quad (95\% \text{ C.L.}), \quad (27)$$

while $m_{\tilde{w}} > 260$ GeV (95% C.L) is obtained from the similar analysis by CMS collaboration with 19.5 fb^{-1} data at the 8 TeV run [46]. This is a very robust limit because it does not depend on other sparticle masses such as the gluino mass and is applicable as long as the wino is a stable LSP.

4.2 Direct detection

Direct detection, where the reaction between the dark matter and nucleon is utilized, is also the important approach for the dark matter detection. Recent underground experiments with a huge volume of stable liquid (such as Xenon, Argon) provides quite strong sensitivities to the light dark matter (~ 10 GeV). However, the sensitivity becomes weaker as the dark matter particle gets heavy because of the small number density. Moreover, for the pure wino case, because the wino dark matter does not interact with the nucleus at tree level, the scattering cross section is relatively small as was seen in Sec. 3.3 and it is difficult for the current experiments to reach the sensitivity line required by the wino detection. The future experiments, on the other hand, are designed to have stronger sensitivities by more than two orders of magnitude and we can expect the detection of the wino dark matter signal even for the mass is $\mathcal{O}(1)$ TeV.

Currently, above 10 GeV, the strongest constraints are given by the 2-layer type experiment using xenon liquid such as XENON100 [92], LUX [93]. The detectors catch the scintillation light from the collision between the dark matter and a nucleus. The collision emits the scintillation photons and electrons. The scintillation photons are observed as the first light peak through the photomultiplier tubes. The electrons, on the other hand, drift in the liquid xenon by the injected electric field and finally go into the gas xenon area where the gas and electron collision emit the other scintillation photons, which becomes the second photon peak of the reaction. The time difference of the peak provides the position of the collision and the information of the peak height and width enables one to efficiently separate the signal event to the background gamma-rays and electrons.

Fig. 6 shows the current (and future) sensitivity lines of the various direct detections. One can see that the current sensitivity lines ($\sim 10^{-45} \text{ cm}^2$) do not reach the wino scattering cross section given in Sec. 3.3 ($\sim 10^{-47} \text{ cm}^2$) at $m_{\tilde{w}} \sim \mathcal{O}(1)$ TeV. However, more and more large experiments are proposed such as Xenon1T [95], DarkSide-G2 [96], LZ [97] and DARWIN [98]. Especially, DARWIN plans to sweep the neutrino background region ($\sim 10^{-48} \text{ cm}^2$) and therefore 3 TeV wino can be de-

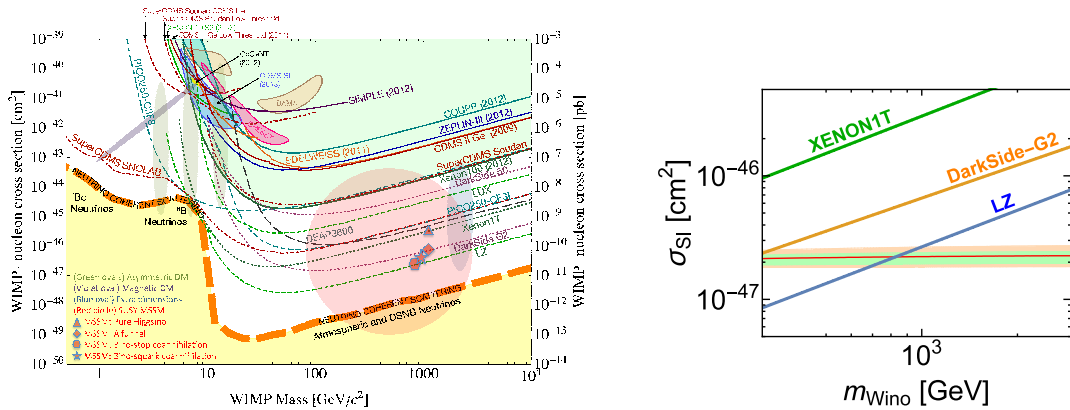


Figure 6: **Left panel:** Current and future sensitivity lines by the direct detections. The figure is from [94]. **Right panel:** The wino cross section and the sensitivity reaches of the future direct detections. The wino cross section is calculated by [61]. The green band shows the perturbative uncertainties and the yellow band is the error from the input parameters.

tected. The other experiments also reach the wino cross section, which will exclude $\mathcal{O}(1)$ TeV wino as shown in the right panel of Fig. 6.

4.3 Indirect detection

Indirect detection searches the signals from the annihilation products of the dark matter in the universe. There are many approaches to observe the dark matter signals: by utilizing anti-particles, neutrinos, and photons. Recently more and more precise cosmic-ray measurements are made and more stringent constraints are imposed on the dark matter annihilation. However, it is still difficult to discuss the conservative limit of these approaches because of the huge astrophysical uncertainties. For example, indirect detections utilizing the charged particle fluxes (anti-proton, anti-deuteron, electron, positron, etc.) suffer from the large systematic uncertainty of how the charged particles propagate in our galaxy [99]. On the other hand, the gamma-ray signals do not suffer from the uncertainty in propagation ^{#10} and moreover, since gamma-ray travels in a straight line, there are many targets which can be used to detect the wino dark matter, such as the central galactic region (CGR) of our galaxy, galactic clusters, diffused component of gamma-rays, and dSphs. One might expect that the conservative and strong sensitivity can be easily obtained by the

^{#10} The indirect detection of neutrino flux does not suffer from such an uncertainty in propagation. However, the acceptance of the neutrino signal is, unfortunately, too low to completely test the models in near future [100].

gamma-ray observations. However, the difficulties remain in the dark matter halo and the background estimations. The signal from dark matter annihilation at the CGR suffers from a significant uncertainty due to limited knowledge of dark matter profile and astrophysical background at the region [101]. ^{#11} The signal from galactic clusters is less certain due to unknown boost factors [105], and it seems difficult to test the models in near future [106]. Observation of diffuse gamma-rays to detect the wino dark matter is almost free from large systematic uncertainties caused by dark matter profile and astrophysical background. However, its signal is weak compared to others [107].

From the conservative point of view, dwarf spheroidal galaxies are the ideal targets. They are expected to be strong enough to test the wino dark matter, while systematic uncertainties from dark matter profile in each dSph and astrophysical background are much smaller than those of the CGR [108]. The indirect detection by the dSph observations is actually known to give a strong limit on wino dark matter [63] and therefore it is worth discussing its future prospect and conservativeness. Below, we introduce the current dSph gamma-ray observation and will investigate the future prospect and detailed conservativeness in Sec. 6 and Sec. 7.

In addition, other robust constraints can be obtained by the observables which reflect the phenomena of the early universe such as CMB, primordial abundance of the light elements because they do not suffer from the complicated astrophysical uncertainties described above. We also review the wino constraints from them.

4.3.1 dSph

As partially mentioned above, there are several advantages to consider the dSphs as the target to detect the wino dark matter. First, the measured values of mass density (as well as mass-to-light ratio) of the dSphs are high, indicating that they are dark matter rich objects. Second, baryonic gas densities inside the dSphs are very low and no active galactic nucleus is observed, which reduces astrophysical gamma-ray backgrounds to small values. Finally, they are also relatively nearby from us and the measurement of velocity dispersions inside each dSph allows us to estimate its dark matter profile precisely.

DSphs can be classified into two types: Classical dSph, and ultra-faint dSph.

^{#11} The use of the monochromatic gamma-ray helps to reduce the background gamma-ray and enhances the detectability of the dark matter signal as performed by H.E.S.S. experiment [102]. With a huge uncertainty of the dark matter profile, however, only a small portion of the wino mass range can be excluded (see Ref. [103, 104] for related discussions).

The classical dSphs contain the eight dSphs, Ursa Minor, Sculptor, Draco, Sextans, Carina, Fornax, Leo I, and Leo II, which have been discovered before the Sloan Digital Sky Survey (SDSS) observation [109]. Because classical dSph contains a large number of the bright stars in their system, the kinematical survey of the galaxy stars provide relatively solid estimation of the dark matter halos.

After the SDSS observation, many fainter dwarf spheroidal galaxies called ultra-faint dSphs have been discovered. Some of them are located within 10–50 kpc from us and their mass-to-light ratios are about ten times larger than those of the classical dSphs, which implies that the strong dark matter signal can be emitted from them. Their dark matter profiles are, however, not fixed well due to limited stellar kinematic data: only 10–100 stellar kinematic data have been obtained at present for each ultra-faint dSph.

The most stringent limit on the annihilation cross section of the wino dark matter is currently from the six years data of the Fermi-LAT observation [63]. The Fermi-LAT collaboration provides limits by combining the observational data of fifteen dSphs including seven classical dSphs (except for Leo I) and eight ultra-faint dSphs, which is shown by the blue line in Fig. 7 and it gives the exclusion of $m_{\tilde{w}} < 900 \text{ GeV}$ and $1.8 \text{ TeV} < m_{\tilde{w}} < 2.7 \text{ TeV}$ at 95% confidence level. In the figure, the dark matter is assumed to annihilate into W^+W^- with 100% branching fraction, which approximates well the branching fraction of the wino dark matter. Here, we stress that the dark matter halo of the ultra-faint dSphs are obtained in a highly biased way, as discussed in Sec. 6, and it seems not clear whether or not the limit can be regarded as the robust one.

The more conservative limit can be extracted from the sensitivity line of classical dSphs [108] as shown in the green line in Fig. 7. Here we depict the sensitivity line from Ursa Minor which gives the strongest limit among them.^{#12} Because the dark matter halos of the classical dSphs are obtained by a relatively robust way, the limits can be regarded as more robust ones than those by fifteen dSphs. It can be seen from the figure that the conservative lower bound of the wino dark matter mass is

$$m_{\tilde{w}} > 320 \text{ GeV} \quad (95\% \text{ C.L.}) . \quad (28)$$

This sensitivity line is provided by the four years observation data under the old event selection algorithm. By the update of the event selection criteria and exposure time, the sensitivity gets stronger by $\sim 40\%$ and gives $m_{\tilde{w}} \gtrsim 350 \text{ GeV}$.

^{#12}The limit is not significantly altered even if we combine data of all classical dSphs.

4.3.2 CMB

Recent Planck satellite provides very precise map of the CMB anisotropy of its temperature and polarization [10]. The amplitude of these power spectra reflects the history of the early universe and therefore we can extract the information about the energy density of the baryon and dark matter, spatial curvature, the Hubble constant, the primordial fluctuation and more.

The existence of the dark matter slightly distorts the CMB spectrum through its annihilation. The injection of the annihilation product ionizes and excites the hadron plasma at the time of the recombination, which reduces the amplitude of the spectrum. On the other hand, the fractions of the ions after the recombination are increased by the remnant of the annihilation products, which enhances the amplitude of the CMB polarization. Current CMB observation shows no large deviation from the standard theory, which implies that the large annihilation cross section of the dark matter becomes inconsistent with the current observation [110, 111, 112, 113, 114].

The energy injection from the dark matter annihilation per volume can be written by

$$\frac{dE}{dt dV} = \rho_{\text{crit}}^2 c^2 \Omega_{\text{DM}}^{(\text{obs.})^2} (1+z)^6 \frac{f(z) \langle \sigma v \rangle}{2m_{\text{DM}}}, \quad (29)$$

where ρ_{crit} is the critical density of the current universe and m_{DM} is the dark matter mass and z represents the redshift. $f(z)$ represents the efficiency of the energy injection to the gases which depends on the final state of the annihilation. The computation of $f(z)$ is provided by Ref. [113, 115, 116]. The injected energy goes into heating the plasma, ionizations and excitations of the gases. The fraction of them (and its time dependence) is estimated by Ref. [117].

The energy injection is encoded in the recombination calculation routine RECFAST [118] used in the CMB calculation code CAMB [119], which provides TT, TE, EE spectrum through the history of the ionization and heating and Planck collaboration provides the constraint using the latest observational data [10]. The wino dark matter case can be approximated by considering WW mode of $f(z)$ (~ 0.29 [113]), which gives

$$m_{\tilde{w}} \gtrsim 430 \text{ GeV} \quad (95\% \text{ C.L.}), \quad (30)$$

as shown in Fig. 7.^{#13}

^{#13} We note that the most of the CMB distortion stems from the non-standard energy injection

4.3.3 BBN

The energy injection from the dark matter annihilation might affect the primordial abundance of the light elements such as ^4He , ^3He , D, ^6Li , ^7Li . Current observation precisely determines the nucleon abundances, which in turn gives stringent constraints on the dark matter annihilation. Based on the latest discussion given by Ref. [120], we will briefly review these constraints.

The effect of the dark matter annihilation appears in the primordial abundances of the light elements which are computed by solving the following Boltzmann equations:

$$\frac{dn}{dt} + 3Hn = (\text{standard BBN contributions}) + (\text{dark matter contribution}), \quad (31)$$

where n represents the number density of the light elements and H is the expansion rate of the universe. The dark matter contribution can be expressed by the sum of the three components: photodissociation, hadrodissociation and the contribution to the interconversion process between proton and neutron.

In Ref. [120], they improve the accuracy of the calculation by involving the effect of anti-nucleons produced by dark matter annihilation and the interconversion reactions between (anti-) neutron and (anti-) proton. The effect of the anti-nuclei is partially involved: They consider the energetic proton production by the anti-nuclei scattering process and include it to the ^4He -p collision. The products from the anti-nuclei - ^4He collision is neglected because of the lack of the experimental data. Here we note that this neglect underestimates the dark matter effect and therefore the constraint on the dark matter annihilation becomes conservative.

For the observables, the most promising one is the primary D (deuteron) measured from the D absorption in damped Ly α system [121]. The ratio between D and H measures $D/H = (2.53 \pm 0.04) \times 10^{-5}$, where the error is smaller than the previous result by a factor of 5. They also estimate the constraints from the mass fraction of the primordial helium 4 obtained by the infrared and visible ^4He line from HII regions in extra-galaxies [122] as well as $^3\text{He}/\text{D}$ obtained from protosolar cloud observation [123]. They do not consider the sensitivity lines from ^7Li , ^6Li observation because of the lack of the reliability [124, 125].

The result shows that the most severe constraint is from D/H. For the wino dark

during the recombination and therefore, the dark matter annihilation rate at the recombination is mostly constrained. However, for the wino case, the difference of the cross section at the current and the recombination era is found to be negligible [29].

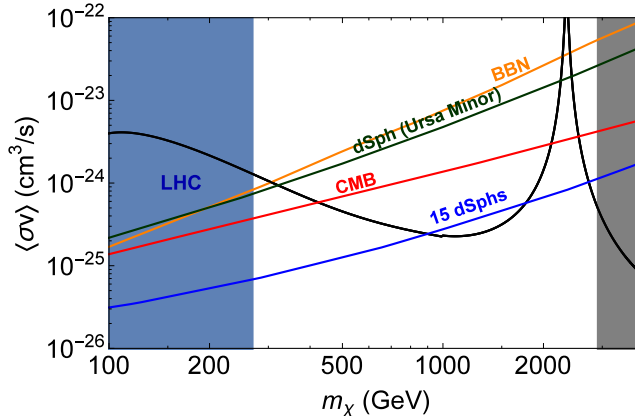


Figure 7: *The current wino mass limit. The blue-shaded region is excluded by the LHC experiments and the gray-shaded region is the upper bound from the thermal relic. The orange, green, red, and blue lines represent the constraints from BBN, dSph (Ursa Minor), CMB, and 15 dSphs respectively.*

matter case, the exclusion line gives

$$m_{\tilde{w}} \gtrsim 320\text{GeV} \quad (95\% \text{ C.L.}) , \quad (32)$$

as shown in Fig. 7. The ${}^4\text{He}$ provides more than two orders of magnitude weaker constraint, while ${}^3\text{He}/\text{D}$ is much weaker than ${}^4\text{He}$.

4.4 Summary of the current limits

In this section, we have reviewed the current limit of the wino dark matter. The collider experiments provides the robust lower bound of the wino mass and the disappearing track search excludes wino lighter than 270 GeV. On the other hand, because the nucleon-wino interaction is suppressed, the direct detection does not strongly constrain the wino mass, while the future experiments can detect wino with a mass of $\mathcal{O}(1)$ TeV. For the indirect detection search, although it is difficult to perfectly control the astrophysical uncertainty, the robust constraint can be obtained by the dSph, CMB and the primordial abundances of the light elements, which exclude $m_{\tilde{w}} \lesssim 430$ GeV in addition to the vicinity of the peak of the Sommerfeld enhancement: $2.1 \lesssim m_{\tilde{w}} \lesssim 2.5$ TeV.

From the next section, we investigate the future limits especially focusing on the collider search and indirect detection.

5 Future constraints from collider searches

5.1 Review

In 2015, LHC started new run (Run 2) with 13 TeV center of mass energy. 13 TeV run of 2015 provided 3 fb^{-1} integrated luminosity, which is expected to reach 30 fb^{-1} in 2016. Run 2 will be continued to 2018 with $\sqrt{s} = 13 - 14 \text{ TeV}$, under which the luminosity will increase to $\sim 100 \text{ fb}^{-1}$. After a long shutdown phase, Run 3 will be implemented in 2020 – 2022 which will provide another $\sim 250 \text{ fb}^{-1}$ luminosity with 14 TeV center of mass energy. Finally, the high-luminosity run (named Run 4, Run 5) will be implemented from 2024, where the accumulated luminosity will reach $\sim 3000 \text{ fb}^{-1}$ with new detectors. We can expect that the disappearing track discussed in the previous section will prove a considerably heavier wino under the $\mathcal{O}(10)$ TeV center of mass energy and the large number of statistics. Although the detailed capability and background estimation are still unknown, the estimation indicates that the exclusion reaches 500 GeV at the 14 TeV run [47, 48].

The next hadron collider is also proposed by CERN (FCC) [55] and China (SppC) [56], both of which is designed to have $\sim 100 \text{ TeV}$ center of mass energy. The impact of the 100 TeV collider is estimated [48] and it is found that it can exclude $m_{\tilde{w}} < 3.2 \text{ TeV}$ by the disappearing track search at $L = 3000 \text{ fb}^{-1}$. However, development of the detector should be required for the extremely high energy environment and therefore it is still unclear whether the running performance can reach the expected sensitivity.

As a promising near future collider, e^+e^- collider is a strong probe for the wino dark matter. The lepton collider provides clean event signals above $\mathcal{O}(100)$ GeV energy level. Moreover, by tuning the polarization of incoming e^+e^- , the detection is sensitive for the interaction of the produced particles. One of the most promising project is the international linear collider (ILC) [49], which is led by the Japanese collaboration where the center of mass energy is at most 1 TeV and provides the polarized beam of $(P_- P_+) = (-80\%, +60\%)$ at most. Here, P_- (P_+) is defined by the fraction of the right handed electron (positron) minus fraction of the left handed electron (positron). As a multi-TeV e^+e^- linear collider, Compact Linear Collider (CLIC) [50] is also under review whose center of mass energy reaches up to 3 TeV in the benchmark program. CERN and China also propose the e^+e^- circular collider with $\sqrt{s} \sim 250 \text{ GeV}$ as the first-phase project of their circular collider projects (named FCC-ee, CEPC respectively).

The dark matter search by the lepton colliders can be classified into two cases

with respect to the dark matter mass $m_{\tilde{w}}$. One is for $m_{\tilde{w}} < \sqrt{s}/2$, where the dark matter pair can be directly produced. In that case, the direct production tagged by the mono-photon gives stringent constraints [51, 52]. Ref. [52] also includes the effect of the final state radiation from the charged wino pair^{#14} and shows that 240 GeV wino can be excluded with 5σ significance at $\sqrt{s} = 500$ GeV, $L = 500\text{fb}^{-1}$. The study also shows that it is possible to distinguish the wino dark matter signal from the other dark matter candidates by utilizing the threshold excitation and the beam polarization.

The other case is for $m_{\tilde{w}} > \sqrt{s}/2$, which implies that the pair production does not occur. Although this case is especially important for $\mathcal{O}(1)$ TeV wino dark matter, the detection potential has not been clear. In Ref. [54], we have pointed out that significant sensitivity can be obtained by using the indirect search, where the loop correction from the dark matter is measured via the standard model final state such as quark pair, lepton pair production. Below, based on our work [54], we discuss the indirect search by using the lepton colliders.

5.2 Loop Corrections

In this section, we discuss the impact of the indirect search of the future lepton colliders. Although the focus of this thesis is the wino dark matter search, it is informative to discuss more general new particle detection, where the particle only interacts with the electroweak gauge bosons (EWIMP).

Let us consider an EWIMP of a mass m which is an $SU(2)_L$ n -tuple and has a hypercharge of Y . Here we assume that the EWIMP interacts with SM particles only through the SM gauge interactions. We here note that the EWIMP may have other renormalizable interactions with SM particles especially when it is scalar. For instance, the interaction $|\phi|^2|H|^2$ is allowed with ϕ being the EWIMP. The interaction $(\phi H)^2$ or $(\phi^\dagger H)^2$ is also possible if ϕ has a hypercharge of $\pm 1/2$. Though these interactions contribute to the EWIMP mass after the electroweak symmetry breaking, its effect is not significant as far as the EWIMP mass m is sufficiently larger than the electroweak scale. We therefore neglect the effects in the following discussions to make our discussion simple.^{#15} Here, we note that the wino LSP is

^{#14} They assume that the charged wino is also invisible.

^{#15} The interactions addressed here are allowed even if the EWIMP is odd under some Z_2 symmetry while all SM particles being even, as in the case that the EWIMP is dark matter. The interactions are, however, severely constrained by recent dark matter direct detection experiments when the EWIMP plays the role of dark matter.

the case of the Majorana fermion with $(n = 3, Y = 0)$.

Below, we focus on the SM processes $e^-e^+ \rightarrow f\bar{f}$. The loop correction also appears in the triple gauge couplings such as γWW and ZWW , which affect e.g. the process $e^-e^+ \rightarrow W^-W^+$. However, by the discussion of the effective field theory,^{#16} it is found that this channel is not as efficient as the fermion pair creation, at least when $m \gg \sqrt{s}$ [50, 127].

After integrating the EWIMP out at one-loop level, we obtain the following effective Lagrangian $\mathcal{L}_{\text{eff}}^{\text{EWIMP}}$ for the $e^-e^+ \rightarrow f\bar{f}$ processes:

$$\mathcal{L}_{\text{eff}}^{\text{EWIMP}} = \mathcal{L}_{\text{SM}} + \frac{g_2^2 C_{WW}}{8} W_{\mu\nu}^a \Pi(-D^2/m^2) W^{a\mu\nu} + \frac{g_1^2 C_{BB}}{8} B_{\mu\nu} \Pi(-\partial^2/m^2) B^{\mu\nu} + \dots, \quad (33)$$

where the coefficients C_{WW} and C_{BB} are given by

$$C_{WW} = \frac{n(n-1)(n+1)}{6} \begin{cases} 1 & \text{(Complex scalar)} \\ 8 & \text{(Dirac fermion)} \end{cases}, \quad (34)$$

$$C_{BB} = 2nY^2 \begin{cases} 1 & \text{(Complex scalar)} \\ 8 & \text{(Dirac fermion)} \end{cases}. \quad (35)$$

An additional factor 1/2 should be multiplied for a real scalar and a Majorana fermion.^{#17} The function $\Pi(x)$ is the renormalized self-energy of the gauge bosons from the EWIMP's loop. Its explicit form is

$$\Pi(x) = \begin{cases} \frac{1}{16\pi^2} \int_0^1 dy y(1-y) \ln[1 - y(1-y)x] & \text{(Fermion)} \\ \frac{1}{16\pi^2} \int_0^1 dy (1-2y)^2 \ln[1 - y(1-y)x] & \text{(Scalar)} \end{cases}. \quad (36)$$

Here we have used the $\overline{\text{MS}}$ regularization scheme with the renormalization scale of $\mu_{\overline{\text{MS}}} = m$.

As can be seen in the effective Lagrangian (33), the EWIMP's effect is encoded in the operators involving two field strength tensors. It is worth notifying that the absence of couplings to any SM particles other than the gauge interactions ensure the SM symmetry like flavor, CP and custodial symmetries, etc. Precision measurements

^{#16} Namely the SM Lagrangian plus higher dimensional operators which are obtained after integrating the EWIMP out [126].

^{#17} The ellipsis at the end of the Lagrangian includes operators composed of the strength tensors more than two, but those are irrelevant for the following discussion.

at low energy experiments are thus not efficient to see the effect of the EWIMP. #18 Energetic lepton colliders such as ILC, CLIC, FCC-ee and CEPC will therefore play an important role to detect the new EWIMP.

Let us calculate the indirect corrections to the process $e^-e^+ \rightarrow f\bar{f}$. When the final state is a SM fermion pair other than an electron-positron pair, the leading order (LO) amplitude is

$$i\mathcal{M}_{\text{LO}}[e_h^-(p)e_{\bar{h}}^+(p') \rightarrow f_{h'}(k)\bar{f}_{\bar{h}'}(k')] = i[\bar{v}_h(p')\gamma^\mu u_h(p)] \sum_{V=\gamma,Z} \frac{C_{e_h V} C_{f_{h'} V}}{s - m_V^2} [\bar{u}_{h'}(k)\gamma_\mu v_{h'}(k')], \quad (37)$$

where $h, h' = L, R$ ($\bar{h}, \bar{h}' = R, L$) represent the chirality of the fermions. Fermion wave functions are defined as $u_{L(R)}(p) = P_{L(R)}u(p)$ and $v_{L(R)}(p) = P_{L(R)}v(p)$ with $u(p)$ and $v(p)$ being those of particles and anti-particles. Gauge couplings of the fermions are given by $C_{f_L Z} = g_Z(T_{3f}/2 - Q_f s_W^2)$, $C_{f_R Z} = -g_Z Q_f s_W^2$ and $C_{f_L \gamma} = C_{f_R \gamma} = eQ_f$ with T_{3f} and Q_f being the third component of the weak isospin and the electric charge of the fermion f . The coupling g_Z is defined by $g_Z = g_2/c_W$.

When the final state is an electron-positron pair, the LO amplitude of processes $e_L^-e_R^+ \rightarrow e_R^-e_L^+$ and $e_R^-e_L^+ \rightarrow e_L^-e_R^+$ are again given by the amplitude (37). On the other hand, those of other processes, $e_L^-e_R^+ \rightarrow e_L^-e_R^+$, $e_R^-e_L^+ \rightarrow e_R^-e_L^+$, $e_L^-e_L^+ \rightarrow e_L^-e_L^+$ and $e_R^-e_R^+ \rightarrow e_R^-e_R^+$, are given by

$$i\mathcal{M}_{\text{LO}}(e_h^-e_{\bar{h}'}^+ \rightarrow e_h^-e_{\bar{h}'}^+) = i[\bar{v}_{h'}(p')\gamma^\mu u_h(p)] \sum_{V=\gamma,Z} \frac{C_{e_h V} C_{e_{h'} V}}{s - m_V^2} [\bar{u}_h(k)\gamma_\mu v_{h'}(k')] \\ - i[\bar{u}_h(k)\gamma^\mu u_h(p)] \sum_{V=\gamma,Z} \frac{C_{e_h V} C_{e_{h'} V}}{t - m_V^2} [\bar{v}_{h'}(p')\gamma_\mu v_{h'}(k')]. \quad (38)$$

The contribution of the EWIMP to the di-fermion processes appear at the next leading order (NLO), which can be evaluated by the effective Lagrangian (33). When the final state is a SM fermion pair other than an electron-positron pair, the contribution to the amplitude is given by

$$i\mathcal{M}_{\text{BSM}}(e_h^-e_{\bar{h}}^+ \rightarrow f_{h'}\bar{f}_{\bar{h}'}) = i[\bar{v}_h(p')\gamma^\mu u_h(p)] \sum_{V V'=\gamma,Z} \frac{C_{e_h V} C_{f_{h'} V'} d_{VV'} s \Pi(s) [\bar{u}_{h'}(k)\gamma_\mu v_{h'}(k')]}{(s - m_V^2)(s - m_{V'}^2)}, \quad (39)$$

where $d_{VV'}$ are gauge group factors whose explicit forms are $d_{ZZ} = (g_Z^2/2)(c_W^4 C_{WW} + s_W^4 C_{BB})$, $d_{\gamma\gamma} = (e^2/2)(C_{WW} + C_{BB})$ and $d_{Z\gamma} = d_{\gamma Z} = (e g_Z/2)(c_W^2 C_{WW} - s_W^2 C_{BB})$,

#18 Contribution to the oblique parameters [128] (including the extension of S, T, U [129, 130]) from the operators proportional to C_{WW} and C_{BB} has been evaluated in Ref. [131] and turned out to be small.

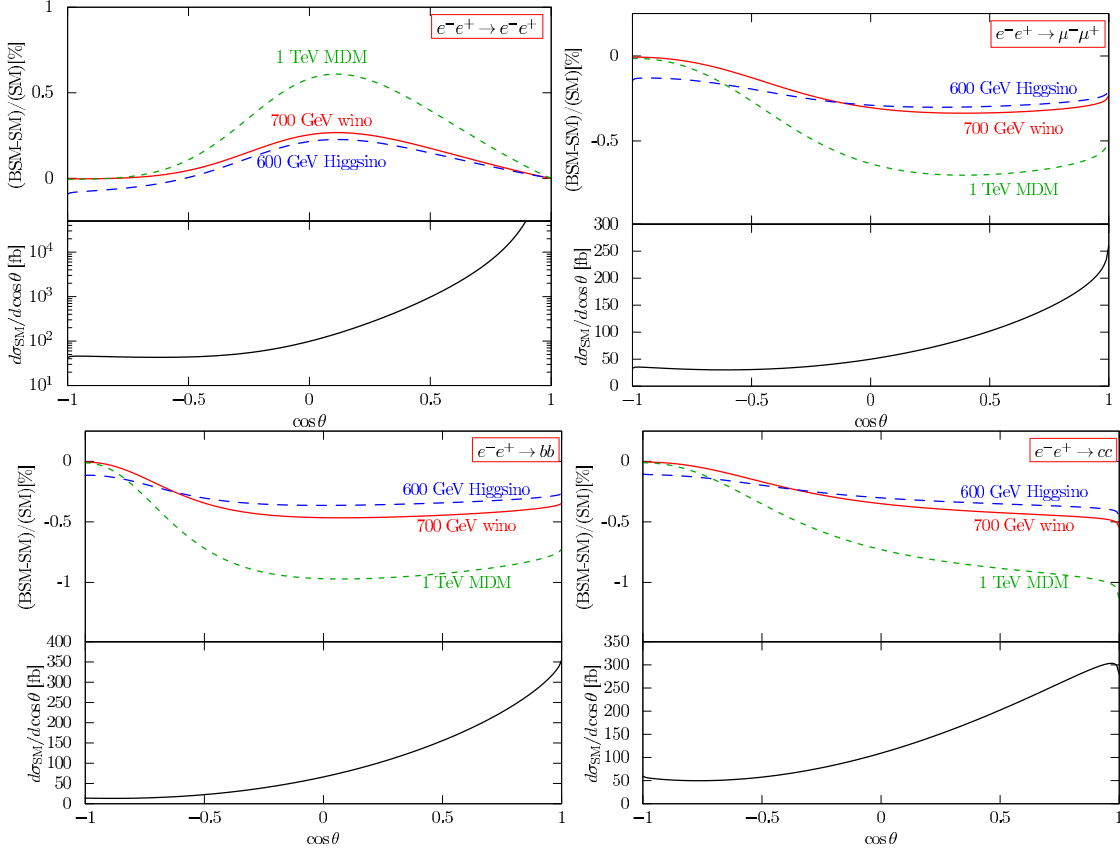


Figure 8: Contributions to the differential cross section of $e^-e^+ \rightarrow f\bar{f}(\gamma)$ from the 700 GeV wino, the 600 GeV Higgsino and the 1 TeV fermionic minimal dark matter. The center of mass energy is fixed to be $\sqrt{s} = 1$ TeV with polarizations of incoming electron and positron beams being $P_- = -80\%$ and $P_+ = +60\%$, respectively. The “ $d\sigma_{\text{SM}}/d\cos\theta$ ” plots show the one-loop SM differential cross sections.

respectively. The EWIMP’s contribution to processes $e_L^-e_R^+ \rightarrow e_R^-e_L^+$ and $e_R^-e_L^+ \rightarrow e_L^-e_R^+$ are also given by the above formula. The contribution to the process $e_h^-e_{h'}^+ \rightarrow e_h^-e_{h'}^+$ is, on the other hand, given by

$$\begin{aligned}
i\mathcal{M}_{\text{BSM}}(e_h^-e_{h'}^+ \rightarrow e_h^-e_{h'}^+) &= i[\bar{v}_{h'}(p')\gamma^\mu u_h(p)] \sum_{V,V'=\gamma,Z} \frac{C_{e_h V} C_{e_{h'} V'} d_{VV'} s \Pi(s) [\bar{u}_h(k)\gamma_\mu v_{h'}(k')]}{(s - m_V^2)(s - m_{V'}^2)} \\
&\quad - i[\bar{u}_h(k)\gamma^\mu u_h(p)] \sum_{V,V'=\gamma,Z} \frac{C_{e_h V} C_{e_{h'} V'} d_{VV'} t \Pi(t) [\bar{v}_{h'}(p')\gamma_\mu v_{h'}(k')]}{(t - m_V^2)(t - m_{V'}^2)}.
\end{aligned} \tag{40}$$

The NLO amplitudes (39) and (40) have the same chirality structure as the LO ones (37) and (38). The dominant contribution of the EWIMP is thus from the interference between these amplitudes.

As some examples, we show in Fig. 8 contributions to the differential cross section of $e^-e^+ \rightarrow f\bar{f}(\gamma)$ from the 700 GeV wino (Majorana fermion with $n = 3$ & $Y = 0$), the 600 GeV Higgsino (Dirac fermion with $n = 2$ & $Y = \pm 1/2$) and the 1 TeV minimal DM (Majorana fermion with $n = 5$ & $Y = 0$) at one-loop level with the center of mass energy of $\sqrt{s} = 1$ TeV. Polarizations of incoming electron and positron beams are assumed to be $P_- = -80\%$ (left-handed like) and $P_+ = +60\%$ (right-handed like), respectively,^{#19} because the EWIMPs in the examples mainly affect the $SU(2)_L$ gauge boson propagator through the interaction $W_{\mu\nu}^a \Pi(-D^2/m^2) W^{a\mu\nu}$ in the effective Lagrangian (33). While the most important benefit of the beam polarization is to enhance the cross section and effectively increase the integrated luminosity, it also reduces the right-handed electron process which in practice contributes to the background. Therefore, the polarization can enhance the signal significance against the systematic errors, which is an additional gain to the increase of the effective luminosity. In order to depict the figures (and to discuss the prospect of future lepton colliders in the next section), we have also included SM contributions at NLO order using the code AITALC [137] with a slight modification, which integrates the programs QGRAF [138], DIANA [139], FORM [140], LOOPTOOLS [141] and FF [142]. Here we set $E_\gamma^{\text{max}} = 0.1\sqrt{s}$ for $e^-e^+ \rightarrow f\bar{f}\gamma$ at the NLO calculation.

5.3 Analysis method and detector performance

In order to quantitatively investigate the capability of future lepton colliders for probing the EWIMP, we adopt the binned likelihood analysis on the differential cross section of the process $e^-e^+ \rightarrow f\bar{f}$. We use ten uniform intervals for the scattering angle $\cos\theta \in [-1 : 1]$ for the final state $f \neq e^-$, while $\cos\theta \in [-0.99 : 0.99]$ for $f = e^-$. We have assumed a simplified setup for detection efficiency; 100% for leptons, 80% for b -jets and 50% for c -jets. Here, we require at least one heavy flavor quark identification for b - and c -jets channels. We then define the χ^2 function as

$$\chi^2 = \sum_{i=1}^{10} \frac{\left[N_i^{(\text{BSM+SM})} - N_i^{(\text{SM})} \right]^2}{N_i^{(\text{SM})} + \left[\epsilon_i N_i^{(\text{SM})} \right]^2}, \quad (41)$$

where $N_i^{(\text{SM+BSM})}$ ($N_i^{(\text{SM})}$) is the expected value of the number of events with (without) the EWIMP contribution, while ϵ_i represents a systematic error in the estimation of $N_i^{(\text{SM})}$. The denominator thus represents a quadratic sum of the systematic

^{#19}The polarization of the positron beam is assumed to be the future upgradeable maximum at the ILC [132, 133, 134, 135, 136].

and statistical errors. We have also assumed that the correlation between the errors is negligible and treated them as independent ones.

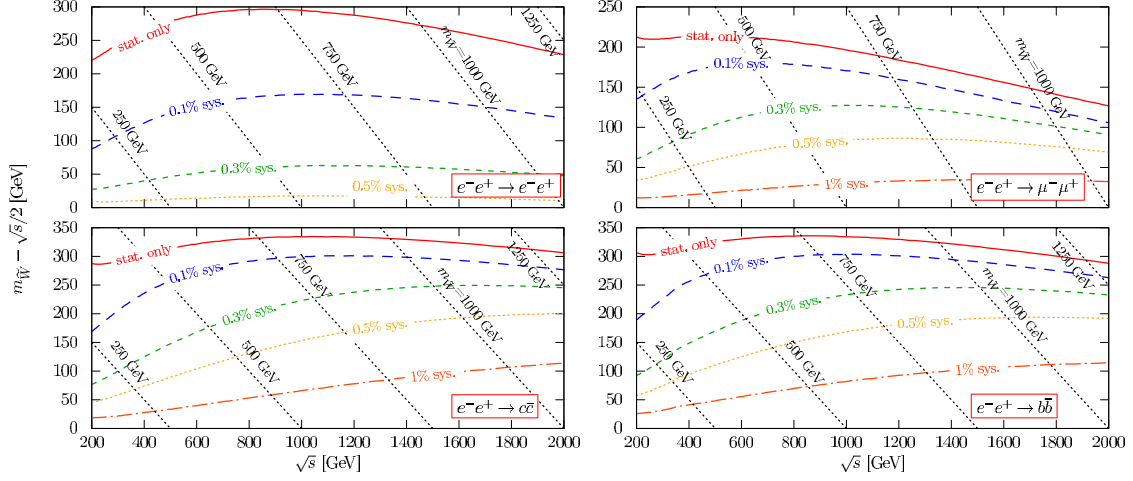
We have only considered the irreducible background from the SM di-fermion process to estimate $N_i^{(\text{SM})}$, as discussed in the previous section. Other reducible backgrounds are expected to be negligible, for those give little events in the signal region of $E_f + E_{\bar{f}} \simeq \sqrt{s}$. In reality, the estimation of the irreducible background suffers from various kinds of experimental uncertainties, such as luminosity, polarization and acceptance estimation errors. The above ϵ_i represents a collective parameterization of these uncertainties, which is expected to be $O(0.1 - 1)\%$ according to the current ILC technical design report (TDR) [132, 133, 134, 135, 136]. Estimating the precise value of the ϵ_i is beyond the scope of this article. Instead, we examine how large the change of ϵ_i alters the capability of future lepton colliders by adopting several representative values of $\epsilon_i = 0, 0.1, 0.3, 0.5$ and 1% .

The deviation from the SM prediction approximately scales as $N^{(\text{BSM+SM})} - N^{(\text{SM})} \propto 1/m^2$, because it comes from an interference between the SM and the EWIMP amplitudes. According to the χ^2 function (41), when the statistical error dominates the systematic one, the EWIMP mass reach turns out to be approximately proportional to $s^{1/4}L^{1/4}$. It can therefore be seen that increasing the luminosity L is equivalent to increasing the collision energy squared s , so that accumulating data at future lepton colliders has a great impact on the EWIMP search. Needless to say, the systematic error eventually dominates the statistical one when L becomes large enough, which is estimated to be $L \gtrsim (10^{-5}/\epsilon_i^2)(s/1 \text{ TeV}^2)[\text{ab}^{-1}]$. The mass reach is then proportional only to s in such a case.

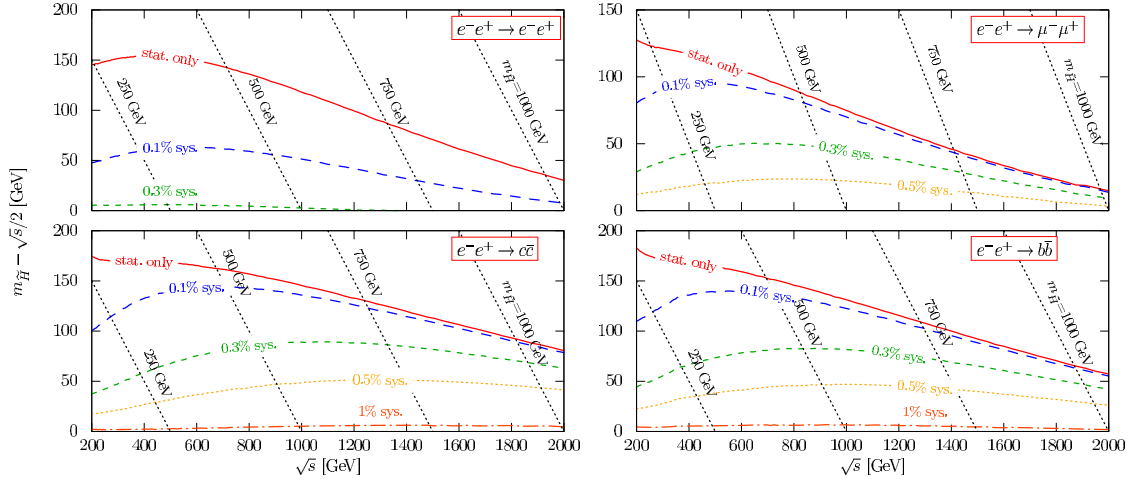
5.4 Results

We are now at the position to discuss the capability of future lepton colliders to probe EWIMPs. As mentioned earlier, we consider not only the wino LSP but also several well-motivated EWIMP candidates: the Higgsino LSP and a few minimal dark matters (MDMs). We have assumed the integrated luminosity of $L = 3 \text{ ab}^{-1}$ and the beam polarizations of $P_- = -80\%$ and $P_+ = +60\%$ in the following discussions, unless otherwise stated explicitly.

The capability of future lepton colliders to probe the wino LSP ($n = 3$ & $Y = 0$, Majorana fermion) and Higgsino LSP ($n = 2$ & $Y = \pm 1/2$, Dirac fermion) are shown in Fig. 9. As we have mentioned before, left-handed electron and right-handed positron beam polarizations have better sensitivity than the opposite ones

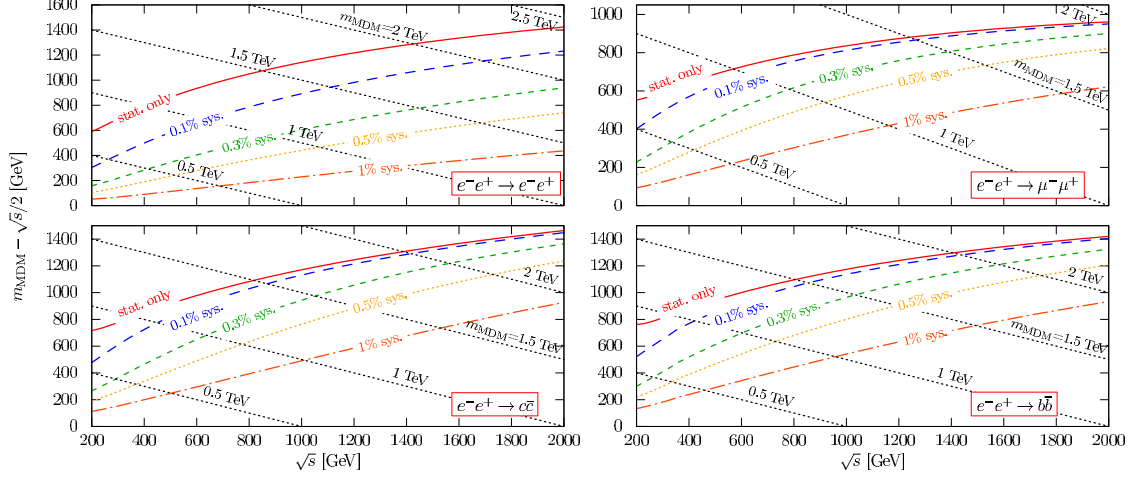


(a) The wino LSP

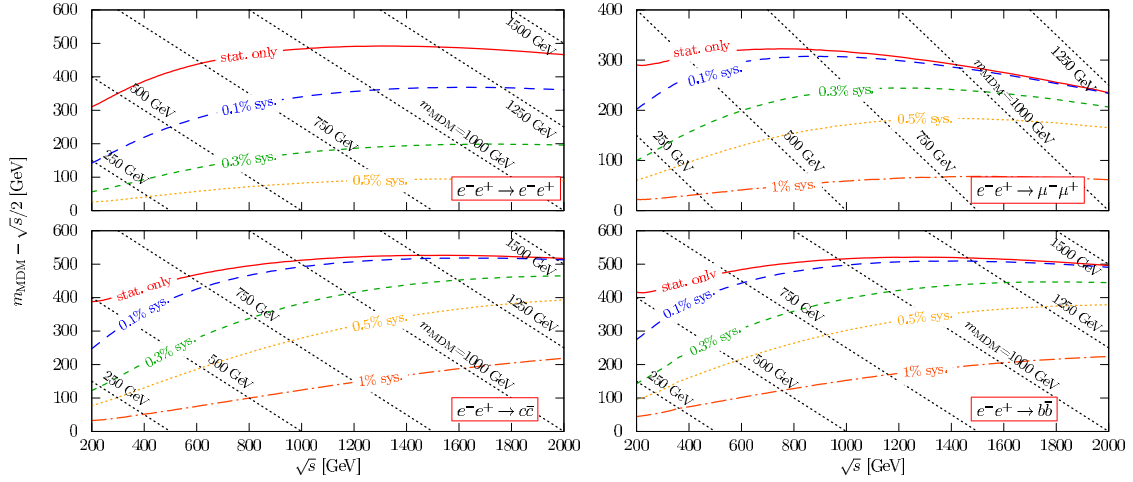


(b) The Higgsino LSP

Figure 9: Prospect of LSP dark matter searches: (a) The wino LSP ($n = 3$ & $Y = 0$, Majorana fermion) and (b) The Higgsino ($n = 2$ & $Y = \pm 1/2$, Dirac fermion). The differences between the expected reach of the EWIMP mass m at 95% C.L. and the beam mass $\sqrt{s}/2$ is shown. Here we assume that the integrated luminosity of 3 ab^{-1} and the electron and positron beam polarizations of -80% and $+60\%$. We have shown the results with the systematic uncertainty of $\epsilon_i = 0, 0.1, 0.3, 0.5$ and 1% .



(a) The minimal fermion dark matter ($n = 5$ and $Y = 0$)



(b) The minimal scalar dark matter ($n = 7$ and $Y = 0$)

Figure 10: Prospect of minimal dark matter (MDM) searches: (a) The Majorana fermion MDM ($n = 5$ & $Y = 0$) and (b) The real scalar MDM ($n = 7$ & $Y = 0$). The differences between the expected reach of the MDM mass m_{MDM} at 95% C.L. and the beam energy $\sqrt{s}/2$ is shown. Here we assume that the integrated luminosity of 3 ab^{-1} and the electron and positron beam polarizations of -80% and $+60\%$. We have shown the results with the systematic uncertainty of $\epsilon_i = 0, 0.1, 0.3, 0.5$ and 1% .

for these EWIMP candidates. The Higgsino LSP also affects the $U(1)_Y$ gauge boson propagator, but this contribution is less significant than that from the $SU(2)_L$ gauge boson propagator due to the smallness of the $U(1)_Y$ gauge coupling. As can be seen from the figure, a future collider with $\sqrt{s} = 500 \text{ GeV}$ (1 TeV) will probe the mass up to 430 GeV (670 GeV) for the wino LSP and 340 GeV (560 GeV) for the Higgsino LSP by measuring the scattering cross section of the $e^-e^+ \rightarrow \mu^-\mu^+$ process with the systematic error of $\epsilon_i = 0.1\%$.

We consider two types of the MDM. One is a Majorana fermion with $n = 5$ and $Y = 0$ and the other is a real scalar with $n = 7$ and $Y = 0$. The stability of both particles is automatically guaranteed without imposing any ad hoc parities [87, 143, 144]. The capability of future lepton colliders to probe these dark matters are shown in Fig. 10. Left-handed electron and right-handed positron beam polarizations are better than the opposite ones in both cases. As can be seen from the figure, a future collider with $\sqrt{s} = 500 \text{ GeV}$ (1 TeV) will probe the mass up to 850 GeV (1.5 GeV) for the fermionic MDM and 530 GeV (810 GeV) for the bosonic MDM by measuring the scattering cross section of the $e^-e^+ \rightarrow \mu^-\mu^+$ process with the systematic error of $\epsilon_i = 0.1\%$. The contribution of the EWIMP to di-fermion processes is approximately proportional to n^3 as seen in equation (34), so that the minimal dark matters are more easily accessible than the LSP dark matters.

Finally, we also show the combined sensitivity for the wino in Fig. 11. Here we assume the integrated luminosity of 2 ab^{-1} and the electron and positron beam polarizations of -80% and $+60\%$. Sys. 1 represents the combined result under the systematic errors of 0.2% for electron, 0.15% for muon, 0.5% for bottom, and 1% for charm while Sys. 2 is estimated under the systematic errors of 0.4% for electron, 0.3% for muon, 1% for bottom, and 2% for charm. The figure shows that $\sqrt{s} = 1 \text{ TeV}$ can search up to $650 - 750 \text{ GeV}$ wino.

5.5 Potential of future lepton colliders with large \sqrt{s}

We have discussed the setup motivated by the proposed TDR of the ILC project. It would be also interesting to investigate how heavy dark matter can be in principle probed at future lepton colliders with very high energy center of mass energy. In such colliders with beam energy much higher than the TeV scale, the statistical error tends to dominate the systematic one, for di-fermion production cross sections scales as $1/s$. We therefore neglect the systematic uncertainty in this investigation and combine the e , μ , c and b channels in the analysis in order to estimate the ultimate

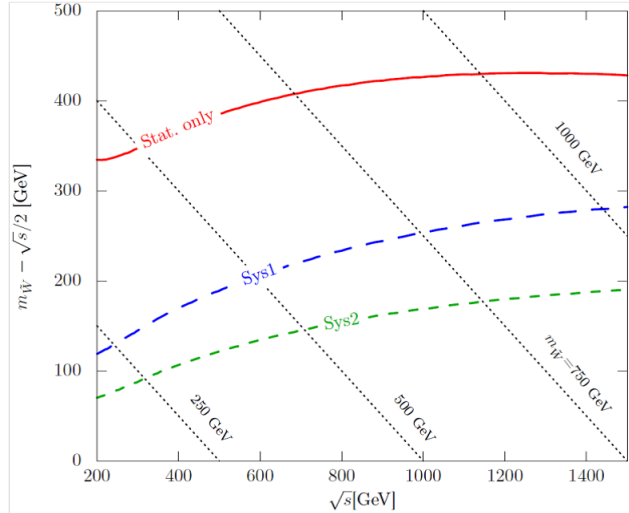


Figure 11: *Combined reach for wino. The differences between the expected reach of the EWIMP mass m at 95% C.L. and the beam energy $\sqrt{s}/2$ is shown. Here we assume that the integrated luminosity of 2 ab^{-1} and the electron and positron beam polarizations of -80% and $+60\%$. Sys.1 represents the combined result under the systematic errors of 0.2% for electron, 0.15% for muon, 0.5% for bottom, and 1% for charm while Sys.2 is estimated under the systematic errors of 0.4% for electron, 0.3% for muon, 1% for bottom, and 2% for charm.*

potential of future lepton colliders for the EWIMP search.

The capability of future lepton colliders to probe the LSP dark matters and the MDM discussed in previous subsection is shown in Fig. 12. The integrated luminosity is fixed to be $L = 1 \text{ ab}^{-1}$ (red solid lines) and 10 ab^{-1} (blue dashed lines), while the polarizations electron and positron beams are -80% and $+60\%$. The yellow-shaded band represents the upper bound from the thermal dark matter relics. As we expected in section 5.3, the sensitivity reaches are in good agreement with the scaling law $\sim s^{1/4} L^{1/4}$ although small deviations appear due to logarithm corrections.

5.6 Conclusion

In this section, we have studied the capability of future lepton colliders, such as ILC, CLIC, FCC-ee CEPC, to probe EWIMPs indirectly. Di-fermion production processes $e^-e^+ \rightarrow f\bar{f}$ is investigated as a suitable channel for this purpose when the mass of an EWIMP is much larger than the beam energy. We have found that the mass larger than the beam energy by 100-1000 GeV is actually detectable when systematic errors to measure the cross sections of the processes are well under control at $O(0.1)\%$ level. Especially for wino dark matter case, the combined analysis can

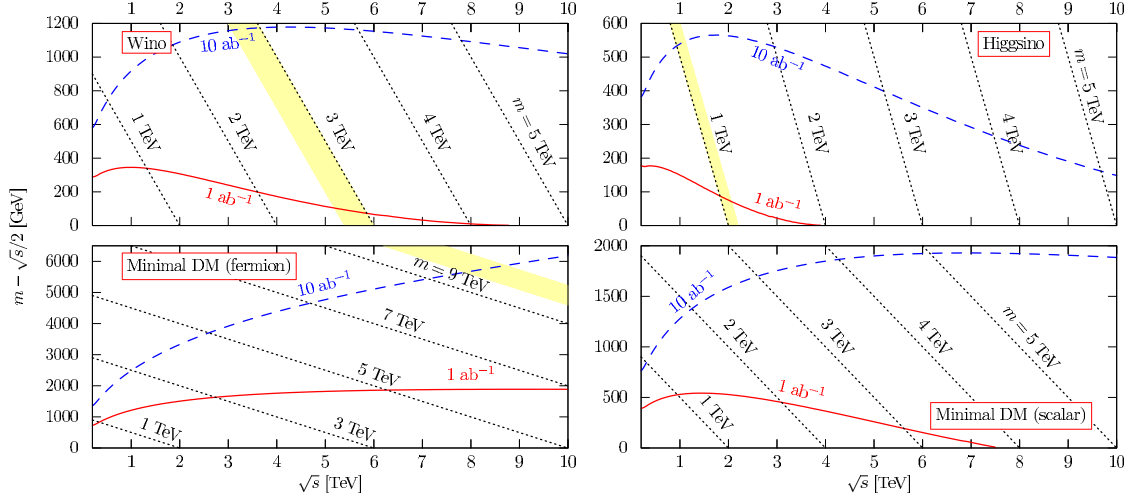


Figure 12: *Ultimate potential of future lepton colliders with large center of mass energy to probe the wino LSP, the Higgsino LSP and the two MDMs discussed in Sec. 5.4. The integrated luminosity is fixed to be 1 ab^{-1} (red solid lines) and 10 ab^{-1} (blue dashed lines), while the polarizations electron and positron beams are -80% and $+60\%$. Only the statistical uncertainty is taken into account in the analysis. In the yellow-shaded region, the thermal relic abundance of EWIMPs explains the observed abundance of dark matter in the present universe $\Omega h^2 \simeq 0.12$ [29, 87].*

exclude

$$m_{\tilde{w}} > 650 - 750 \text{ GeV} \quad (95\% \text{ C.L.}) , \quad (42)$$

at $\sqrt{s} = 1 \text{ TeV}$, $L = 2 \text{ ab}^{-1}$.

In the analysis, we adopted somehow optimistic and simplified assumptions on the collider setup. The systematic errors have actually many origins and thus more complicated. A detailed and realistic analysis will be necessary to conclude the capability of future lepton colliders for these indirect probes, while we expect that it does not alter our result so much and thus the di-fermion processes will play an important role to search for the EWIMP at the colliders.

Let us comment on other channels than di-fermion productions. As we have mentioned in Section 5.2, the effect of EWIMPs on the triple gauge couplings (e.g. $e^-e^+ \rightarrow Z/\gamma \rightarrow W^-W^+$) is not so useful, as far as $m \gg \sqrt{s}$. However, when the mass and the beam energy are close to each other, $m \simeq \sqrt{s}/2$, the description via dimension six operators is no longer valid. Especially, for an EWIMP with smaller n and Y like a Higgsino, the reach of di-fermion channels is not far above beam energy (see Fig. 9). In such a case, it is not easy to determine which modes, di-fermion or di-boson, is more suitable to search for EWIMPs. It is therefore interesting to study

also on the triple gauge boson couplings as a probe of EWIMPs. Another interesting phenomena may appear when $m \simeq \sqrt{s}/2$. In such a case, a nearly on-shell EWIMP bound states will appear as an intermediate state and may affect the production cross section significantly. Detailed analysis on this effect is beyond the scope of this article and we leave it as a future work.

6 Future constraints from indirect detections

In the near future, more and more cosmic-ray detection experiments will start. For the charged cosmic-ray observation, AMS-02 collaboration continues their observation and the anti-proton flux will be surveyed up to TeV energy range. Moreover, the next charged particle observations will be launched by CALET [145], DAMPE [146] collaboration from 2015, 2016 respectively. The gamma-ray measurements are also proceeded by the on-earth types (HESS-II [147], HAWC [148] and CTA [149]) and the satellite-types (GAMMA-400 [150], PANGU [151], HERD [152], CALET, and DAMPE) observations. Cherenkov Telescope Array (CTA) is one of the most promising future on-earth type gamma-ray observations, which will start the observation from 2017. Its line gamma-ray search toward the galactic center will catch the $\mathcal{O}(1-10)$ TeV dark matter annihilation signal with high sensitivity [153]. Here the wide field of view is expected to mitigate the dependence of the dark matter halo shape and background contamination. The optimization should be carefully discussed and therefore will be a future work. For the satellite-type observation, Fermi-LAT extends their operation till 2018. Moreover, the next gamma-ray observations will be performed by GAMMA-400, PANGU and HERD as well as CALET, DAMPE. Although their effective areas are slightly smaller than Fermi-LAT, the combined analysis will bring stronger constraints in the near future.^{#20}

For the prominent features discussed in Sec. 4.3 (clean, dark matter rich, and close to us) and the expectation to the future surveys, below, we discuss the future wino limits from the dSph gamma-ray observations based on our work [64]. In the discussion, we estimate a conservative limit by robustly considering the signal flux, backgrounds, and the capability of the detectors. We first evaluate how well our

^{#20} Interesting constraints will also be brought by the radio/hard X-ray observation of the cluster galaxies by SKA [154] and Astro-H [155], which will start their observation at 2020, 2015 respectively. Although the constraints depend on the model of the clusters, the dark matter annihilation is strongly constrained by these observations [156]. The estimation shows that the 100 hour observation gives $\mathcal{O}(10^{3-7})$ stronger constraints compared to the current Fermi sensitivity.

method to evaluate detection sensitivity works in Sec. 6.5 by comparing the method with the official one from the Fermi-LAT. After that, we discuss in Sec. 6.6 how severely the annihilation cross section can be limited in future, considering both Fermi-LAT and GAMMA-400 telescopes.

6.1 Flux formula

At a given energy E of the gamma-ray, the differential gamma-ray flux from wino dark matter annihilations in each dSph in a solid angle $\Delta\Omega$ is given by

$$\Phi(E, \Delta\Omega) = \left[\frac{\langle\sigma v\rangle}{8\pi m_{\tilde{w}}^2} \sum_f \text{Br}(\chi^0\chi^0 \rightarrow f) \left(\frac{dN_\gamma}{dE} \right)_f \right] \left[\int_{\Delta\Omega} d\Omega \int_{l.o.s.} dl \rho^2(l, \Omega) \right]. \quad (43)$$

$\text{Br}(\chi^0\chi^0 \rightarrow f)$ denotes the branching fraction of the annihilation into a final-state f , and $(dN_\gamma/dE)_f$, as introduced in Sec. 3.2, is the differential number density of photons for a given final state f , (i.e. the fragmentation function). The dark matter profile inside dSph is denoted by $\rho(l, \Omega)$. Here, l denotes the distance along the line-of-sight and Ω is the solid angle of an observational cone pointing to the center of the dSph. The part in first parenthesis is determined only by particle physics, which is discussed in Sec. 3.2, while the second one, which is called the J -factor $J(\Delta\Omega)$, is from astrophysics.

We note that since the annihilation cross sections of the wino dark matter has been calculated with the precision of a few percent level [74], the most dominant systematic error on the particle physics factor in equation (43) comes from the fragmentation functions. In particular, numerical simulations for quark fragmentations tend to give a large error, as discussed in Ref. [79, 157]. Fortunately, the wino dark matter annihilates mainly into electroweak gauge bosons, so that the simulations have been tuned very well by collider physics data. The systematic error associated with the particle physics factor is estimated to be at most 10%.

6.2 Astrophysical factor

The second term in the flux formula (43), called J -factor, is determined by the dark matter density profile inside a dSph, $\rho(l, \Omega)$. With α_{ROI} being the maximum angle between the observational cone and the direction to the dSph center, the J factor is defined by

$$J(\alpha_{\text{ROI}}) \equiv \int_{\Delta\Omega(\alpha_{\text{ROI}})} d\Omega \int_{l.o.s.} dl \rho^2(l, \Omega), \quad (44)$$

where the solid angle is given by $\Delta\Omega(\alpha_{\text{ROI}}) = 2\pi(1 - \cos\alpha_{\text{ROI}})$.

The dark matter profile is usually evaluated by comparing the mass-model of dSphs and the stellar kinematic data of the dSphs (e.g. velocity dispersions of stellar objects). Since dSphs are dark-matter-rich astrophysical objects, the stellar kinematics are governed mostly by how the dark matter is distributed inside the dSphs, namely the dark matter profile. The profile is generally assumed to be spherically distributed and described by the function [158]:

$$\rho(r) = \rho_s (r/r_s)^{-\gamma} [1 + (r/r_s)^\alpha]^{(\gamma-\beta)/\alpha}, \quad (45)$$

where r is the distance from the dSph center. Parameter γ determines the inner slope of the profile (say, cuspy or cored), β describes the outer slope, α controls the sharpness of transition from the inner to the outer slopes at a characteristic scale r_s , and ρ_s is a normalization factor. The profile is thus completely specified by evaluating five parameters, α , β , γ , r_s and ρ_s , from stellar kinematics. Notice that the so-called NFW profile ($\alpha = 1$, $\beta = 3$, $\gamma = 1$) [159] is adopted in many articles to reduce the free parameters. On the other hand, recent observations suggest another profile possibility which is cored at the center [160]. The most typical one is called the Burkert profile ($\alpha \simeq 1.5$, $\beta = 3$, $\gamma = 0$) [161].

The size of the observational cone in the J -factor (44) is usually taken to be around the half-light radius r_e , corresponding to the angle $\alpha_e \simeq r_e/d$ with d being the distance between dSph and us [162]. This choice minimizes the systematic error on the factor. That is, the choice of a much smaller α_{ROI} than α_e not only reduces the signal flux but also enhances the error of J -factor due to the decreasing stellar kinematic data. The much larger α_{ROI} than α_e also enhances the systematic error of the J -factor because the effect of dark matter substructures around the dSphs (e.g. dark matter clumps) is expected to contribute to the profile [163]. Besides, since the J -factor is proportional to dark matter density squared, the factor is not enhanced even if we take larger α_{ROI} . According to analysis by the Fermi-LAT collaboration, we take $\alpha = 0.5^\circ$ for all the dSphs in our analysis, which satisfies the above condition.

In our analysis, we use the four classical dSphs, Ursa Minor, Draco, Sculptor, and Sextans, because their locations are close to us (within 100 kpc) and give sizable contributions for the wino dark matter search. The J -factors of the other classical dSphs are negligibly small for the purpose. We use the J -factor values adopted in Ref. [108]. Information about the four dSphs is shown in Table 1. The median values and the errors of the J -factors were obtained by the Bayesian analysis assuming the NFW profile [164]. It is worth emphasizing that, because stellar kinematic data of

	long. (deg.)	lat. (deg.)	dist. (kpc)	α_s (deg.)	$\log_{10}[J(0.5^\circ)/(\text{GeV}^2\text{cm}^{-5}\text{sr})]$
Draco	86.4	34.7	76	$0.25_{-0.09}^{+0.15}$	18.8 ± 0.16
Ursa Min.	105.0	44.8	76	$0.32_{-0.12}^{+0.18}$	18.8 ± 0.19
Sculptor	287.5	-83.2	86	$0.25_{-0.13}^{+0.25}$	18.6 ± 0.18
Sextans	243.5	42.3	86	$0.13_{-0.05}^{+0.07}$	18.4 ± 0.27

Table 1: *The information about classical dSphs (Draco [166], Ursa Minor [166], Sculptor [167], Sextans [167]). long. (lat.) is the longitude (latitude) of the galactic coordinate. dist. denotes the distance from the earth to each dSph. α_s represents the dark matter halo size and $J(0.5^\circ)$ is J -factor with a cone radius of 0.5° . Both are from Ref. [108], where the two-level Bayesian hierarchical model [164] is used for the estimation.*

the four dSphs have already been accumulated enough [165], the maximum likelihood analysis can also evaluate their J -factors well even if we use the most generalized dark matter profile (45) [162]. The result of the maximum likelihood analysis turns out to be consistent with that from the Bayesian analysis, so that the estimation of the J -factors given in the table is robust.

For the ultra-faint dSphs, the data are too limited ($\lesssim \mathcal{O}(100)$) to evaluate the dark matter profile by the maximum likelihood analysis. In such a case, it is pointed out that the J -factor obtained from the fit has a large deviation by two orders of magnitude or more [168]. To minimize the deviation, most studies adopt the Bayesian analysis and impose a prior bias to the fit. In the Bayesian analysis, however, the choice of the prior turns out to significantly affect the posterior probability distribution of the J -factors [169]. In Ref. [108], they use the J -factors of the ultra-faint dSphs estimated by the two-level Bayesian hierarchical model [164] in order to avoid arbitrary choice of the prior probability. In this model, all dSphs are assumed to have some common relations among luminosity, maximum circular velocity, and the radius of the maximum velocity, and they are used in the bottom-level prior probability.^{#21} Validity of the use of the relations is, however, not guaranteed, because origins of the ultra-faint dSphs are still under debate and it is not clear whether or not such relations hold for all the dSphs. Thus, at this point, the dark matter constraint obtained from the ultra-faint dSphs seems less conservative. Meanwhile, many efforts are now being paid to obtain more kinematic data of the ultra-faint dSphs by deeply observing them, and the dSphs will eventually play important roles

^{#21}Explicit forms of the relations are determined based on simulations/observations [170] and they involve some free parameters. These parameters are evaluated using the data of all dSphs.

	long. (deg.)	lat. (deg.)	dist. (kpc)	α_s (deg.)	$\log_{10}[J(0.5^\circ)/(\text{GeV}^2\text{cm}^{-5}\text{sr})]$
Segue 1	220.5	50.4	23	$0.40_{-0.27}^{+0.86}$	19.5 ± 0.29
Ursa Maj. II	152.5	37.4	32	$0.32_{-0.19}^{+0.48}$	19.3 ± 0.28
Willman 1	158.6	56.8	38	$0.25_{-0.17}^{+0.54}$	19.1 ± 0.31
Coma B.	241.9	83.6	44	$0.25_{-0.17}^{+0.54}$	19.0 ± 0.25

Table 2: *The same as Table 1, but for the information about ultra-faint dSphs (Segue 1 [171], Ursa Major II [172], Willman 1 [173], Coma Berenices [172]).*

for detecting dark matter signals in (near) future. We will therefore involve ultra-faint dSphs in our analysis of future prospects, with errors on their J -factors being free parameters. Mean values of the J -factors are chosen according to the results in Ref. [108]. As is the same reason for the classical dSphs, the following four ultra-faint dSphs are used in our analysis: Segue 1, Ursa Major II, Willman 1, Coma Berenices, and information about the dSphs are shown in Table 2^{#22}

Finally, we note that there are other hidden biases for both the classical and ultra-faint dSph halo estimation such as halo truncation, non-sphericity, dispersion anisotropy, and foreground contamination. These biases might affect the median value of the J -factors above. In this section, we do not consider the detailed effects of them and further discussion will be given in Sec. 7.

6.3 Backgrounds

We discuss here astrophysical backgrounds against the dark matter signal from various dSphs, which originate in galactic diffuse emissions, isotropic diffuse emissions, and point source emissions. The galactic diffuse emissions come from the decay of neutral pions produced by the collision between the cosmic-ray (CR) and the interstellar medium (ISM), the bremsstrahlung of CR electrons in the ISM, and the inverse Compton scattering off the interstellar radiation field (ISRF). Gamma-ray emissions from large scale structures such as the hard-spectrum lobes (Fermi Bubbles) [174] and the giant radio loop (Loop I) [175] also contribute to the diffuse component. Any dSphs we are considering, which are shown in the tables in previous subsection, are not located on the directions of these structures. The isotropic emissions are, on the other hand, composed of several extragalactic contributions: active galactic nucleus, starburst galaxies, gamma-ray bursts, and other unknown

^{#22} In Table 2, the errors of the J -factors of the ultra-faint dSphs are also shown from Ref. [108], though we do not use them.

sources.^{#23} Point source emissions are mainly from active galaxies, mostly blazars. Supernova remnants and pulsars are also a part of the contribution. Furthermore, there are a large number of point sources which are not identified yet.

In our analysis, the astrophysical backgrounds are evaluated based on the background model provided by the Fermi-LAT collaboration. The galactic diffused emissions are estimated by the GALPROP code [176]. The simulation calculates the gamma-ray emission by using interstellar gas distributions (mainly HI and HII gasses) for the neutral pion production, the ISRF model for the inverse Compton scattering, and the models of the large structures. The isotropic emissions are, on the other hand, evaluated directly from the observational gamma-ray data of all-sky except the region $|b| < 30^\circ$, where b is the galactic latitude: the emissions are obtained by subtracting the galactic diffuse emissions and the point source emissions [177] from the data by using the profile likelihood analysis with their normalizations being free parameters. It is worth emphasizing that the Fermi-LAT collaboration estimated the uncertainty of the model by examining the different choice of the magnetic diffusion zone, the ISRF model, and the sky region. It then turned out that the choice does not make a large difference, which is in fact smaller than the uncertainty to determine the normalizations in the profile likelihood analysis.

Among various data of the astrophysical backgrounds provided by the Fermi-LAT collaboration [178], we use the data ‘gll_iem_v05.fit’ for the galactic diffuse background, which is obtained based on the highly sophisticated data-classification called ‘Pass 7’ [179, 180].^{#24} The isotropic diffuse background model is, on the other hand, released based on two different selection criteria; ‘Pass 7 SOURCE’ and ‘Pass 7 CLEAN’ [178]. Though the SOURCE class data gives a larger number of statistics, it contains a significant amount of misidentified CR contributions, especially at the energy region above 1 GeV [179]. In order to avoid such a contamination, we take the CLEAN class data ‘iso_clean_v05.txt’. Emissions from point and unrated sources which are overlapped with the signal region (which is defined as a $1.0^\circ \times 1.0^\circ$ square pointing to a dSph in this article) may change the background normalization. Since

^{#23}Dark matter annihilations in our galactic halo and those of extra-galaxies also contribute to the isotropic emissions, though they are smaller than the other contributions [107]. Furthermore, since the isotropic emissions are evaluated with the direct use of Fermi-LAT diffuse gamma-ray data as mentioned in following discussion, the contributions do not affect our analysis at all.

^{#24} Recently, Fermi updates the pass criteria into ‘Pass 8’ [63] which adopts more sophisticated event selection algorithm and the capabilities are improved by 10-30 percent level. The ‘Pass 8’ can easily be applied to our work and we expect 20 – 40 % improvement will be obtained in our future expectation. The detailed work will be explored in the future.

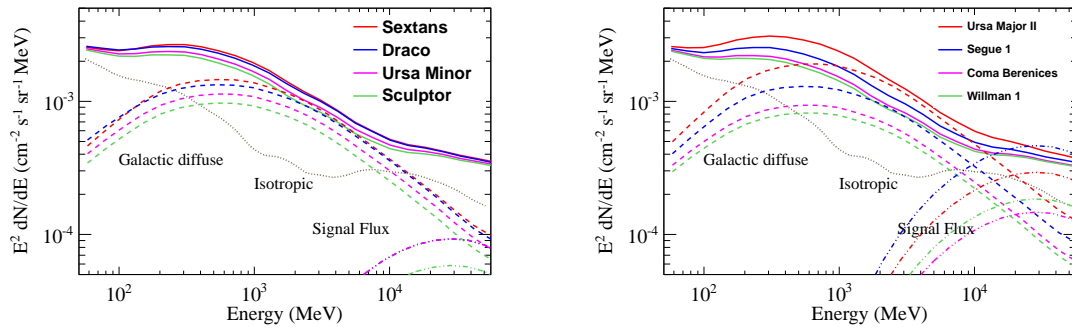


Figure 13: Astrophysical background fluxes per unit solid angle averaged over the signal region for classical (**left panel**) and ultra-faint (**right panel**) dSphs as a function of the gamma-ray energy. Galactic and isotropic diffuse components are shown as broken and dotted lines, respectively, while their sums are shown as solid lines. The dot-dashed lines are the signal fluxes obtained by the formula (43), where we set $m_{\tilde{w}} = 500 \text{ GeV}$ and assume the Fermi-LAT capability.

the change is estimated to be at most $\mathcal{O}(10)\%$ level [181], we neglect their contributions to the astrophysical backgrounds. The background flux is then estimated by integrating galactic and isotropic diffuse emissions over the signal region. The background flux per unit solid angle averaged over the signal region is shown in Fig. 13 as a function of the gamma-ray energy for each classical/ultra-faint dSph.^{#25} We have checked that the background flux is not altered even if we use larger region: e.g. averaging over a $5^\circ \times 5^\circ$ square gives at most 10 percent deviation.

6.4 Detector capabilities

The number of signal and background events in actual observations depends on not only their fluxes but also the capability of detectors (gamma-ray telescopes). In our analysis, we consider the Fermi-LAT [182] and the future projected GAMMA-400 [150] telescopes.^{#26} Such kind of satellite-borne gamma-ray telescopes can cover

^{#25}Since no significant gamma-ray excesses have been observed yet for all the directions of the dSphs, it is good enough to estimate the diffused background averaged over the signal region.

^{#26} On-earth type telescopes, such as H.E.S.S [147], MAGIC [183], VERITAS [184], HAWC [148] and CTA [149] are also important gamma-ray detector, which has quite large effective area and high angular resolution. However, because of the limited exposure time, it is difficult to achieve a competitive sensitivity to the satellite types when we consider the dSph continuum gamma-ray search. For the line signal search, on the other hand, thanks to the high angular resolution and the wide range of the energy region, the line signal from the $\mathcal{O}(1)$ TeV wino can be efficiently explored.

the whole sky region and thus efficiently accumulate the signal events from various dSphs.^{#27} The most important aspect of the capability is from the effective area, the angular resolution called point spread function (PSF), and the energy resolution; those are often called the instrumental response functions (IRFs). The effective area is determined by the gamma-ray conversion rate induced by a thin foil in the detectors, and depends also on event identification algorithm. The left panel of Fig. 14 is showing the energy dependence of the effective area using the CLEAN class IRF, ‘P7REP_CLEAN_V15’ [185], for the Fermi-LAT and the IRF in Ref. [186] for the GAMMA-400. It can be seen that the area of the GAMMA-400 is 40–100% smaller than that of the Fermi-LAT, though the energy range covered by the former telescope (0.1–3000 GeV) is much larger than that of the latter one (0.1–500 GeV). The PSF is mainly determined by the strip geometry of the detectors and the track reconstruction uncertainty from the multiple scattering of created electrons. The latter factor becomes significant for low-energy gamma-rays, as shown in the middle panel of Fig. 14. The PSF of the GAMMA-400 is substantially smaller than that of the Fermi-LAT when $E \gtrsim 10^4$ MeV. The energy resolution is determined by the energy loss inside the tracker and the shower leakage inside the electromagnetic calorimeter. Though very energetic gamma-rays with $E \gtrsim 100$ GeV rarely deposit their energies inside the calorimeter, the energies are deduced from a sophisticated shower imaging analysis. The right panel of Fig. 14 shows the energy resolution. It can be seen that the GAMMA-400 covers wider energy range and gives better resolution thanks to the thick calorimeter.

Using the IRFs presented in Fig. 14, the number of signal and background events (S_{ai} and B_{ai}), which is obtained in actual observation of the dSph ‘a’ at the ‘i’-th energy bin having the width of ΔE_i , is estimated as

$$S_{ai} = t_{\text{obs}} \times \int_{\Delta E_i} dE \mathcal{F}_a^{(S)}(E, \Delta\Omega_i) A_{\text{eff}}(E) , \quad (46)$$

$$B_{ai} = t_{\text{obs}} \times \int_{\Delta E_i} dE \mathcal{F}_a^{(B)}(E, \Delta\Omega_i) A_{\text{eff}}(E) , \quad (47)$$

where t_{obs} and $A_{\text{eff}}(E)$ are the exposure time and the effective area, respectively. We use 25 energy bins with logarithmically equal width in the range of 0.5 GeV to 500 GeV, namely the i-th bin has the center value of $E_i = 0.5 \times 10^{0.125(i-1)}$ GeV with

In this case most promising target is the center of the Milky Way galaxy, which requires a careful treatment of the dark matter profile and the background. The investigation is beyond the scope of this thesis and will be a future work.

^{#27}The proton rejection factor is also better than other kinds of telescopes, which is estimated to be 10^4 for the Fermi-LAT telescope and 10^6 for the GAMMA-400 telescope, respectively.

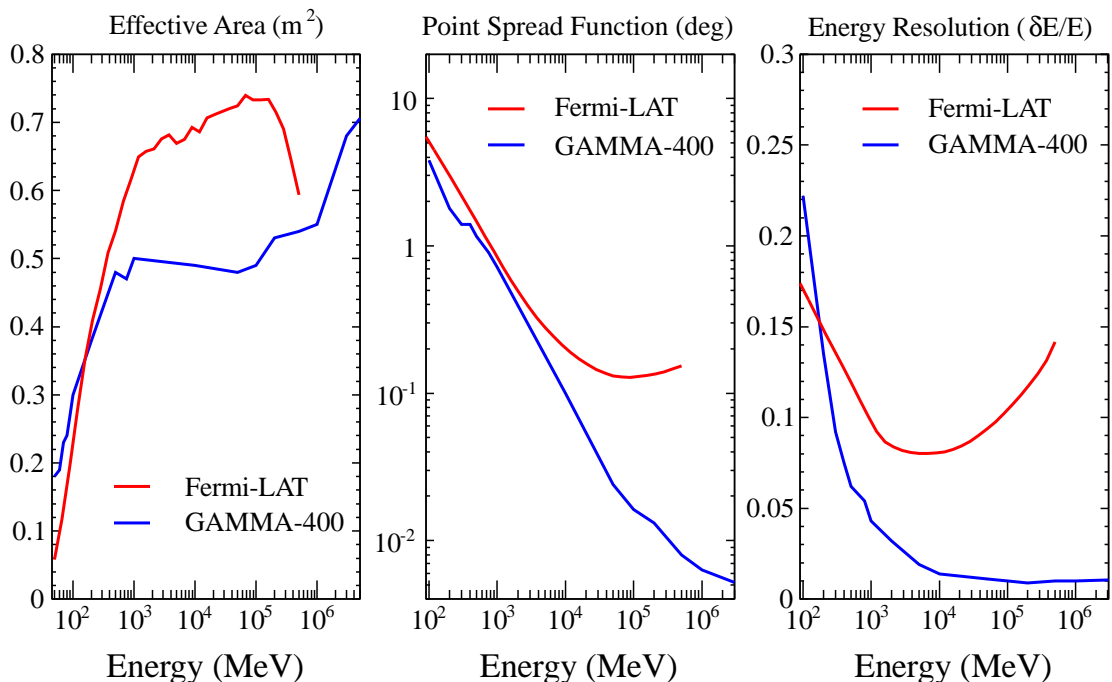


Figure 14: The effective area (**left panel**), the point spread function (PSF) (**middle panel**), and the energy resolution (**right panel**) are shown as a function of the gamma-ray energy (in unit of MeV). Both cases for the Fermi-LAT [185] and the GAMMA-400 telescopes [186] are shown in each figure as red and blue lines, respectively.

the width of $\Delta E_i/E_i \simeq 0.29$. This choice gives sufficiently large bin-width compared to the energy resolution shown in Fig. 14. The solid angle $\Delta\Omega_i$ is determined as follows. Though the dark matter profile in each dSph is, as discussed in Sec. 6.2, well concentrated within the circular region with an angular radius of 0.5° , the signal events from the dSph are diffused due to the detector effect. We therefore choose the angle as $\Delta\Omega_i = 2\pi(1 - \cos \alpha_i)$ with $\alpha_i = [(0.5^\circ)^2 + \psi_{68}^2(E_i)]^{1/2}$ to collect most of the signal events. Here, ψ_{68} is the 68% containment angle (PSF) shown in Fig. 14. This choice means the region of interest (ROI) is set to be the circular region with the radius of α_i . The signal and background fluxes are then given by

$$\mathcal{F}_a^{(S)}(E, \Delta\Omega_i) = \epsilon(\Delta\Omega_i) \Phi_a(E, \Delta\Omega_i), \quad \mathcal{F}_a^{(B)}(E, \Delta\Omega_i) = \Delta\Omega_i (d\Phi_a^B(E)/d\Omega), \quad (48)$$

where $\Phi_a(E, \Delta\Omega_i)$ is the signal flux from the dSph ‘a’ given by the formula (43),^{#28} while $d\Phi_a^B(E)/d\Omega$ is the averaged background flux per unit solid angle shown in

^{#28}Since the dark matter profile inside each dSph is concentrated within the circular region with the radius of 0.5° , the following approximation, $\Phi_a(E, \Delta\Omega_i) \simeq \Phi_a(E, \Delta\Omega_{0.5^\circ})$, is used in our analysis with good accuracy, where $\Delta\Omega_{0.5^\circ}$ denotes the solid angle with the angular radius of 0.5° .

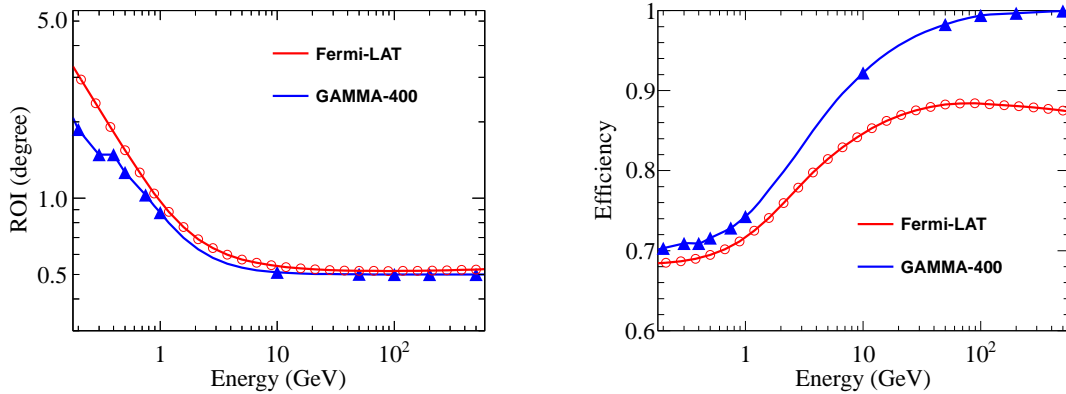


Figure 15: **Left panel:** The angle defining the ROI (i.e. α_{ROI}) used in our analysis as a function of the gamma-ray energy. (The ROI is defined by the circular region with this angle.) **Right panel:** The efficiency factor $\epsilon(\Delta\Omega_i)$ as a function of the energy.

Fig. 13. The observed signal is smeared by the detector capability and therefore the amount of the signal flux in the ROI is reduced. The efficiency factor $\epsilon(\Delta\Omega)$ is introduced to take this loss of highly diffused signal events into account. In order to calculate $\epsilon(\Delta\Omega)$, the function provided in Ref. [179] is used to describe the angular distribution of the diffusion effect for the Fermi-LAT, while the Gaussian distribution with the width of ψ_{68} is assumed for the GAMMA-400. Both the angle of ROI (i.e. α_{ROI}) and the efficiency factor are shown in Fig. 15 as a function of the gamma-ray energy. It can be seen that the ROI is governed by the PSF and thus the efficiency factor is about 0.68 when $E < 1$ GeV, while it is close to one when $E > 10$ GeV because the PSF becomes negligibly small compared to the angle 0.5° (especially for the GAMMA-400). The examples of the signal fluxes are also shown in Fig. 13, where we set $m_{\tilde{w}} = 500$ GeV and assume the Fermi-LAT capability.

With the use of signal and background events (S_{ai} and B_{ai}) and also the uncertainty of the J -factor discussed in Sec. 6.2, the sensitivity to detect the dark matter signal at each telescope, Fermi-LAT and GAMMA-400, can be obtained by the maximum joint likelihood estimation [108]. The joint likelihood function is constructed

by the product of the likelihood function [187] for each dSph,^{#29}

$$\mathcal{L}[\langle\sigma v\rangle, \{J_a\}] \equiv \prod_{a,i} \frac{P(N_{ai}; S_{ai}[\langle\sigma v\rangle, J_a] + B_{ai})}{P(N_{ai}; N_{ai})} G(J_a; \log_{10} J_a^{(\text{obs})}, \delta(\log_{10} J_a^{(\text{obs})})) \quad (49)$$

where $P(N; \lambda)$ and $G(x; \mu, \sigma)$ are the Poisson and the Log Gaussian distributions, respectively, while $\log_{10} J_a^{(\text{obs})}$ and $\delta(\log_{10} J_a^{(\text{obs})})$ are the observed J -factor and its error of the dSph ‘a’. The number of events at the ‘i’-th energy bin obtained by observing the dSph ‘a’ is denoted by N_{ai} . Since we are interested in how severely the annihilation cross section can be constrained with the dark matter mass being fixed in future gamma-ray observations, the number of the signal events S_{ai} depends only on the cross section $\langle\sigma v\rangle$ and the J -factor J_a . Because of the same reason, the number of events N_{ai} in our analysis is generated as a mock data following the Poisson distribution with the mean B_{ai} . Maximizing the joint likelihood function with respect to the nuisance parameters J_a , namely $-2 \ln \mathcal{L}(\langle\sigma v\rangle, \{J_{\min}\}) + 2 \ln \mathcal{L}(0, \{J_{\min}\}) = 2.71$, gives the expected upper limit on the cross section at 95% confidence level. Here, $\{J_{\min}\}$ represents the set of J -factors maximizing the likelihood function for each $\langle\sigma v\rangle$. Using methods developed in this section, we discuss the capability of future dSph observations to explore the wino dark matter in next section.

6.5 Validating our method

We are now at the position to discuss how well our method developed in previous section works to give detection sensitivity for the wino dark matter. We consider the eight dSphs discussed in Sec 6.2. For that purpose, we performed pseudo-experiment 2000 times, where N_{ai} in equation (49) is generated from the Poisson distribution with the mean value B_{ai} . The expectation band (fluctuation) is then obtained by the following procedure, which is also adopted in the Fermi-LAT collaboration: We first calculate the upper limit on the annihilation cross section $\langle\sigma v\rangle$ at 95% confidence level in each generated mock data with the dark matter mass being fixed. Here, we use the instrumental response functions of the Fermi-LAT assuming data of four years. As a result, we obtain 2000 limits on $\langle\sigma v\rangle$ for each dark matter mass thanks

^{#29} Here we consider one bin analysis for the spatial distribution of the signal flux. In the Fermi LAT analysis, the flux is also spatially binned, which enhances the power of the test. On the other hand, we do not consider the efficiency of the exposure time and the angular dependence of the effective area, which enhances our rejection power. In the next work, we will take into account these factors. However, we expect that involving these two factors do not significantly change the result because we can successfully reproduce the Fermi official result (as shown in Fig. 16) thanks to the cancellation of these factors.

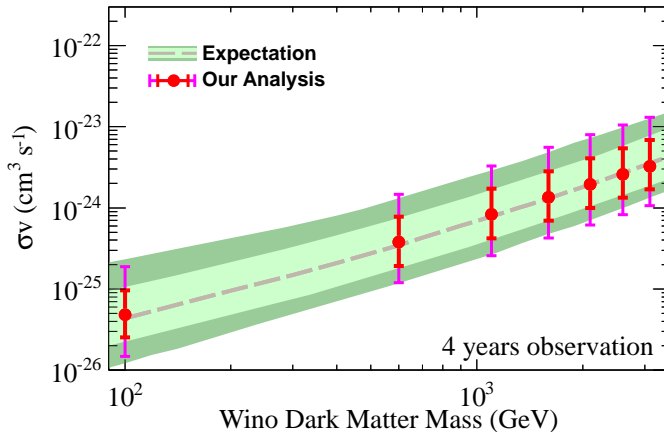


Figure 16: Comparison between our method and Fermi-LAT’s one on the expected limit on $\langle\sigma v\rangle$ at 95% confidence level. See text for more details.

to 2000 generation of mock data. We then calculate the mean value and its 68% and 95% fluctuations of the limit by observing the distribution of the 2000 limits.

The median values and their 68% (95%) fluctuations of the limit on the cross section $\langle\sigma v\rangle$ are shown in Fig. 16 for several dark matter masses, which are depicted as red circles and red (orange) bars, respectively. Those officially from the Fermi-LAT collaboration are also shown in the same figure. It can be seen that not only the median values but also their fluctuations obtained by our method are in good agreement with those from the Fermi-LAT collaboration. It is worth mentioning again that, even if we include the other seven dSphs which are not listed in the tables in the previous section, the result is little changed because the J -factors of these seven dSphs are small compared to the eight dSphs we have used.

6.6 Expected future limit

Here, we give our final results on how widely the mass of the wino dark matter will be explored in (near) future from the gamma-ray observation of dSphs. Two main progresses are expected in this program:^{#30} One is the accumulation of more data at the Fermi-LAT and the future projected GAMMA-400 telescopes, and another is the improvement of J -factor estimations (especially for ultra-faint dSphs) by obtaining kinematical data of the dSphs accurately. According to these expectations,

^{#30}There may be another progress if we discover new dwarf spheroidal galaxies giving large J -factors, for example, by the DES and LSST surveys. See Ref [188] for more details.

as near future prospect, we first discuss detection sensitivity (expected future limit) obtained by ten years data of the Fermi-LAT observation assuming $\delta(\log_{10} J) = 0.2$ for ultra-faint dSphs. We next demonstrate detection sensitivity expected from fifteen years data-taking at the Fermi-LAT observation plus ten years data-taking at the GAMMA-400 observation as optimistic but realistic future prospect. Finally, we consider what kind of effort and additional observation are required in future to explore entire mass region of the wino dark matter.

The expected future limit at the first case is shown in the upper panel of Fig. 17. Ten years data-taking at the Fermi-LAT observation is the one officially guaranteed by the collaboration [189]. On the other hand, the logarithmic errors of the J -factors for ultra-faint dSphs, $\delta(\log_{10} J_{\text{UF}}) = 0.2$, stems from the fact that current errors for classical dSphs are around 0.2 and from the expectation that deep kinematical survey for ultra-faint dSphs in future will achieve this accuracy. For example, the Prime Focus Spectrograph (PFS) of the SuMIRe Project [190] will be available for this purpose. It is designed to provide a wide field of view (0.65° radius), which is four–five times wider than DEIMOS-KEK [191], keeping an accurate wavelength resolution $R \equiv \lambda/\delta\lambda \sim 5000$ at most. Here, λ represents the wavelength of the light covering from 0.38 to 1.3 μm . Capability of the PFS leads to a large number of kinematical data with high accuracy and we expect that the condition $\delta(\log_{10} J_{\text{UF}}) = 0.2$ will be satisfied in future.^{#31} In such a case, from the figure, the wino dark matter with $m_{\tilde{w}} \leq 810 \text{ GeV}$ and $1.86 \text{ TeV} \leq m_{\tilde{w}} \leq 2.7 \text{ TeV}$ will be explored at 95% confidence level.

We next consider how the capability of the dSph observation is increased when the GAMMA-400 data becomes available. The expected future limit in this case is shown in the middle panel of Fig. 17, where fifteen years data at the Fermi-LAT observation plus ten years data at the GAMMA-400 observation is assumed with keeping the errors of the J -factors for ultra-faint dSphs being the same as previous case, $\delta(\log_{10} J_{\text{UF}}) = 0.2$. The combined analysis of the Fermi-LAT and the GAMMA-400 observations has been performed using the likelihood function constructed by the product of their event likelihoods discussed in previous section. It then turns out from the figure that the wino dark matter with $m_{\tilde{w}} \leq 1.0 \text{ TeV}$ and $1.66 \text{ TeV} \leq m_{\tilde{w}} \leq 2.77 \text{ TeV}$ will be explored at 95% confidence level. It is worth mentioning that, though the effective area of the GAMMA-400 telescope is smaller than that of the Fermi-LAT, the accurate point spread function above 10 GeV guarantees enough

^{#31} The detailed impact of PFS is investigated in Sec. 7.

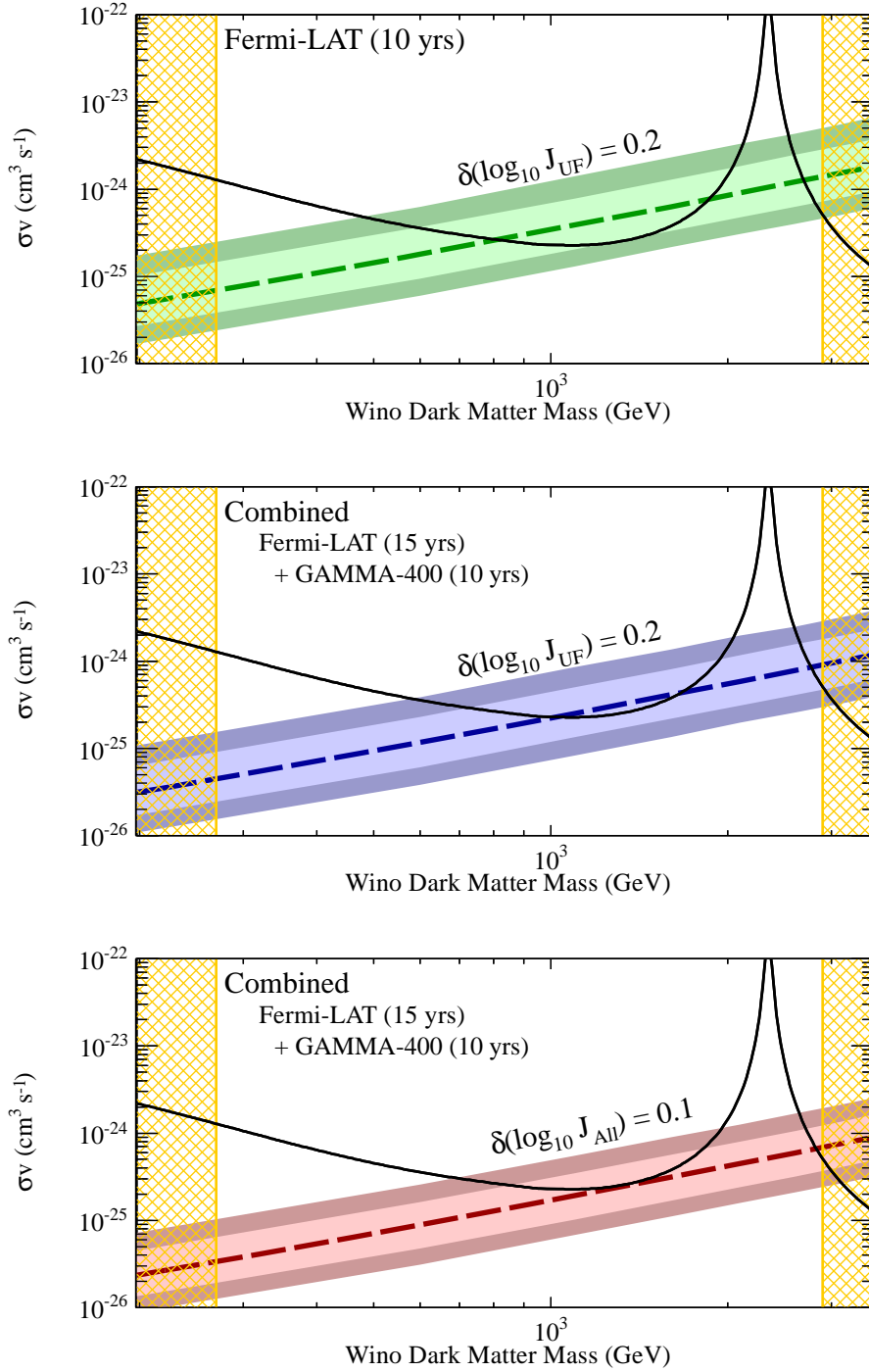


Figure 17: *Expected future limits on the dark matter annihilation cross section assuming ten years data at the Fermi-LAT and $\delta(\log_{10} J_{\text{UF}}) = 0.2$ (Upper panel), fifteen years data at the Fermi-LAT plus ten years data at the GAMMA-400 and $\delta(\log_{10} J_{\text{UF}}) = 0.2$ (Middle panel), and the same as the middle panel but $\delta(\log_{10} J_{\text{All}}) = 0.1$ (Lower panel). Orange-meshed regions correspond to the limits from the collider search (lower bound) and the thermal relic abundance (upper bound) of the wino dark matter, respectively.*

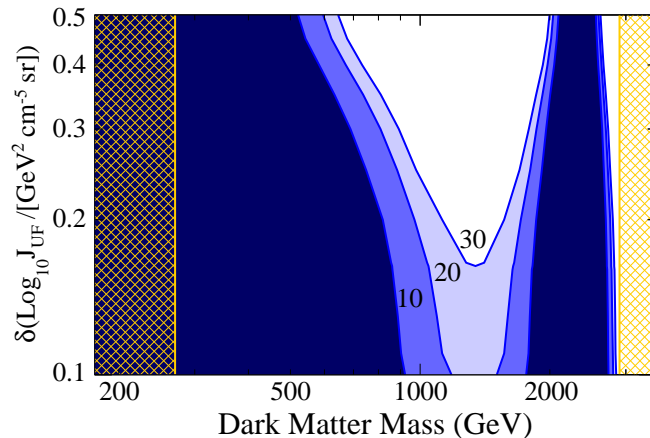


Figure 18: *Expected limits on the wino mass at 95% confidence level as a function of $\delta(\log_{10} J_{\text{UF}})$ (vertical axis) assuming 10, 20, and 30 years data-taking at the Fermi-LAT. Orange-meshed regions correspond to the limits from the collider search (lower bound) and the thermal relic abundance (upper bound) of the wino dark matter, respectively.*

efficiency to detect the dark matter. In fact, the capability of the GAMMA-400 observation is almost comparable to that of the Fermi-LAT.

As shown in the middle panel of Fig. 17, the most of the parameter region for the wino dark matter mass will be covered in future by the dSph observation; it is however not complete and some small regions ($m_{\tilde{w}} \sim 1.5$ TeV and 3 TeV) still remains uncovered. We therefore consider what kind of effort is needed to explore the entire mass region. The simplest solution is, of course, to observe dSphs using telescopes having larger effective area than those of the Fermi-LAT and the GAMMA-400. It is, on the other hand, not obvious whether or not such a costly plan is realized in (near) future. Another solution is to improve estimation of J -factors for both classical and ultra-faint dSphs, which requires very precise kinematical data for each dSphs. In the bottom panel of Fig. 17, the expected future limit is shown assuming that the J -factors for all the eight dSphs are succeeded to be determined at the level of $\delta(\log_{10} J_{\text{All}}) = 0.1$. Here, gamma-ray data is assumed to be the same as previous case (fifteen years data at the Fermi-LAT plus ten years data at the GAMMA-400). It can be seen from the figure that entire mass region (from 270 GeV to 2.9 TeV) can be covered in such a case. This fact indicates that not only increasing gamma-ray data but also decreasing the error of the J -factor for each dSph are important to cover the entire mass region of the wino dark matter, namely to completely test the high scale SUSY models.

Finally, it is worth showing that how much of the gains are expected from better measurements of the J -factors in comparison with larger data set from the Fermi-LAT observation. Expected limits on the wino mass at 95% confidence level are shown in Fig. 18 as a function of $\delta(\log_{10} J_{\text{UF}})$ (vertical axis) assuming 10, 20, and 30 years data-taking. It can be seen from the figure that dramatic improvement of detection sensitivity can be achieved by determining the J -factors accurately.

6.7 Conclusion

We have thoroughly investigated detection possibility of the wino dark matter in (near) future using the gamma-ray observation of dSphs. We have carefully discussed the dark matter density profile inside each dSph, astrophysical backgrounds against the wino dark matter detection, and the capability of present and future gamma-ray telescopes. All of the issues are mandatory to give robust prospect for the wino dark matter search in (near) future gamma-ray observation.

The limit of the wino dark matter mass will be expanded to $810 \text{ GeV} \leq m_{\tilde{w}} \leq 1.86 \text{ TeV}$ and $2.7 \text{ TeV} \leq m_{\tilde{w}} \leq 2.9 \text{ TeV}$ using ten years data of the Fermi-LAT when the J -factors of ultra-faint dSphs are determined with its accuracy of $\delta(\log_{10} J_{\text{UF}}) = 0.2$ and no signals are obtained at the observation. When the GAMMA-400 data becomes available, the limit is further improved to $1.0 \text{ TeV} \leq m_{\tilde{w}} \leq 1.66 \text{ TeV}$ and $2.77 \text{ TeV} \leq m_{\tilde{w}} \leq 2.9 \text{ TeV}$. Here, fifteen years data of the Fermi-LAT and ten years data of the GAMMA-400 are assumed. In addition, we have considered what kind of effort is eventually needed to search for entire mass region of the wino dark matter. Putting the possibility to have more powerful gamma-ray telescopes aside, the improvement of J -factors for both classical and ultra-faint dSphs will play an important role for this purpose.

7 Impact of the dSphs survey in the future

In the previous section, we have investigated the future potential of the gamma-ray detection and found that the J -factor errors give a significant impact on the sensitivity line. This fact enhances the importance of the precise understating of the systematic errors in the J -factor estimation. Below, we present various systematic errors hidden in the estimation: prior bias, dispersion anisotropy, halo truncation, non-sphericity, and foreground contamination. Although these effects are non-negligible, they are usually not taken into account even for the classical dSphs.

We can expect that the detailed analysis using future kinematical data will resolve and reduce these systematics. However, even for the future survey, the foreground contamination from the Milky Way stars still remains and rather becomes large. Therefore, it is no doubt that the treatment of the foreground contamination will be a key to the precise halo estimation in the future. In this section, we investigate the impact on the future spectroscopic survey and provide the new method to take into account the foreground contamination.

7.1 Astrophysical factor revisited

As discussed in Sec. 6.2, the second parenthesis in the right hand side of equation (43), so called J -factor, represents the amount of the dark matter in the halo which is deduced from astrophysical observation. Using the kinematical data obtained from the spectroscopic survey, many studies provide the estimation of the J -factors. In Sec. 6.2, we have reviewed the Bayesian Hierarchical Modeling method [164], where they fit the dark matter halo parameter by imposing the relations between the maximum velocity, maximum radius and total luminosity using the data of all dSphs. On the other hand, one can also directly estimate the dark matter halo by comparing the stellar velocity data with the theoretical dispersion curve.^{#32} The dispersion curve is usually obtained from the Jeans equation [192] under the assumption of the spherical symmetry and steady (and dark matter dominate) system, which is expressed as

$$\frac{1}{\nu_*(r)} \frac{\partial}{\partial r} (\nu_*(r) \sigma_r^2) + \frac{2\beta_{\text{ani}}(r) \sigma_r^2}{r} = -\frac{GM(r)}{r^2}, \quad (50)$$

where r again denotes the distance from the dSph center and $\nu_*(r)$ is the number distribution of the dSph member stars obtained from photometric observations. The velocity dispersions of the stars in the dSph are defined by σ_r , σ_θ , and σ_ϕ which denote the components along the radial, azimuthal, and polar direction respectively. The anisotropy parameter β_{ani} is defined by $\beta_{\text{ani}} = 1 - (\sigma_\theta^2 + \sigma_\phi^2)/2\sigma_r^2$. G is the gravitational constant and $M(r)$ is the enclosed mass of the dark matter halo. We give the detailed derivation in appendix A.

To compare this velocity dispersion with the observables, one should project it along the line-of-sight. By a straightforward calculation (see appendix A for detail),

^{#32} Here we note that a spectrograph can only measure stellar velocities along the line-of-sight, and they cannot be directly used for the halo estimation.

one can find that the projected dispersion curve $\sigma_{l.o.s}$ is given by

$$\sigma_{l.o.s}^2(R) = \frac{2}{\Sigma_*(R)} \int_R^\infty \left(1 - \beta_{\text{ani}}(r) \frac{R^2}{r^2}\right) \frac{\nu_*(r) \sigma_r^2(r)}{\sqrt{1 - R^2/r^2}} dr, \quad (51)$$

where R denotes the projected distance from the dSph center and $\Sigma_*(R)$ is the projected stellar distribution obtained by integrating $\nu_*(r)$ along the projected direction. The fit is performed by comparing the observed $\sigma_{l.o.s}$ and the equation (51) obtained by several fitting parameters (typically the halo profile parameter and velocity anisotropy) with respect to R .

Recently, however, it is pointed out that there exist non-negligible systematic errors hidden in the halo estimation: the prior bias, velocity anisotropy, halo truncation, non-sphericity, and foreground contamination.

The prior bias is required for the fit with small observational data. As discussed in Sec. 6.2, when the number of the observed stars is small, the J -factor obtained from the fit does not converge well and has a large deviation (by two orders of magnitude or more). Therefore, most studies evaluate the J -factor by imposing the prior bias [164] or imposing the empirical parameter cut [168]. However, Ref. [169] reveals that the choice of the prior strongly affects the halo estimation by at most two orders of magnitude for ultra-faint dSph fit. Thus, conservatively speaking, one should be careful when considering the gamma-ray sensitivity lines including the contribution from the ultra-faint dSph.

The velocity anisotropy $\beta_{\text{ani}}(r)$ is another subject of discussion. Because the anisotropy parameter cannot be directly addressed, one should make assumptions on the spatial dependence of the anisotropy. Currently, most studies assume that the anisotropy is r -independent, while the recent study [168] fits the kinematical data by using the Baes & van Hase parametrization [193]. Although it is pointed out that the anisotropy parameter might give a non-negligible effect on the J -factor estimation [194], the quantitative discussion is not enough and should be investigated in the future.

Another systematic error comes from the morphology of the outer halo. Even for the classical dSphs with ~ 500 member stars, the fit often allows quite a large dark matter halo radius (even more than 100 kpc) with small dark matter density [195] because the star kinematics does not provide the information over the outermost star. Although the dark matter halo may be truncated at some distance by the effect of the tidal stripping, there is no consensus on the truncation radius. One can calculate the tidal radius of the dSphs by assuming the Milky Way halo mass and profiles. Another conservative approach is to consider the distance of the outermost

star as a lower bound of the truncation radius. Because smaller truncation radius gives smaller J -factor, this lower bound method always provides conservative results. In this discussion, we also adopt the latter estimation.

Recent studies also test the contribution from the non-sphericity. Although most calculations assume the spherical dark matter halo for simplicity, there is no reason why the dark matter halo should be spherical. Ref. [168] estimates the effect of the non-sphericity using mock stellar sample and shows that the non-sphericity may affect the J -factor by a factor of two. The axis-symmetric fit is also performed by Ref. [196], which provides additional 60–100% deviation to the spherical estimation.

Finally, foreground contamination can also be a non-negligible systematics for the J -factor estimation. The observed data always includes the stars belonging to the Milky Way galaxy. Among them, dSph member stars are identified by utilizing the star information such as its position, velocity, color, metallicity, effective temperature and surface gravity. However, it is still difficult to absolutely eliminate the foreground contamination and Ref. [197] reveals that the profile estimation of the ultra-faint dSph (Segue I) is significantly affected by the ‘marginal’ stars which cannot be identified well. In the Segue I case, the overestimation of the J -factor reaches more than two orders of magnitude. The study also shows that the overestimation generally occurs when the number of the observed star is $\lesssim \mathcal{O}(100)$.

It is difficult to significantly reduce these systematic errors with the current kinematical data. The simplest way to resolve them is to increase the number of the observed stars and therefore the future spectroscopic survey toward the dSphs is highly motivated from the points of view of the dark matter detection. The foreground contamination, however, remains problematic because the number of the foreground stars also increases with the deeper, wider survey. The next section is devoted to investigate the potential of the future spectroscopic survey and the optimization of this foreground contamination by introducing a new likelihood.

7.2 Analysis

In the analysis, we first generate realistic mock dSph stellar data including the foreground stars. To clarify the effect from the contamination, the mock dSph stars are generated assuming the spherical distribution and constant the velocity anisotropy. Using this mock data, we test the capability of the future spectrograph and discuss the efficient data cuts. Finally, we propose a likelihood function to eliminate the foreground bias efficiently and fit the mock observed data using the likelihood

dSph	d [kpc]	r_e [pc]	(g, l)	v_{dSph} [km/s]
Draco	76	211	(86.4, 34.7)	-292
Ursa Minor	76	181	(105, 44.8)	-247

Table 3: *The properties of the galaxies which are given in Ref. [199] and references therein. d denotes the distance to the dSph. (g, l) are the longitude and latitude of each dSph. Here the galactic coordinates are used. The bulk velocity of each dSph is given by v_{dSph} . The negative sign represents that the dSph goes away from the earth.*

dSph	$\log_{10}(\rho_s/[M_{\odot}/\text{pc}^3])$	$\log_{10}(r_s/[\text{kpc}])$	α	β	γ	β_{ani}
Draco 1	-2.05	3.96	2.78	7.78	0.675	0.130
Draco 2	-1.52	3.15	2.77	3.18	0.783	-0.005
Ursa Minor	-0.497	2.60	1.64	5.29	0.777	-0.475

Table 4: *The dark matter halo parameter of each dSph.*

function. Here, the fit is performed under the same assumption above (spherical, constant anisotropy).

7.2.1 Dark Matter halo and stellar distribution

We adopt the generalized density profile introduced in equation (45) as the input dark matter profile for the mock data and fit:

$$\rho(r) = \rho_s (r/r_s)^{-\gamma} [1 + (r/r_s)^{\alpha}]^{(\gamma-\beta)/\alpha}. \quad (52)$$

We also assume Plummer profile [198] for the member stellar distribution:

$$\nu_*(r) = (3/4\pi r_e^3) (1 + (r/r_e)^2)^{-5/2}, \quad (53)$$

where r_e again denotes the projected half-light radius of the dSph. Here, we normalize $\nu_*(r)$ to $\int 4\pi r^2 \nu_*(r) dr = 1$.

7.2.2 Mock dSphs

We construct the mock dSphs based on the classical dSphs data with large J -factor where the number of the current observed member star is 300 – 500. This amount of the stellar data provides relatively well-determined dark matter profile and therefore,

they are especially important when one considers the conservative sensitivity lines. Here, we extract the halo data from Draco and Ursa Minor observations and use it for the input of the mock generator.

The mock dSphs is constructed by two steps. At the first step, we generate the member stars with the color and chemical information by using a stellar evolution model deduced from the current photometric and spectroscopic data. The next step is to assign to each star the information about the position and velocity consistent with the phase-space distribution function determined by the input dark matter potential.

In the first step, the synthetic color-magnitude diagrams for the Draco and Ursa Minor are generated by utilizing the latest version of the PERSEC isochrones [200]. We first randomly draw initial masses of stars from the Salpeter initial-mass function. Ages and metallicities are also randomly drawn from assumed distributions. The ages of the stars are assumed to be randomly distributed in the range 10^{10} - 10^{12} years for both galaxies. The stellar metallicities ($[\text{Fe}/\text{H}]$) are assumed to follow a Gaussian distribution with a mean and dispersion -1.9 (-2.1) and 0.5 (0.5) dex, respectively, for Draco (Ursa Minor), which approximately reproduce the observed metallicity distributions in these galaxies [201]. The present-day absolute magnitude, temperature and surface gravity are then assigned to each star based on the PERSEC isochrones for the given initial mass, age and metallicity. The apparent magnitudes are obtained by taking into account the distance modulus of 19.40 , which corresponds to the distance of 76 kpc, for both Draco and Ursa Minor [202]. Finally, the photometric errors, which are assumed to increase toward fainter magnitudes with a cubic polynomial, are assigned to the apparent magnitudes. The number of stars in each galaxy is adjusted to yield the total luminosity approximately consistent with the observed luminosity.

After constructing the member star mock, we next randomly assign the position and velocity for each star by using the kinematical distribution of the dSph (and finally add the bulk velocity v_{dSph}). The stellar distribution consistent with the dark matter potential is obtained by the method in Ref. [203] in which we assume the constant velocity anisotropy parameter (see appendix B for detail). As the input dark matter halo, we adopt two types of the halo profile considering ‘Draco like’ and ‘Ursa Minor like’ dSph. For Draco like dSphs, we estimate the halo profile by utilizing the current kinematical stellar data given by MMT/Hectochelle observations [204]. We obtain the best fit parameters of the halo by the same method in Ref. [195]

θ_{ROI} [degree]	i_{max} [mag]	dv [km/s]	$d[\text{Fe}/\text{H}]$	$d \log_{10}(g/[\text{cm}/\text{s}^2])$	dT_{eff} [K]
0.65, 1.3	21, 21.5	3.0	0.5	0.5	500

Table 5: *The capability of the spectrograph.* θ_{ROI} is the radius of the region of interest.

as shown in the first line of Table 4 (‘Draco 1’).^{#33} However, the best fit data for Draco usually gives large r_s (~ 10 kpc). In fact, the amount of the foreground contamination is not obvious for the current observational data. As one can see later, foreground contamination gives a large velocity dispersion at outer region and leads overestimation of the halo size. Therefore, we also adopt another fit parameter with smaller r_s and a good chi-square (0.1% larger than the best fit chi-square) as shown in the second line of Table 4 (‘Draco 2’). For Ursa Minor like dSphs, on the other hand, because the kinematical data of the Ursa Minor is not available, we adopt the median values of Ref[195] as the input parameter of the halo which is shown in the third line of Table 4 (‘Ursa Minor’).

The non-member stars belonging to the Milky Way galaxy are also included in the mock data. This foreground stars are generated from the Besançon model [205]. The generator provides the stellar population of the Milky Way galaxy including the thin disc, thick disc, bulge and halo component with its velocity, age, luminosity, color, chemical components, effective temperature and surface gravity. As the Besançon model only provides the distance from the earth to each star, we assign the projected spatial coordinate assuming that the distribution is isotropic in the region of interest.

7.2.3 Spectrograph

As the future spectrograph, we model the Prime Focus Spectrograph (PFS), which is introduced in Sec 6.6. The PFS is the next future spectrograph of the SuMiRe project [190], which has large region of interest (~ 0.65) and 2394 fibers. The spectrograph has the three-color-arms which cover blue, red and near infrared wavelength with the resolution $\lambda/\delta\lambda$ of 2500, 3200, and 4500 respectively. Moreover, the spectrograph has the other median-resolution option for the red-arm ($\lambda/\delta\lambda = 5000$), where the expected velocity resolution dv reaches 3 km/sec.^{#34} In addition, utiliz-

^{#33} The fit uses the ~ 450 kinematical data.

^{#34} The median resolution mode ($\lambda = 7100 - 8850 \text{ \AA}$) covers the Calcium triplet and α element lines.

dSph	θ_{ROI} [degree]	i_{max} [mag]	v_{lower} [km/s]	v_{upper} [km/s]	N_{Mem}	N_{FG}
Draco	0.65	21	−350	−230	900	37
		21.5			1140	43
	1.3	21	940	152		
Ursa Minor	0.65	21	−310	−190	1100	33
		21.5			1400	41
	1.3	21	1130	140		

Table 6: *The status of the mock dSphs. The averaged number of the member (foreground) stars after the cuts are given by N_{Mem} (N_{FG}). See the text for the details of the cuts.*

ing the line spectrum in the wide wavelength, it is expected that the detailed star information can be obtained with good accuracies.

For the region of interest, we assume one pointing observation (a radius of 0.65 degrees) and four pointing observation (1.3 degrees). We also assume that the spectrograph can measure the recession velocity v , metallicity $[\text{Fe}/\text{H}]$, effective temperature T_{eff} , and surface gravity g for each star with the accuracies given in Table 5, which are used to eliminate the foreground stars.^{#35} To convolve the detector resolution, the mock data is smeared by the normal distribution functions with the respective resolution widths given in Table 5. As the depth of the survey depends on the exposure time, we adopt two cases of the upper bound of the magnitude ($i_{\text{max}} = 21, 21.5$). We note that $i_{\text{max}} = 21$ corresponds to a sensitivity of two nights exposure of PFS and the current observation for Draco is $i_{\text{max}} \lesssim 20.5$. $i_{\text{max}} = 21.5$ is considered only for the one-pointing case.

7.2.4 Cut

The mock data obtained in the previous section contains large number of the foreground stars (more than five times larger). To reduce the foreground contamination, we impose the cuts to the raw mock data. First, the spatial ($r < d \sin \theta_{\text{ROI}}$) cut should be imposed because of the limited region of interest. Here d denotes the distance of each dSph and θ_{ROI} is the radius of the region of interest. We further optimize the foreground contamination by imposing following cuts:

^{#35} We check the effect of the velocity resolution and find it small because the dispersion is given by $\sqrt{\sigma_r^2 + dv^2}$. For classical dSph case, $\sigma_r \gtrsim 10$ (km/sec) and the effect of dv is negligible.

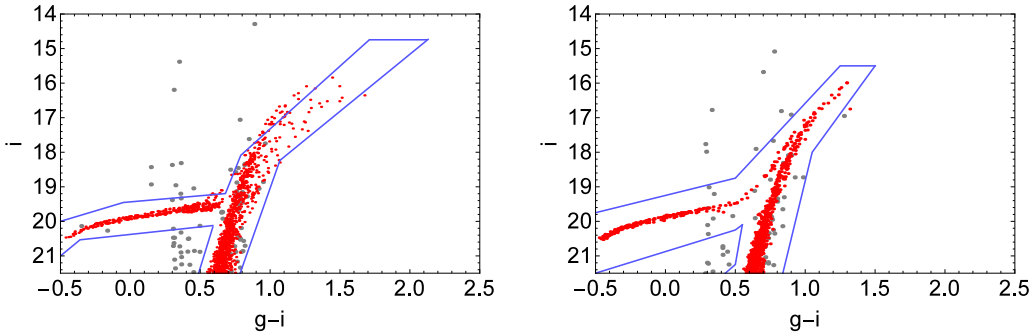


Figure 19: The color-magnitude map for Draco (left) and Ursa Minor (right). We impose the color-magnitude cut by the blue lines. The red dots show the members star and gray dots represent the foreground stars. The stars on the map are residuals after the cuts of the ROI, velocity and $\log g$. For Draco, we draw the color cut referring Ref. [204].

- $v_{\text{lower}} < v < v_{\text{upper}}$,
- $0.2 < \log_{10}(g/[\text{cm/s}^2]) < 3.7$,

as well as the cut on the color-magnitude diagram as shown in Fig.19. Here, v_{lower} , v_{upper} are given in Table 6 for each dSph. The composition after imposing the cuts is also shown in that table. Here we note that because the surface gravity reflects the absolute magnitude, the surface gravity cut can efficiently eliminate the dark foreground stars from the member stars with brighter absolute magnitude. We also note that the most of the residual foreground stars belong to the halo star component and therefore, additional cuts using the chemical component or effective temperature is not efficient because the halo stars have similar origin to the dSph member star. Rather, these additional cuts eliminate the member stars scattered by the detector resolution by 15 % level.

7.2.5 Velocity dispersion

The velocity dispersion along the line-of-sight can be obtained from the equation (50), (51). Here we note that the equation (50) has a general solution [206, 207]. When the β_{ani} is constant, the radial velocity dispersion can be expressed as

$$\sigma_r^2(r) = \frac{1}{\nu_*(r)} \int_r^\infty \nu_*(r') \left(\frac{r'}{r}\right)^{2\beta_{\text{ani}}} \frac{GM(r')}{r'^2} dr' . \quad (54)$$

The detailed derivation is given in appendix A. Combining the equations (51), (52), (53), and (54), we can obtain the theoretical dispersion curve for given halo parameters α , β , γ , ρ_s , r_s and velocity anisotropy β_{ani} . We also note that $M(r) \equiv$

$\int_0^r 4\pi r'^2 \rho(r') dr'$ under the spherical assumption and $\Sigma_*(R) = (1/\pi r_e^2) (1 + (R/r_e)^2)^{-2}$ for the Plummer profile.

7.2.6 Likelihood

The likelihood function is constructed taking the foreground contamination into account. To avoid the binning dependence, we perform the unbinned analysis by setting the likelihood as follows:

$$-2 \ln \mathcal{L} = -2 \sum_i \ln(s f_{\text{Mem}}(v_i, R_i) + (1 - s) f_{\text{FG}}(v_i, R_i)) , \quad (55)$$

where s is the membership fraction parameter and $f_{\text{Mem}}(v, R)$ ($f_{\text{FG}}(v, R)$) is the distribution function of the member (foreground) stars. ‘ i ’ runs all the mock data set. The distribution functions are defined by

$$f_{\text{Mem}}(v, R) = 2\pi R \Sigma_*(R) N_{\text{Mem}} \mathcal{G}[v; v_{\text{Mem}}, \sigma_{l.o.s}(R)] , \quad (56)$$

$$f_{\text{FG}}(v, R) = 2\pi R N_{\text{FG}} \mathcal{G}[v; v_{\text{FG}}, \sigma_{\text{FG}}] , \quad (57)$$

where $\mathcal{G}[x; \mu, \sigma]$ represents the normal distribution function of a variable x with a mean of μ and a standard deviation of σ . The parameter v_{Mem} represents the bulk velocity of the dSph while v_{FG} is (dominantly) controlled by the bulk velocity of the foreground halo component. Here, we assume that the both velocity distribution can be approximated by the single Gaussian and σ_{FG} is independent from R . N_{Mem} , N_{FG} , is the normalization correction factor, under which the distribution functions satisfy

$$\int_0^{r_{\text{ROI}}} dR \int_{v_{\text{lower}}}^{v_{\text{upper}}} dv f_{\text{Mem}}(v, R) = 1 , \quad (58)$$

$$\int_0^{r_{\text{ROI}}} dR \int_{v_{\text{lower}}}^{v_{\text{upper}}} dv f_{\text{FG}}(v, R) = 1 , \quad (59)$$

where $r_{\text{ROI}} \equiv d \sin \theta_{\text{ROI}}$. We note that the free parameter v_{Mem} always converges to the input bulk velocity v_{dSph} . We make the width of the velocity cut wide enough compared to $\sigma_{l.o.s}(R)$ around v_{dSph} and thus we can neglect the correction from the velocity integration of the member star distribution.

Before the fit, the information about v_{FG} , σ_{FG} can be extracted by utilizing the data set in the control region, i.e., the data set with $v < v_{\text{lower}}$ or $v > v_{\text{upper}}$.^{#36} Performing a fit to the control region, the best fit value and standard deviation

^{#36} The control region can also be taken by the spatial position, setting an annulus centered at the dSph galaxy. However, we have found that the fraction of the member star in the annulus is not negligible and therefore we decided to use v parameter to define the control region.

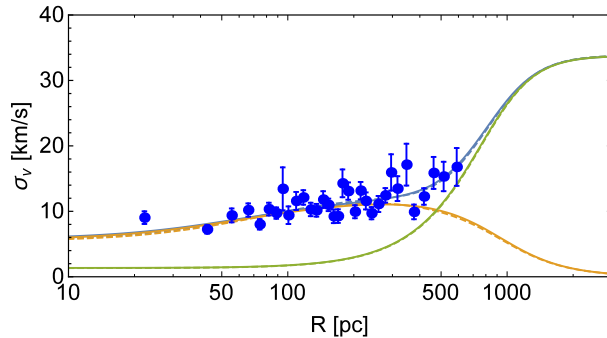


Figure 20: *The dispersion curve of the Ursa Minor Mock ($\theta_{ROI} = 0.65$, $i_{max} = 21$). The solid blue line shows the dispersion curves obtained from the best fit parameter. The binned dispersions of the mock data are shown by the blue dots with error bars. The solid orange (green) line shows the member (foreground) contribution to the dispersion curve. The dashed orange line is obtained from the input parameter of the dSph dark matter halo. The dashed green line is the curve obtained from the mean value of the foreground prior, while the dashed blue line shows the sum of them.*

of v_{FG} , σ_{FG} (v_{FG0} , σ_{FG0} , dv_{FG} , $d\sigma_{FG}$) can be obtained. We use this information as a prior for v_{FG} , σ_{FG} by multiplying $\mathcal{G}[v_{FG}; v_{FG0}, dv_{FG}] \mathcal{G}[\sigma_{FG}; \sigma_{FG0}, d\sigma_{FG}]$ to the likelihood function in equation (55). The detailed way to estimate the foreground distribution function is given in appendix C.

The likelihood (multiplied by the foreground priors) is maximized under the five free parameters of the dark matter halo (ρ_s , r_s , α , β , γ), one velocity anisotropy parameter β_{ani} and four nuisance parameters in the likelihood function (s , v_{Mem} , v_{FG} , σ_{FG}). We perform the Metropolis-Hastings (MH) algorithm [208, 209] of the Markov Chain Monte Carlo (MCMC) method. Once one properly tunes the MCMC process (such as the number of the burn-in step, the sampling step and length of the chain), the sampling set of the MCMC reflects the probability density of the likelihood function. Accumulating $\mathcal{O}(10^5)$ samples for each data set, we search the halo parameters under the flat/log-flat priors within the range of $-4 < \log_{10}(\rho_s/[M_{\odot}/\text{pc}^3]) < 4$, $0 < \log_{10}(r_s/[\text{kpc}]) < 5$, $0.5 < \alpha < 3$, $3 < \beta < 10$, $0 < \gamma < 1.2$ and $-1 < \log_{10}(1 - \beta_{ani}) < 1$, which is the same criteria of [195].

7.3 Results

Table 7 shows the results of the fit. We make 10 mocks for each case and average the median values of $\log J$. The error bar of the J -factor for each mock sample is estimated by comparing the median and 68% quantile. In the table, we give the

Mock	θ_{ROI}	i_{max}	Ref	Contaminated	Our fit	Ultimate
Draco 1	0.65	21	18.94	19.32 ^{+0.10} _{-0.11} ± 0.10	18.69 ^{+0.11} _{-0.09} ± 0.07	18.86 ^{+0.09} _{-0.08} ± 0.08
		21.5		19.34 ^{+0.09} _{-0.11} ± 0.05	18.68 ^{+0.09} _{-0.08} ± 0.07	18.87 ^{+0.08} _{-0.07} ± 0.06
		1.3	21		19.40 ^{+0.06} _{-0.06} ± 0.05	18.72 ^{+0.10} _{-0.08} ± 0.08
Draco 2	0.65	21	18.88	19.37 ^{+0.10} _{-0.11} ± 0.09	18.87 ^{+0.12} _{-0.10} ± 0.09	18.88 ^{+0.09} _{-0.07} ± 0.08
		21.5		19.32 ^{+0.09} _{-0.11} ± 0.12	18.88 ^{+0.11} _{-0.10} ± 0.09	18.87 ^{+0.08} _{-0.07} ± 0.09
		1.3	21		19.47 ^{+0.06} _{-0.06} ± 0.04	18.89 ^{+0.10} _{-0.09} ± 0.10
Ursa Minor	0.65	21	19.03	19.30 ^{+0.07} _{-0.06} ± 0.09	19.11 ^{+0.12} _{-0.08} ± 0.04	19.09 ^{+0.13} _{-0.08} ± 0.03
		21.5		19.28 ^{+0.06} _{-0.05} ± 0.05	19.11 ^{+0.11} _{-0.07} ± 0.04	19.08 ^{+0.10} _{-0.07} ± 0.04
		1.3	21		19.47 ^{+0.05} _{-0.05} ± 0.04	19.09 ^{+0.12} _{-0.08} ± 0.04

Table 7: *The resultant J-factors. We make 10 mocks and we give the mean (the first values) and averages of the error bars (the first uncertainties). The standard deviation of the median values is also put on the second uncertainty. The J-factors calculated by the input parameters are given in the ‘Ref’ column. The ‘Contaminated’ column shows the results where all the data after the cut is considered as the member. The ‘Our fit’ column shows the fit results obtained by using the likelihood of equation (55). We also estimate the J-factor without considering the foreground contamination, which is shown in the ‘Ultimate’ column on the table.*

averages of the error bars at the first uncertainties. The standard deviation of the median values is also put on the second uncertainty. The fluctuation of the median values reflects the statistical deviation of the sample quality. As an example of the result, we show the dispersion curve obtained from the best fit parameter and mock data in Fig 20. Although we do not adopt the binned analysis, the fit successfully reproduces the input curves.

All J-factors are calculated in $\Delta\Omega = 2.4 \times 10^{-4}$ sr, corresponding to the angular radius of 0.5 degree, which is the standard size for the J-factor calculation as discussed in Sec. 6.2. To eliminate the fluctuation due to the halo truncation, we fix the size of the halo truncation at 2000 pc for all mocks. ^{#37} The J-factors calculated by the input parameters are given in the ‘Ref’ column. The ‘Contaminated’ column shows the results where all the data after the cut is considered as the member (implying

^{#37} We set slightly larger truncation radii than those given by Ref. [195] (1.9 kpc for Draco and 1.6 kpc for Ursa Minor).

that we fix $s = 1$ in equation (55)). The ‘*Our fit*’ column shows the fit results obtained by using the likelihood of equation (55). As the ultimate case, we also estimate the J-factor without considering the foreground contamination, which is shown in the ‘*Ultimate*’ column on the table.

The ‘*Contaminated*’ column shows that even if the contamination is $\sim 3 - 10$ percent (see table 6) and the number of the observed stars is large, the fit gives systematically large J-factor ($\delta \log J \sim 0.3 - 0.5$). This systematic error stems from the enhancement of the velocity dispersion by the foreground stars at the outer region as can be seen in Fig. 20.

On the other hand, our likelihood estimation gives consistent result compared to the ‘*Ref*’ values (or the ‘*Ultimate*’ case) though small systematical deviation appears. This systematical bias becomes large when r_s is large (Draco 1), which can be explained as follows: Generally speaking, a large r_s gives large member velocity dispersion at the outer region. Consider the velocity distribution at the outer region $R \sim 1$ kpc, where the number of the foreground stars is comparable to the member stars. In the velocity region of interest ($v_{\text{lower}} < v < v_{\text{upper}}$), the foreground velocity distribution monotonically increases as the velocity increases while the member star distribution has Gaussian peak at $v = v_{\text{dSph}}$ with a standard deviation of $\sigma_{l.o.s}(R)$. Therefore, more miss-identification occur in the $v > v_{\text{dSph}}$ region, where the fit considers the foreground as the member star and *vice versa*. Furthermore, when the member dispersion is large, it becomes hard to distinguish the foreground dispersion curve and the miss-identification occurs even at around the Gaussian peak $v \sim v_{\text{dSph}}$ while $v < v_{\text{dSph}}$ region gives relatively correct identification. This asymmetric uncertainty leads the underestimation of the width of the member velocity distribution. We note that this miss-identification occurs within the uncertainty of the foreground distribution shape and therefore the wide region of interest ameliorates the fit result even for Draco 1 case. This fact implies that one should be aware of the systematical errors when the resultant r_s is, roughly speaking, larger than the maximum distance of the observed stars.

We finally show the effect on the sensitivity line using the Fermi-LAT gamma-ray telescope. Fig. 21 shows the expected median sensitivity line by the Fermi-LAT 6 years observation computed by the same method in Sec. 6. The blue line uses the J-factor obtained from our likelihood, while the red line uses the contaminated fit result of Draco 2 mock with $\theta_{\text{ROI}} = 0.65$, $i_{\text{max}} = 21$. The dashed line is from the input value setting $\delta \log J = 0.16$ (the same size as in Ref. [63]). ‘Pass 7’ capabilities are used for the estimation. The figure shows that the overestimation of the J-factor

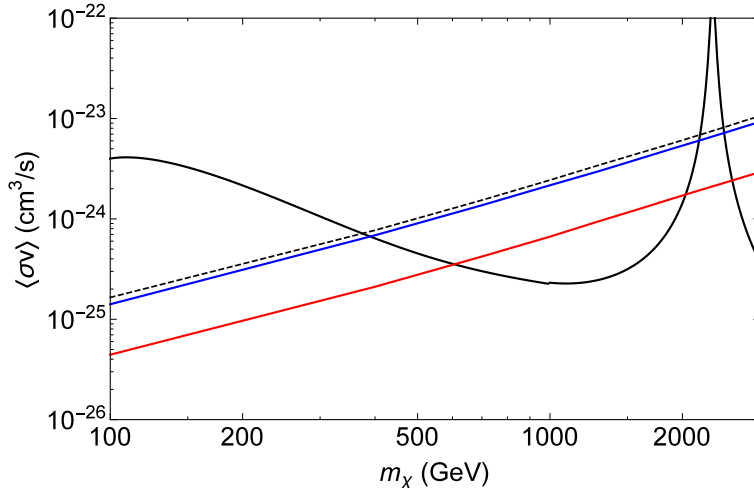


Figure 21: *The expected median sensitivity lines by the Fermi-LAT 6 years observation. The blue line uses the J -factor obtained from our likelihood, while the red line uses the contaminated fit result of Draco 2 mock with $\theta_{ROI} = 0.65$, $i_{max} = 21$. The dashed line is from the input value setting $\delta \log J = 0.16$ (the same size as in Ref. [63]). ‘Pass 7’ capabilities are used for the estimation.*

derives factors of three deviation of the sensitivity lines, implying the importance of the foreground reduction.

7.4 Conclusion

In this section, we have investigated the effect of the foreground contamination by using the mock dSph samples. We have tested the various cuts to optimize the quality of the data and found that the cut using the velocity and surface gravity efficiently eliminate the contamination, while the other cuts do not work well because the origin of the member stars and foreground halo stars are degenerated. A new likelihood function has been constructed which includes the foreground distribution function. We have tested the likelihood function by making the three types of the mock data (Ursa Minor, Draco with large r_s and Draco with small r_s) and three cases of the observation (small/large ROI, $i_{max} = 21, 21.5$). The likelihood successfully reproduces the reference J -factor value while the contaminated fit gives large deviation from the reference value. The effect of the sampling fluctuation has also been estimated and found that it leads $\delta \log J \sim 0.1$ deviation at most even for the fit under $\mathcal{O}(1000)$ samples. We have also found that the reduction of the foreground effect becomes worse when the halo radius is large (roughly larger than

the outer most observed star), which causes $\delta \log J \sim 0.2$ deviation. This deviation is mitigated by the understanding of the foreground function, i.e. by taking a wide control region.

8 Summary

In this thesis, we have comprehensively studied the future detection of the wino dark matter. Detection of the wino dark matter has a strong impact on particle physics, because the high scale SUSY breaking models, which is now regarded as one of the most promising new physics candidates, predicts the neutral wino as dark matter in most of their parameter region. Although the wino can be detected by both the collider searches and indirect detections, it is not easy to reach the $\mathcal{O}(1)$ TeV wino sensitivity. To test the future detectability of wino, we investigate the collider search and indirect detections. For collider search, one of the most promising searches will be brought by the linear colliders. However, although the linear collider sensitivity is quite strong for the relatively light dark matter below the center of mass energy, the sensitivity reach for the heavier wino dark matter has been unclear. In Sec. 4.3, we have provided a precise estimation for the indirect search where the loop contribution of the dark matter is probed through the standard model channels. The likelihood analysis including the realistic systematic errors reveals that 500 GeV beam energy can probe up to 650 – 750 GeV wino through the channel of the SM fermion pair production.

The indirect detection, especially the gamma-ray observation of the dSphs observation is also a strong probe to the $\mathcal{O}(1)$ TeV wino. However, the uncertainties hidden in the halo estimation should be carefully taken into account, especially when the ultra-faint dSph observation is considered. In Sec. 6, we have investigated the future sensitivity reach of the dSph detection. For realistic and conservative estimation, we have robustly discussed the dark matter density profile inside each dSph, astrophysical backgrounds against the wino dark matter detection, and the capability of present and future gamma-ray telescopes. We have found that the limit will be expanded to $810 \text{ GeV} \leq m_{\tilde{w}} \leq 1.86 \text{ TeV}$ and $2.7 \text{ TeV} \leq m_{\tilde{w}} \leq 2.9 \text{ TeV}$ using ten years data of the Fermi-LAT when the J -factors of ultra-faint dSphs are determined with its accuracy of $\delta(\log_{10} J_{\text{UF}}) = 0.2$. The sensitivity will reach 1.0 TeV and more if we include the future telescope. In addition, we have also pointed out that the precise J -factors estimation for both classical and ultra-faint dSphs significantly affects the sensitivity lines, by which we can exclude the entire wino parameter region.

Finally, we have tested the future J -factors determination performing a precise halo estimation under the future kinematical survey. The estimation has many systematic errors such as the prior biases, halo truncation, non-sphericity, anisotropy and, foreground contamination. The study has especially focused on the treatment of the foreground contamination, which plays a crucial role for the future observation. Under the realistic setup of the future spectrograph and the optimization of the cut, we have found that the number of the observed star can be more than twice compared to the current observation, including less than 5% contamination. However, we have also found that this contamination significantly biases the J -factor median value, which leads factors of three deviation. We have proposed a new likelihood function and shown that the contamination is efficiently eliminated under the new method.

Acknowledgments

I would like to express my deepest gratitude to my supervisor, Professor Shigeki Matsumoto for his continuous support, encouragement and discussion during my doctoral course. Without his help, I would never complete my dissertation. I am also deeply grateful to my official supervisor, Professor Kentro Hori for providing me a great support and opportunity as a Ph.D. student in his laboratory. I would like to show my great appreciation to Biplob Bhattacharjee, Takeshi Fukuyama, Keisuke Harigaya, Kohei Hayashi, Masahiro Ibe, Miho Ishigaki, Kunio Kaneta, Anirban Kundu, Yukihiro Mimura, Kohei Nishiyama, Satoshi Shirai, Hajime Sugai, for their collaboration and fruitful discussions. I would also like to thank Tomoki Ohtsuki who shares the office room with me and always gives me warm encouragements. I would also like to thank my family, who always support and encourage me with their best wishes. Finally, I would like to thank JSPS Research Fellowships for Young Scientists which made me possible to complete this study.

Appendix A Jeans equation

A.1 Boltzmann equation

In this appendix, we derive the Jeans equation (50).

Jeans equation can be derived from Boltzmann equation by using spherical and steady-state assumptions. Consider phase-space (p, q, t) and an infinitesimal volume $\delta p \delta q$ on the phase-space at time t . Here, p, q is canonical momentum and coordinate respectively. We define phase distribution function $f(p, q, t)$ which represents number density of particle in the infinitesimal volume $\delta p \delta q$. Boltzmann equation gives time evolution of the distribution function $f(p, q, t)$ in $\delta p \delta q$. Position and momentum of particles in $\delta p \delta q$ evolves as $(p, q, t) \rightarrow (p', q', t')$ obeying an equation of motion characterized by a Hamiltonian $H(p, q)$. Number of the particles in $\delta p \delta q$ is invariant under an infinitesimal time evolution as long as we see the same phase-space volume propagated by the equation of motion: $\delta p \delta q \rightarrow \delta p' \delta q'$, which implies,

$$f(p, q, t) \delta p \delta q = f(p', q', t') \delta p' \delta q' . \quad (60)$$

Under a collisionless system, Liouville theorem provides $\delta p \delta q = \delta p' \delta q'$ and we can obtain general (collisionless) Boltzmann equation.

$$f(p', q', t') - f(p, q, t) = \left(\dot{p} \frac{\partial f}{\partial p} + \dot{q} \frac{\partial f}{\partial q} + \frac{\partial f}{\partial t} \right) \delta t = 0 . \quad (61)$$

Practically, it is often expressed by position-velocity variables (\vec{x}, \vec{v}) and we will adopt this expression in the following discussion: $\partial f / \partial t + \dot{\mathbf{x}} \partial f / \partial \mathbf{x} + \dot{\mathbf{v}} \partial f / \partial \mathbf{v} = 0$.

Using the Boltzmann equation, we can construct relations among following observables:

$$\nu(\vec{x}) \equiv \int f(\vec{x}, \vec{v}) d\vec{v}, \quad (62)$$

$$\overline{u_i}(\vec{x}) \equiv \frac{1}{\nu(\vec{x})} \int v_i f(\vec{x}, \vec{v}) d\vec{v}, \quad (63)$$

$$\overline{u_i^2}(\vec{x}) \equiv \frac{1}{\nu(\vec{x})} \int (v_i - \overline{u_i})^2 f(\vec{x}, \vec{v}) d\vec{v}, \quad (64)$$

$$\overline{u_{ij}^2}(\vec{x}) \equiv \frac{1}{\nu(\vec{x})} \int (v_i - \overline{u_i})(v_j - \overline{u_j}) f(\vec{x}, \vec{v}) d\vec{v} \quad (\text{for } i \neq j), \quad (65)$$

where $\nu(\vec{x})$ represents number density. $\overline{u_i}(\vec{x})$ is mean velocity along a direction i and $\overline{u_i^2}(\vec{x}), \overline{u_{ij}^2}(\vec{x})$ is velocity dispersion for each combination (i, j) .

For stellar kinematics, it is convenient to express Boltzmann equation on spherical coordinate of (r, θ, ϕ) . As a preparation for the spherical expression, we introduce Hamiltonian $H = K(p) + T(q)$ where $K(p) = m_0 v^2/2$ implies kinematical energy of stars in the infinitesimal volume $\delta p \delta q$ and potential energy $T(q) = m_0 V(q)$ is defined by potential $V(q)$. Here m_0 represents total enclosed mass in the volume. This Hamiltonian on spherical coordinate can be expressed by canonical variables $(r, \theta, \phi, p_r, p_\theta, p_\phi)$ as follows:

$$H = \frac{p_r^2}{2m_0} + \frac{p_\theta^2}{2m_0 r^2} + \frac{p_\phi^2}{2m_0 r^2 \sin^2 \theta} + m_0 V(r, \theta, \phi) . \quad (66)$$

It is convenient to express these momentums by velocity (v_r, v_θ, v_ϕ) as $p_r = m_0 v_r$, $p_\theta = m_0 r v_\theta$, $p_\phi = m_0 r \sin \theta v_\phi$. Then equation of motion provides following equations:

$$\begin{aligned} \dot{v}_r &= \frac{v_\theta^2 + v_\phi^2}{r} - \frac{\partial V}{\partial r} , \\ \dot{v}_\theta &= \frac{v_\phi^2 \cot \theta - v_r v_\theta}{r} - \frac{1}{r} \frac{\partial V}{\partial \theta} , \\ \dot{v}_\phi &= -\frac{v_\phi (v_r + v_\theta \cot \theta)}{r} - \frac{1}{r \sin \theta} \frac{\partial V}{\partial \phi} , \end{aligned} \quad (67)$$

The continuity equation can be obtained by acting $\int d\mathbf{v}$ to the Boltzmann equation $\partial f / \partial t + \dot{\mathbf{x}} \partial f / \partial \mathbf{x} + \dot{\mathbf{v}} \partial f / \partial \mathbf{v} = 0$.

$$\begin{aligned} \frac{\partial \nu(\vec{x})}{\partial t} + \frac{\partial}{\partial r} (\nu(\vec{x}) \bar{u}_r(\vec{x})) + \frac{1}{r} \frac{\partial}{\partial \theta} (\nu(\vec{x}) \bar{u}_\theta(\vec{x})) + \frac{1}{r \sin \theta} \frac{\partial}{\partial \phi} (\nu(\vec{x}) \bar{u}_\phi(\vec{x})) \\ + \frac{2\nu(\vec{x}) \bar{u}_r(\vec{x})}{r} + \frac{\nu(\vec{x}) \bar{u}_\theta(\vec{x}) \cot \theta}{r} = 0 . \end{aligned} \quad (68)$$

The second raw of Eq.(68) appears from $\int \dot{\mathbf{v}} \partial f / \partial \mathbf{v}$. Similarly, the dispersion relation can be obtained by acting $\int v_i d\mathbf{v}$ where $i = r, \theta, \phi$. We will only calculate case of $i = r$ which is used later to derive Jeans equation. Using the continuity equation, we can derive the first moment of the Boltzmann equation on spherical coordinate below:

$$\begin{aligned} \nu \frac{\partial}{\partial t} \bar{u}_r + \nu \left(\bar{u}_r \frac{\partial}{\partial r} \bar{u}_r + \frac{\bar{u}_\theta}{r} \frac{\partial}{\partial \theta} \bar{u}_r + \frac{\bar{u}_\phi}{r \sin \theta} \frac{\partial}{\partial \phi} \nu \bar{u}_r \right) \\ + \frac{\partial}{\partial r} (\nu \bar{u}_r^2) + \frac{1}{r} \frac{\partial}{\partial \theta} (\nu \bar{u}_{r\theta}^2) + \frac{1}{r \sin \theta} \frac{\partial}{\partial \phi} (\nu \bar{u}_{r\phi}^2) \\ + \frac{\nu}{r} \left(2\bar{u}_r^2 - \bar{u}_\theta^2 - \bar{u}_\phi^2 + \bar{u}_{r\theta}^2 \cot \theta - (\bar{u}_\theta)^2 - (\bar{u}_\phi)^2 \right) = -\nu \frac{\partial V}{\partial r} . \end{aligned} \quad (69)$$

Next, we will introduce following assumptions for the system:

- Steady-state: $\partial / \partial t = 0$ and $\bar{u}_r = 0$

- Spherical symmetry: $\overline{u_r} = \overline{u_\theta} = \overline{u_\phi}$, $\overline{u_\theta^2} = \overline{u_\phi^2}$ and $\overline{u_{r\theta}^2} = \overline{u_{r\phi}^2} = \overline{u_{\theta\phi}^2} = 0$

Note that we consider an inertial frame of reference such that the system (a galaxy of interest) remains stationary and therefore steady-state implies $\overline{u_r} = 0$. Substituting these conditions into Eq.(69), we finally obtain a simple form of the spherical Boltzmann equation which is often called Jeans equation:

$$\frac{1}{\nu} \frac{\partial}{\partial r} (\nu \overline{u_r^2}) + \frac{2\beta_{\text{ani}}(r) \overline{u_r^2}}{r} = -\frac{\partial V}{\partial r}. \quad (70)$$

Here we introduce anisotropy parameter $\beta_{\text{ani}}(r) \equiv 1 - (\overline{u_\theta^2} + \overline{u_\phi^2})/2\overline{u_r^2}$.

A.2 Projection

Current observation can only measure the quantities along the line of sight (LOS). Once we fix the direction of LOS, tangent vector \vec{r}_\perp can be defined by the shortest distance between the center of the galaxy and LOS. Using the unit vector along the line of sight $\vec{\hat{s}}$, position vector can be decompose of two parts.

$$\vec{r}_\parallel \equiv (\vec{\hat{s}} \cdot \vec{r}) \vec{\hat{s}} \equiv t \vec{\hat{s}}, \quad (71)$$

$$\vec{r}_\perp = \vec{r} - \vec{r}_\parallel. \quad (72)$$

Then number density distribution projected along LOS can be defined by

$$\Sigma(\vec{r}_\perp) = \int_{\text{obs}}^{\infty} dt \int d\vec{v} f(\vec{r}_\perp + t\vec{\hat{s}}, \vec{v}). \quad (73)$$

obs represents the location of the observer. Below, we consider this location is far enough from the galaxy ($\text{obs} \sim -\infty$). t can be expressed by r as $t = \sqrt{r^2 - r_\perp^2}$ which implies $dt = r dr / \sqrt{r^2 - r_\perp^2}$. Using the spherical symmetry $\nu(\vec{r}) = \nu(r)$ and $|\vec{r}_\perp \pm t\vec{\hat{s}}|^2 = r^2$, equation (73) becomes

$$\Sigma(\vec{r}_\perp) = 2 \int_{r_\perp}^{\infty} \frac{\nu(r)r}{\sqrt{r^2 - r_\perp^2}} dr. \quad (74)$$

Similarly, the mean velocity and velocity dispersion along LOS can be defined by using the projection vector $\vec{v}_\parallel \equiv (\vec{\hat{s}} \cdot \vec{v}) \vec{\hat{s}}$.

$$\overline{u_\parallel}(\vec{r}_\perp) = \frac{1}{\Sigma(\vec{r}_\perp)} \int_{\text{obs}}^{\infty} dt \int d\vec{v} (\vec{\hat{s}} \cdot \vec{v}) f(\vec{r}_\perp + t\vec{\hat{s}}, \vec{v}), \quad (75)$$

$$\overline{u_\parallel^2}(\vec{r}_\perp) = \frac{1}{\Sigma(\vec{r}_\perp)} \int_{\text{obs}}^{\infty} dt \int d\vec{v} (\vec{\hat{s}} \cdot \vec{v})^2 f(\vec{r}_\perp + t\vec{\hat{s}}, \vec{v}). \quad (76)$$

The mean velocity is eventually found to be 0 under the spherical symmetry and kinematical equilibrium assumption ($\bar{u}_i = 0$). The velocity dispersion, on the other hand, can be rewritten as

$$\bar{u}_{\parallel}^2(\vec{r}_{\perp}) = \frac{1}{\Sigma(\vec{r}_{\perp})} \int_{obs}^{\infty} dt \hat{s}_i \hat{s}_j \nu(\vec{r}_{\perp} + t\vec{\hat{s}}) \bar{u}_{ij}^2(\vec{r}_{\perp} + t\vec{\hat{s}}). \quad (77)$$

Spherical symmetry implies $\bar{u}_{ij}^2 = 0$ ($i \neq j$) and $\bar{u}_{\theta}^2 = \bar{u}_{\phi}^2$, which gives $\hat{s}_i \hat{s}_j \bar{u}_{ij}^2 = \hat{s}_r^2 \bar{u}_r^2 + (1 - \hat{s}_r^2) \bar{u}_{\theta}^2$. Therefore, using the anisotropy parameter and substituting $\hat{s}_r^2 = (r^2 - r_{\perp}^2)/r^2$, we finally obtain the formula for the velocity dispersion along the LOS:

$$\bar{u}_{\parallel}^2(\vec{r}_{\perp}) = \frac{2}{\Sigma(\vec{r}_{\perp})} \int_{r_{\perp}}^{\infty} \left(1 - \beta_{ani}(r) \frac{r_{\perp}^2}{r^2}\right) \frac{\nu(r) \bar{u}_{rr}^2(r) r}{\sqrt{r^2 - r_{\perp}^2}} dr. \quad (78)$$

A.3 dSph Case

Under the gravitational potential of the dark matter halo, Eq.(70) can be written as:

$$\frac{1}{\nu_*(r)} \frac{d}{dr} [\nu_*(r) \sigma_r^2(r)] + 2 \frac{\beta_{ani}(r) \sigma_r^2(r)}{r} = - \frac{GM(r)}{r^2}. \quad (79)$$

Here we rewrite \bar{u}_r^2 into σ_r^2 , $\nu(r)$ into $\nu_*(r)$. Eq.(79) has the general solution

$$\nu_*(r) \sigma_r^2(r) = \frac{1}{f(r)} \int_r^{\infty} f(s) \nu_*(s) \frac{GM(s)}{s^2} ds, \quad (80)$$

where $f(r) = f_1 \exp[\int_{r_1}^r 2\beta_{ani}(s) s^{-1} ds]$. Here f_1 , r_1 are constant values. If we assume β_{ani} is constant, $f(r)$ can be simplified as $f(r) = f_1 (r/r_1)^{2\beta_{ani}}$. Then Eq.(80) can be expressed as

$$\nu_*(r) \sigma_r^2(r) = \frac{1}{r^{2\beta_{ani}}} \int_r^{\infty} s^{2\beta_{ani}} \nu_*(s) \frac{GM(s)}{s^2} ds. \quad (81)$$

The projected dispersion is also obtained from Eq.(78):

$$\sigma_{l.o.s}^2(R) = \frac{2}{\Sigma_*(R)} \int_R^{\infty} \left(1 - \beta_{ani} \frac{R^2}{r^2}\right) \frac{\nu_*(r) \sigma_r^2(r)}{\sqrt{1 - R^2/r^2}} dr, \quad (82)$$

Here the projected dispersion \bar{u}_{\parallel} is rewritten by $\sigma_{l.o.s}$ and the projected distance r_{\perp} by R , and the projected number distribution Σ by Σ_* .

Appendix B Mock data of dSphs

In this appendix, we introduce the construction of the dSph mock used in Sec. 7.2.2. based on the discussion in Ref. [203]. The stellar distribution of the dSph should be

consistent with the input dark matter potential and stellar distribution. The goal of the formulation is to obtain the distribution function $f(r, \vec{v})$ which satisfies the equation (62), (63), (64), (65) for the given stellar number density and dispersion obtained by the Jeans equation. Here, we assume a steady, spherical system. However, it is usually difficult to solve these equations inversely and therefore, the special form of the distribution is assumed. In this analysis, we adopt the form of

$$f(r, \vec{v}) = f_0(Q(r, \vec{v}))L(r, \vec{v})^{\alpha_{\text{ani}}} , \quad (83)$$

where we define $Q \equiv E - L^2/2r_{\text{ani}}^2$. E, L are the relative energy and the angular momentum of star at the phase space (r, v) respectively, which is given by $E = -(v_r^2 + v_\theta^2 + v_\phi^2)/2 - \Phi(r)$, $L = r\sqrt{v_\theta^2 + v_\phi^2}$. We define the gravitational potential $\Delta\Phi(r) = -4\pi G\rho(r)$ (negative sign convention) which satisfies $\Phi(\infty) = 0$. $r_{\text{ani}} (\geq 0)$, $\alpha_{\text{ani}} (> -1)$ are the parameters which determine the r dependence of the velocity anisotropy β_{ani} .

Under the assumption, the distribution function can be obtained by the formula

$$f_0(Q) = \frac{\sin((n - 1/2 - \alpha_{\text{ani}})\pi)}{\pi\lambda(\alpha_{\text{ani}})(\alpha_{\text{ani}} + 1/2)!} \frac{d^{n+1}}{dQ^{n+1}} \int_0^Q \frac{\nu_2(\Phi)}{Q - \Phi} d\Phi . \quad (84)$$

Here $n \equiv [\alpha_{\text{ani}} + 1/2] + 1$ and $[\alpha_{\text{ani}} + 1/2]$ is the largest integer x which satisfies $x \leq \alpha_{\text{ani}} + 1/2$. $(\alpha_{\text{ani}} + 1/2)!$ is 1 for $(-1 < \alpha_{\text{ani}} \leq -1/2)$ and $(\alpha_{\text{ani}} + 1/2)(\alpha_{\text{ani}} - 1/2) \dots (\alpha_{\text{ani}} + 3/2 - n)$ for $\alpha_{\text{ani}} > -1/2$ and $\lambda(\alpha_{\text{ani}}) \equiv 2^{\alpha_{\text{ani}}+3/2}\pi^{3/2}\Gamma(\alpha_{\text{ani}}+1)/\Gamma(\alpha_{\text{ani}}+3/2)$. We also define ν_2 by

$$\nu_2(r) \equiv \frac{(1 + r^2/r_{\text{ani}}^2)^{\alpha_{\text{ani}}+1}}{r^{2\alpha_{\text{ani}}}} \nu_*(r) . \quad (85)$$

The variable Φ in ν_2 implies that $\nu_2(\Phi) = \nu_2(r(\Phi))$, where we assume that the gravitational potential $\Phi = \Phi(r)$ is the monotonic function and is inversely solved by $r = r(\Phi)$.

We can check that the $f(r, \vec{v})$ obtained by the equation (83), (84) reproduces the input stellar distribution and velocity dispersion obtained from the Jeans equation. Furthermore, the velocity anisotropy can be computed and found

$$\beta_{\text{ani}}(r) \equiv 1 - \frac{\sigma_\theta^2(r) + \sigma_\phi^2(r)}{2\sigma_r^2(r)} = \frac{r^2 - \alpha_{\text{ani}}r_{\text{ani}}^2}{r^2 + r_{\text{ani}}^2} . \quad (86)$$

As we assume the constant anisotropy, we set $r_{\text{ani}} \rightarrow \infty$ and $\alpha_{\text{ani}} = -\beta_{\text{ani}}$ for input β_{ani} .

Finally, we note that because we fix the form of the function as equation (83), the input parameter may not be consistent with this functional form. In that case,

the obtained distribution function has a negative value at some Q . In order to avoid this unphysical distribution, we have slightly modified the input stellar distribution form by introducing the small parameter γ_* : $\nu_*(r) \rightarrow (r/r_*)^{-\gamma_*}\nu_*(r)$. In the analysis, we have set $\gamma_* = 0.1$ and confirmed that the fluctuations of the reproduced number distribution and dispersion curves are negligible.

Appendix C Foreground Distribution

In this appendix, we mention the method to obtain the foreground prior discussed in Sec. 7.2.6. The foreground stars are mainly composed of three components: the halo stars, the thick disc component and the thin disc component. To determine the prior, we use v , $\log g$ information of the mock observation data. For the explanation, we categorize the dataset after the color and ROI cut into two types.

1. the dataset with velocity cut.
2. the dataset with velocity & $\log g$ cut.

We note that the velocity cut here implies masking the signal region ($v_{\text{lower}} < v < v_{\text{upper}}$) to obtain the pure foreground samples. The goal is to determine the foreground shape in the dataset 2. In the dataset 2, although the dominant contribution is the halo component, the other components non-negligibly distort the shape of the foreground distribution. Therefore, we fit all components assuming that their velocity distribution can all be described by the Gaussian distribution function. However, because the disc distributions are located at around $\log g \gtrsim 0.4$, the number of the disc components after the $\log g$ cut becomes so small that the fit cannot converge well. Therefore, we first determine the shape of the thick/thin disc component using the data without $\log g$ cut (dataset 1).

In the first fit, we fit the velocity distribution of the dataset 1 by the sum of the three Gaussians allowing all the parameters (normalizations, mean velocities, dispersions) free. As one can see in the Fig. 22, the fit can be successfully performed because the peaks of the three components are obvious. Then, assuming that the distribution of the thick/thin disc component does not change after the $\log g$ cut (except for their normalization), we use these mean velocities and dispersions to the next fit (dataset 2). ^{#38} Here we note that we cannot utilize information of the halo distribution to the next fit because the halo distribution non-negligibly depends on

^{#38}We have checked the $\log g$ dependence on these component and found that it is small.

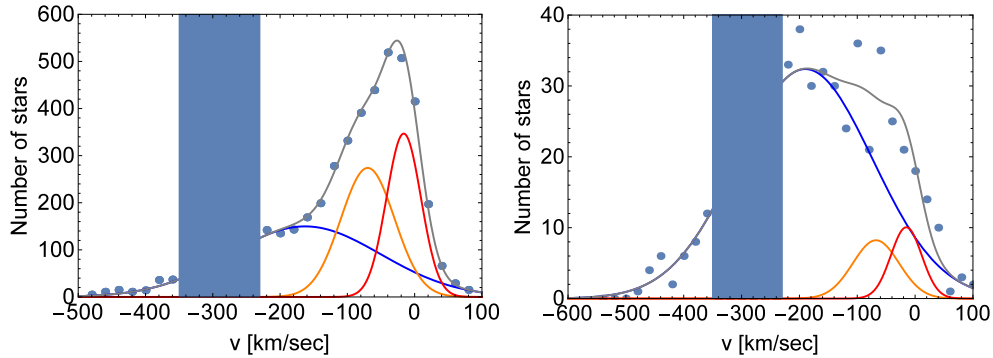


Figure 22: *Foreground fit for the Draco 1 sample with $\theta_{ROI} = 1.3$, $i_{max} = 21$. The blue-shaded region is the signal region. The gray line shows the result of the fit and the blue, orange, red lines show the contribution from the halo, thick disc, and thin disc component respectively. The left panel is the result of the dataset 1 while the right is of the dataset 2. See the text for more detail.*

the $\log g$.^{#39}

In the next step, we again assume that the three components are normal distribution and fit them to the dataset 2 (with velocity and $\log g$ cut). In this fit we constrain the shape of the disc components by imposing the Gaussian prior of the mean velocity and the dispersion, which is obtained from the previous fit. The example of the fit is shown in the right panel of Fig. 22.

We finally note that the foreground curve in the signal region (the blue-shaded region in Fig. 22) is dominated by the halo component and therefore the prior Gaussian for the main fit in Sec. 7.2.6 can be described by the single Gaussian of the halo component.

References

- [1] **ATLAS** Collaboration, G. Aad *et al.*, “Observation of a new particle in the search for the Standard Model Higgs boson with the ATLAS detector at the LHC,” *Phys. Lett.* **B716** (2012) 1–29, [arXiv:1207.7214 \[hep-ex\]](#).
- [2] **CMS** Collaboration, S. Chatrchyan *et al.*, “Observation of a new boson at a mass of 125 GeV with the CMS experiment at the LHC,” *Phys. Lett.* **B716** (2012) 30–61, [arXiv:1207.7235 \[hep-ex\]](#).

^{#39} The shape of the halo component keeps Gaussian in the range of interest, while its mean and width change with respect the $\log g$ value.

- [3] F. Zwicky, “Die Rotverschiebung von extragalaktischen Nebeln,” *Helvetica Physica Acta* **6** (1933) 110–127.
- [4] V. C. Rubin, N. Thonnard, and W. K. Ford, Jr., “Extended rotation curves of high-luminosity spiral galaxies. IV - Systematic dynamical properties, SA through SC,” *Astrophysical Journal* **225** (Nov., 1978) L107–L111.
- [5] V. C. Rubin, W. K. J. Ford, and N. . Thonnard, “Rotational properties of 21 SC galaxies with a large range of luminosities and radii, from NGC 4605 /R = 4kpc/ to UGC 2885 /R = 122 kpc/,” *Astrophysical Journal* **238** (June, 1980) 471–487.
- [6] D. E. McLaughlin, “Evidence in virgo for the universal dark matter halo,” *Astrophys. J.* **512** (1999) L9, [arXiv:astro-ph/9812242](#) [astro-ph].
- [7] E. L. Lokas and G. A. Mamon, “Dark matter distribution in the Coma cluster from galaxy kinematics: Breaking the mass - anisotropy degeneracy,” *Mon. Not. Roy. Astron. Soc.* **343** (2003) 401, [arXiv:astro-ph/0302461](#) [astro-ph].
- [8] D. Clowe, M. Bradac, A. H. Gonzalez, M. Markevitch, S. W. Randall, C. Jones, and D. Zaritsky, “A direct empirical proof of the existence of dark matter,” *Astrophys. J.* **648** (2006) L109–L113, [arXiv:astro-ph/0608407](#) [astro-ph].
- [9] M. Bradac, D. Clowe, A. H. Gonzalez, P. Marshall, W. Forman, C. Jones, M. Markevitch, S. Randall, T. Schrabback, and D. Zaritsky, “Strong and weak lensing united. 3. Measuring the mass distribution of the merging galaxy cluster 1E0657-56,” *Astrophys. J.* **652** (2006) 937–947, [arXiv:astro-ph/0608408](#) [astro-ph].
- [10] **Planck** Collaboration, P. A. R. Ade *et al.*, “Planck 2015 results. XIII. Cosmological parameters,” [arXiv:1502.01589](#) [astro-ph.CO].
- [11] J. Wess and J. Bagger, *Supersymmetry and supergravity*. 1992.
- [12] S. P. Martin, “A Supersymmetry primer,” [arXiv:hep-ph/9709356](#) [hep-ph]. [Adv. Ser. Direct. High Energy Phys.18,1(1998)].
- [13] Y. Okada, M. Yamaguchi, and T. Yanagida, “Upper bound of the lightest Higgs boson mass in the minimal supersymmetric standard model,” *Prog. Theor. Phys.* **85** (1991) 1–6.
- [14] J. R. Ellis, G. Ridolfi, and F. Zwirner, “Radiative corrections to the masses of supersymmetric Higgs bosons,” *Phys. Lett.* **B257** (1991) 83–91.

- [15] H. E. Haber and R. Hempfling, “Can the mass of the lightest Higgs boson of the minimal supersymmetric model be larger than $m(Z)$?,” *Phys. Rev. Lett.* **66** (1991) 1815–1818.
- [16] Y. Okada, M. Yamaguchi, and T. Yanagida, “Renormalization group analysis on the Higgs mass in the softly broken supersymmetric standard model,” *Phys. Lett.* **B262** (1991) 54–58.
- [17] G. Degrandi, S. Di Vita, J. Elias-Miro, J. R. Espinosa, G. F. Giudice, G. Isidori, and A. Strumia, “Higgs mass and vacuum stability in the Standard Model at NNLO,” *JHEP* **08** (2012) 098, [arXiv:1205.6497 \[hep-ph\]](#).
- [18] T. Hahn, S. Heinemeyer, W. Hollik, H. Rzehak, and G. Weiglein, “High-Precision Predictions for the Light CP -Even Higgs Boson Mass of the Minimal Supersymmetric Standard Model,” *Phys. Rev. Lett.* **112** no. 14, (2014) 141801, [arXiv:1312.4937 \[hep-ph\]](#).
- [19] G. F. Giudice, M. A. Luty, H. Murayama, and R. Rattazzi, “Gaugino mass without singlets,” *JHEP* **12** (1998) 027, [arXiv:hep-ph/9810442 \[hep-ph\]](#).
- [20] J. D. Wells, “PeV-scale supersymmetry,” *Phys. Rev.* **D71** (2005) 015013, [arXiv:hep-ph/0411041 \[hep-ph\]](#).
- [21] L. Randall and R. Sundrum, “Out of this world supersymmetry breaking,” *Nucl. Phys.* **B557** (1999) 79–118, [arXiv:hep-th/9810155 \[hep-th\]](#).
- [22] M. Ibe, T. Moroi, and T. T. Yanagida, “Possible Signals of Wino LSP at the Large Hadron Collider,” *Phys. Lett.* **B644** (2007) 355–360, [arXiv:hep-ph/0610277 \[hep-ph\]](#).
- [23] M. Ibe and T. T. Yanagida, “The Lightest Higgs Boson Mass in Pure Gravity Mediation Model,” *Phys. Lett.* **B709** (2012) 374–380, [arXiv:1112.2462 \[hep-ph\]](#).
- [24] M. Ibe, S. Matsumoto, and T. T. Yanagida, “Pure Gravity Mediation,” *Phys. Rev.* **D85** (2012) 095011, [arXiv:1202.2253 \[hep-ph\]](#).
- [25] N. Arkani-Hamed, A. Gupta, D. E. Kaplan, N. Weiner, and T. Zorawski, “Simply Unnatural Supersymmetry,” [arXiv:1212.6971 \[hep-ph\]](#).
- [26] K. Inoue, M. Kawasaki, M. Yamaguchi, and T. Yanagida, “Vanishing squark and slepton masses in a class of supergravity models,” *Phys. Rev.* **D45** (1992) 328–337.

- [27] T. Moroi and L. Randall, “Wino cold dark matter from anomaly mediated SUSY breaking,” *Nucl. Phys.* **B570** (2000) 455–472, [arXiv:hep-ph/9906527](#) [[hep-ph](#)].
- [28] T. Gherghetta, G. F. Giudice, and J. D. Wells, “Phenomenological consequences of supersymmetry with anomaly induced masses,” *Nucl. Phys.* **B559** (1999) 27–47, [arXiv:hep-ph/9904378](#) [[hep-ph](#)].
- [29] J. Hisano, S. Matsumoto, M. Nagai, O. Saito, and M. Senami, “Non-perturbative effect on thermal relic abundance of dark matter,” *Phys. Lett.* **B646** (2007) 34–38, [arXiv:hep-ph/0610249](#) [[hep-ph](#)].
- [30] B. S. Acharya, K. Bobkov, G. L. Kane, P. Kumar, and J. Shao, “Explaining the Electroweak Scale and Stabilizing Moduli in M Theory,” *Phys. Rev.* **D76** (2007) 126010, [arXiv:hep-th/0701034](#) [[hep-th](#)].
- [31] L. J. Hall and Y. Nomura, “Spread Supersymmetry,” *JHEP* **01** (2012) 082, [arXiv:1111.4519](#) [[hep-ph](#)].
- [32] E. Dudas, A. Linde, Y. Mambrini, A. Mustafayev, and K. A. Olive, “Strong moduli stabilization and phenomenology,” *Eur. Phys. J.* **C73** no. 1, (2013) 2268, [arXiv:1209.0499](#) [[hep-ph](#)].
- [33] A. Arvanitaki, N. Craig, S. Dimopoulos, and G. Villadoro, “Mini-Split,” *JHEP* **02** (2013) 126, [arXiv:1210.0555](#) [[hep-ph](#)].
- [34] J. L. Evans, M. Ibe, K. A. Olive, and T. T. Yanagida, “Universality in Pure Gravity Mediation,” *Eur. Phys. J.* **C73** (2013) 2468, [arXiv:1302.5346](#) [[hep-ph](#)].
- [35] J. L. Evans, K. A. Olive, M. Ibe, and T. T. Yanagida, “Non-Universalities in Pure Gravity Mediation,” *Eur. Phys. J.* **C73** no. 10, (2013) 2611, [arXiv:1305.7461](#) [[hep-ph](#)].
- [36] J. L. Evans, M. Ibe, K. A. Olive, and T. T. Yanagida, “One-loop anomaly mediated scalar masses and $(g - 2)_{mu}$ in pure gravity mediation,” *Eur. Phys. J.* **C74** no. 2, (2014) 2775, [arXiv:1312.1984](#) [[hep-ph](#)].
- [37] K. Harigaya, M. Ibe, and T. T. Yanagida, “A Closer Look at Gaugino Masses in Pure Gravity Mediation Model/Minimal Split SUSY Model,” *JHEP* **12** (2013) 016, [arXiv:1310.0643](#) [[hep-ph](#)].
- [38] J. L. Evans, M. A. G. Garcia, and K. A. Olive, “The Moduli and Gravitino (non)-Problems in Models with Strongly Stabilized Moduli,” *JCAP* **1403** (2014) 022, [arXiv:1311.0052](#) [[hep-ph](#)].

- [39] G. D. Coughlan, W. Fischler, E. W. Kolb, S. Raby, and G. G. Ross, “Cosmological Problems for the Polonyi Potential,” *Phys. Lett.* **B131** (1983) 59.
- [40] J. Hisano, T. Moroi, K. Tobe, and M. Yamaguchi, “Lepton flavor violation via right-handed neutrino Yukawa couplings in supersymmetric standard model,” *Phys. Rev.* **D53** (1996) 2442–2459, [arXiv:hep-ph/9510309](#) [hep-ph].
- [41] T. Tsukamoto, K. Fujii, H. Murayama, M. Yamaguchi, and Y. Okada, “Precision study of supersymmetry at future linear $e^+ e^-$ colliders,” *Phys. Rev.* **D51** (1995) 3153–3171.
- [42] B. Bhattacharjee, B. Feldstein, M. Ibe, S. Matsumoto, and T. T. Yanagida, “Pure gravity mediation of supersymmetry breaking at the Large Hadron Collider,” *Phys. Rev.* **D87** no. 1, (2013) 015028, [arXiv:1207.5453](#) [hep-ph].
- [43] J. L. Feng, T. Moroi, L. Randall, M. Strassler, and S.-f. Su, “Discovering supersymmetry at the Tevatron in wino LSP scenarios,” *Phys. Rev. Lett.* **83** (1999) 1731–1734, [arXiv:hep-ph/9904250](#) [hep-ph].
- [44] S. Asai, T. Moroi, and T. T. Yanagida, “Test of Anomaly Mediation at the LHC,” *Phys. Lett.* **B664** (2008) 185–189, [arXiv:0802.3725](#) [hep-ph].
- [45] **ATLAS** Collaboration, G. Aad *et al.*, “Search for charginos nearly mass degenerate with the lightest neutralino based on a disappearing-track signature in pp collisions at $\sqrt{s}=8\text{TeV}$ with the ATLAS detector,” *Phys. Rev.* **D88** no. 11, (2013) 112006, [arXiv:1310.3675](#) [hep-ex].
- [46] **CMS** Collaboration, V. Khachatryan *et al.*, “Search for disappearing tracks in proton-proton collisions at $\sqrt{s} = 8 \text{ TeV}$,” *JHEP* **01** (2015) 096, [arXiv:1411.6006](#) [hep-ex].
- [47] T. Yamanaka *Progress in Particle Physics* (2013) . The reference slide can be found at <http://www2.yukawa.kyoto-u.ac.jp/ppp.ws/PPP2013/program.html>.
- [48] M. Cirelli, F. Sala, and M. Taoso, “Wino-like Minimal Dark Matter and future colliders,” *JHEP* **10** (2014) 033, [arXiv:1407.7058](#) [hep-ph]. [Erratum: *JHEP*01,041(2015)].
- [49] **ILC** Collaboration, G. Aarons *et al.*, “International Linear Collider Reference Design Report Volume 2: Physics at the ILC,” [arXiv:0709.1893](#) [hep-ph].

- [50] **CLIC Physics Working Group** Collaboration, E. Accomando *et al.*, “Physics at the CLIC multi-TeV linear collider,” in *Proceedings, 11th International Conference on Hadron spectroscopy (Hadron 2005)*. 2004. arXiv:hep-ph/0412251 [hep-ph]. <http://weblib.cern.ch/abstract?CERN-2004-005>.
- [51] A. Birkedal, K. Matchev, and M. Perelstein, “Dark matter at colliders: A Model independent approach,” *Phys. Rev.* **D70** (2004) 077701, arXiv:hep-ph/0403004 [hep-ph].
- [52] S. Y. Choi, T. Han, J. Kalinowski, K. Rolbiecki, and X. Wang, “Characterizing invisible electroweak particles through single-photon processes at high energy e^+e^- colliders,” *Phys. Rev.* **D92** no. 9, (2015) 095006, arXiv:1503.08538 [hep-ph].
- [53] J. F. Gunion and S. Mrenna, “Probing models with near degeneracy of the chargino and LSP at a linear e^+e^- collider,” *Phys. Rev.* **D64** (2001) 075002, arXiv:hep-ph/0103167 [hep-ph].
- [54] K. Harigaya, K. Ichikawa, A. Kundu, S. Matsumoto, and S. Shirai, “Indirect Probe of Electroweak-Interacting Particles at Future Lepton Colliders,” *JHEP* **09** (2015) 105, arXiv:1504.03402 [hep-ph].
- [55] “Future circular collider study kickoff meeting.” Geneva, Feb. 12-14, 2014.
- [56] J. Tang *et al.*, “Concept for a Future Super Proton-Proton Collider,” arXiv:1507.03224 [physics.acc-ph].
- [57] J. Hisano, K. Ishiwata, and N. Nagata, “A complete calculation for direct detection of Wino dark matter,” *Phys. Lett.* **B690** (2010) 311–315, arXiv:1004.4090 [hep-ph].
- [58] J. Hisano, K. Ishiwata, and N. Nagata, “Gluon contribution to the dark matter direct detection,” *Phys. Rev.* **D82** (2010) 115007, arXiv:1007.2601 [hep-ph].
- [59] J. Hisano, K. Ishiwata, N. Nagata, and T. Takesako, “Direct Detection of Electroweak-Interacting Dark Matter,” *JHEP* **07** (2011) 005, arXiv:1104.0228 [hep-ph].
- [60] J. Hisano, K. Ishiwata, and N. Nagata, “Direct Search of Dark Matter in High-Scale Supersymmetry,” *Phys. Rev.* **D87** (2013) 035020, arXiv:1210.5985 [hep-ph].

- [61] J. Hisano, K. Ishiwata, and N. Nagata, “QCD Effects on Direct Detection of Wino Dark Matter,” *JHEP* **06** (2015) 097, arXiv:1504.00915 [hep-ph].
- [62] J. Hisano, S. Matsumoto, and M. M. Nojiri, “Explosive dark matter annihilation,” *Phys. Rev. Lett.* **92** (2004) 031303, arXiv:hep-ph/0307216 [hep-ph].
- [63] **Fermi-LAT** Collaboration, M. Ackermann *et al.*, “Searching for Dark Matter Annihilation from Milky Way Dwarf Spheroidal Galaxies with Six Years of Fermi-LAT Data,” *Phys. Rev. Lett.* **115** no. 23, (2015) 231301, arXiv:1503.02641 [astro-ph.HE].
- [64] B. Bhattacharjee, M. Ibe, K. Ichikawa, S. Matsumoto, and K. Nishiyama, “Wino Dark Matter and Future dSph Observations,” *JHEP* **07** (2014) 080, arXiv:1405.4914 [hep-ph].
- [65] **ATLAS** Collaboration, G. Aad *et al.*, “Evidence for the spin-0 nature of the Higgs boson using ATLAS data,” *Phys. Lett.* **B726** (2013) 120–144, arXiv:1307.1432 [hep-ex].
- [66] **CMS** Collaboration, V. Khachatryan *et al.*, “Constraints on the spin-parity and anomalous HVV couplings of the Higgs boson in proton collisions at 7 and 8 TeV,” *Phys. Rev.* **D92** no. 1, (2015) 012004, arXiv:1411.3441 [hep-ex].
- [67] **ATLAS** Collaboration, G. Aad *et al.*, “Measurements of Higgs boson production and couplings in diboson final states with the ATLAS detector at the LHC,” *Phys. Lett.* **B726** (2013) 88–119, arXiv:1307.1427 [hep-ex]. [Erratum: *Phys. Lett.*B734,406(2014)].
- [68] **CMS** Collaboration, V. Khachatryan *et al.*, “Precise determination of the mass of the Higgs boson and tests of compatibility of its couplings with the standard model predictions using proton collisions at 7 and 8 TeV,” *Eur. Phys. J.* **C75** no. 5, (2015) 212, arXiv:1412.8662 [hep-ex].
- [69] M. Ibe, A. Kamada, and S. Matsumoto, “Mixed (cold+warm) dark matter in the bino-wino coannihilation scenario,” *Phys. Rev.* **D89** no. 12, (2014) 123506, arXiv:1311.2162 [hep-ph].
- [70] K. Harigaya, K. Kaneta, and S. Matsumoto, “Gaugino coannihilations,” *Phys. Rev.* **D89** no. 11, (2014) 115021, arXiv:1403.0715 [hep-ph].
- [71] N. Nagata, H. Otono, and S. Shirai, “Probing Bino-Wino Coannihilation at the LHC,” *JHEP* **10** (2015) 086, arXiv:1506.08206 [hep-ph].

- [72] M. Ibe, S. Matsumoto, and R. Sato, “Mass Splitting between Charged and Neutral Winos at Two-Loop Level,” *Phys. Lett.* **B721** (2013) 252–260, [arXiv:1212.5989 \[hep-ph\]](#).
- [73] C. H. Chen, M. Drees, and J. F. Gunion, “A Nonstandard string / SUSY scenario and its phenomenological implications,” *Phys. Rev.* **D55** (1997) 330–347, [arXiv:hep-ph/9607421 \[hep-ph\]](#). [Erratum: *Phys. Rev.* **D60**,039901(1999)].
- [74] A. Hryczuk and R. Iengo, “The one-loop and Sommerfeld electroweak corrections to the Wino dark matter annihilation,” *JHEP* **01** (2012) 163, [arXiv:1111.2916 \[hep-ph\]](#). [Erratum: *JHEP* **06**,137(2012)].
- [75] G. Ovanessian, T. R. Slatyer, and I. W. Stewart, “Heavy Dark Matter Annihilation from Effective Field Theory,” *Phys. Rev. Lett.* **114** no. 21, (2015) 211302, [arXiv:1409.8294 \[hep-ph\]](#).
- [76] T. Sjostrand, S. Mrenna, and P. Z. Skands, “A Brief Introduction to PYTHIA 8.1,” *Comput. Phys. Commun.* **178** (2008) 852–867, [arXiv:0710.3820 \[hep-ph\]](#).
- [77] G. Corcella, I. G. Knowles, G. Marchesini, S. Moretti, K. Odagiri, P. Richardson, M. H. Seymour, and B. R. Webber, “HERWIG 6: An Event generator for hadron emission reactions with interfering gluons (including supersymmetric processes),” *JHEP* **01** (2001) 010, [arXiv:hep-ph/0011363 \[hep-ph\]](#).
- [78] P. Ciafaloni, D. Comelli, A. Riotto, F. Sala, A. Strumia, and A. Urbano, “Weak Corrections are Relevant for Dark Matter Indirect Detection,” *JCAP* **1103** (2011) 019, [arXiv:1009.0224 \[hep-ph\]](#).
- [79] M. Cirelli, G. Corcella, A. Hektor, G. Hutsi, M. Kadastik, P. Panci, M. Raidal, F. Sala, and A. Strumia, “PPPC 4 DM ID: A Poor Particle Physicist Cookbook for Dark Matter Indirect Detection,” *JCAP* **1103** (2011) 051, [arXiv:1012.4515 \[hep-ph\]](#). [Erratum: *JCAP* **1210**,E01(2012)].
- [80] M. Drees and M. Nojiri, “Neutralino - nucleon scattering revisited,” *Phys. Rev.* **D48** (1993) 3483–3501, [arXiv:hep-ph/9307208 \[hep-ph\]](#).
- [81] R. D. Young and A. W. Thomas, “Octet baryon masses and sigma terms from an SU(3) chiral extrapolation,” *Phys. Rev.* **D81** (2010) 014503, [arXiv:0901.3310 \[hep-lat\]](#).

- [82] **JLQCD** Collaboration, H. Ohki, K. Takeda, S. Aoki, S. Hashimoto, T. Kaneko, H. Matsufuru, J. Noaki, and T. Onogi, “Nucleon strange quark content from $N_f = 2 + 1$ lattice QCD with exact chiral symmetry,” *Phys. Rev. D* **D87** (2013) 034509, [arXiv:1208.4185 \[hep-lat\]](#).
- [83] M. A. Shifman, A. I. Vainshtein, and V. I. Zakharov, “Remarks on Higgs Boson Interactions with Nucleons,” *Phys. Lett.* **B78** (1978) 443.
- [84] J. F. Owens, A. Accardi, and W. Melnitchouk, “Global parton distributions with nuclear and finite- Q^2 corrections,” *Phys. Rev. D* **D87** no. 9, (2013) 094012, [arXiv:1212.1702 \[hep-ph\]](#).
- [85] J. Hisano, S. Matsumoto, M. M. Nojiri, and O. Saito, “Direct detection of the Wino and Higgsino-like neutralino dark matters at one-loop level,” *Phys. Rev. D* **D71** (2005) 015007, [arXiv:hep-ph/0407168 \[hep-ph\]](#).
- [86] R. J. Hill and M. P. Solon, “Universal behavior in the scattering of heavy, weakly interacting dark matter on nuclear targets,” *Phys. Lett.* **B707** (2012) 539–545, [arXiv:1111.0016 \[hep-ph\]](#).
- [87] M. Cirelli, A. Strumia, and M. Tamburini, “Cosmology and Astrophysics of Minimal Dark Matter,” *Nucl. Phys.* **B787** (2007) 152–175, [arXiv:0706.4071 \[hep-ph\]](#).
- [88] M. Fukugita and T. Yanagida, “Baryogenesis Without Grand Unification,” *Phys. Lett.* **B174** (1986) 45.
- [89] **ALEPH** Collaboration, A. Heister *et al.*, “Search for charginos nearly mass degenerate with the lightest neutralino in $e^+ e^-$ collisions at center-of-mass energies up to 209-GeV,” *Phys. Lett.* **B533** (2002) 223–236, [arXiv:hep-ex/0203020 \[hep-ex\]](#).
- [90] **ATLAS** Collaboration, G. Aad *et al.*, “Search for direct chargino production in anomaly-mediated supersymmetry breaking models based on a disappearing-track signature in pp collisions at $\sqrt{s} = 7$ TeV with the ATLAS detector,” *JHEP* **01** (2013) 131, [arXiv:1210.2852 \[hep-ex\]](#).
- [91] **DELPHI** Collaboration, J. Abdallah *et al.*, “Searches for supersymmetric particles in $e^+ e^-$ collisions up to 208-GeV and interpretation of the results within the MSSM,” *Eur. Phys. J.* **C31** (2003) 421–479, [arXiv:hep-ex/0311019 \[hep-ex\]](#).

- [92] **XENON100** Collaboration, E. Aprile *et al.*, “Dark Matter Results from 225 Live Days of XENON100 Data,” *Phys. Rev. Lett.* **109** (2012) 181301, [arXiv:1207.5988 \[astro-ph.CO\]](#).
- [93] **LUX** Collaboration, D. S. Akerib *et al.*, “First results from the LUX dark matter experiment at the Sanford Underground Research Facility,” *Phys. Rev. Lett.* **112** (2014) 091303, [arXiv:1310.8214 \[astro-ph.CO\]](#).
- [94] P. Cushman *et al.*, “Working Group Report: WIMP Dark Matter Direct Detection,” in *Community Summer Study 2013: Snowmass on the Mississippi (CSS2013) Minneapolis, MN, USA, July 29-August 6, 2013*. 2013. [arXiv:1310.8327 \[hep-ex\]](#).
<http://inspirehep.net/record/1262767/files/arXiv:1310.8327.pdf>.
- [95] **XENON1T** Collaboration, E. Aprile, “The XENON1T Dark Matter Search Experiment,” *Springer Proc. Phys.* **148** (2013) 93–96, [arXiv:1206.6288 \[astro-ph.IM\]](#).
- [96] C. E. Aalseth *et al.*, “The DarkSide Multiton Detector for the Direct Dark Matter Search,” *Adv. High Energy Phys.* **2015** (2015) 541362.
- [97] D. C. Malling *et al.*, “After LUX: The LZ Program,” [arXiv:1110.0103 \[astro-ph.IM\]](#).
- [98] **DARWIN Consortium** Collaboration, L. Baudis, “DARWIN: dark matter WIMP search with noble liquids,” *J. Phys. Conf. Ser.* **375** (2012) 012028, [arXiv:1201.2402 \[astro-ph.IM\]](#).
- [99] L. Bergstrom, J. Edsjo, and P. Ullio, “Cosmic anti-protons as a probe for supersymmetric dark matter?,” *Astrophys. J.* **526** (1999) 215–235, [arXiv:astro-ph/9902012 \[astro-ph\]](#).
- [100] T. Moroi and K. Nakayama, “Wino LSP detection in the light of recent Higgs searches at the LHC,” *Phys. Lett.* **B710** (2012) 159–163, [arXiv:1112.3123 \[hep-ph\]](#).
- [101] D. Hooper, C. Kelso, and F. S. Queiroz, “Stringent and Robust Constraints on the Dark Matter Annihilation Cross Section From the Region of the Galactic Center,” *Astropart. Phys.* **46** (2013) 55–70, [arXiv:1209.3015 \[astro-ph.HE\]](#).
- [102] **HESS** Collaboration, A. Abramowski *et al.*, “Search for Photon-Linelike Signatures from Dark Matter Annihilations with H.E.S.S.,” *Phys. Rev. Lett.* **110** (2013) 041301, [arXiv:1301.1173 \[astro-ph.HE\]](#).

- [103] T. Cohen, M. Lisanti, A. Pierce, and T. R. Slatyer, “Wino Dark Matter Under Siege,” *JCAP* **1310** (2013) 061, [arXiv:1307.4082](#).
- [104] J. Fan and M. Reece, “In Wino Veritas? Indirect Searches Shed Light on Neutralino Dark Matter,” *JHEP* **10** (2013) 124, [arXiv:1307.4400 \[hep-ph\]](#).
- [105] L. Gao, C. S. Frenk, A. Jenkins, V. Springel, and S. D. M. White, “Where will supersymmetric dark matter first be seen?,” *Mon. Not. Roy. Astron. Soc.* **419** (2012) 1721, [arXiv:1107.1916 \[astro-ph.CO\]](#).
- [106] M. Ackermann *et al.*, “Constraints on Dark Matter Annihilation in Clusters of Galaxies with the Fermi Large Area Telescope,” *JCAP* **1005** (2010) 025, [arXiv:1002.2239 \[astro-ph.CO\]](#).
- [107] **Fermi-LAT** Collaboration, A. A. Abdo *et al.*, “Constraints on Cosmological Dark Matter Annihilation from the Fermi-LAT Isotropic Diffuse Gamma-Ray Measurement,” *JCAP* **1004** (2010) 014, [arXiv:1002.4415 \[astro-ph.CO\]](#).
- [108] **Fermi-LAT** Collaboration, M. Ackermann *et al.*, “Dark matter constraints from observations of 25 Milky Way satellite galaxies with the Fermi Large Area Telescope,” *Phys. Rev.* **D89** (2014) 042001, [arXiv:1310.0828 \[astro-ph.HE\]](#).
- [109] **SDSS** Collaboration, D. G. York *et al.*, “The Sloan Digital Sky Survey: Technical Summary,” *Astron. J.* **120** (2000) 1579–1587, [arXiv:astro-ph/0006396 \[astro-ph\]](#).
- [110] X.-L. Chen and M. Kamionkowski, “Particle decays during the cosmic dark ages,” *Phys. Rev.* **D70** (2004) 043502, [arXiv:astro-ph/0310473 \[astro-ph\]](#).
- [111] N. Padmanabhan and D. P. Finkbeiner, “Detecting dark matter annihilation with CMB polarization: Signatures and experimental prospects,” *Phys. Rev.* **D72** (2005) 023508, [arXiv:astro-ph/0503486 \[astro-ph\]](#).
- [112] S. Galli, A. Melchiorri, G. F. Smoot, and O. Zahn, “From Cavendish to PLANCK: Constraining Newton’s Gravitational Constant with CMB Temperature and Polarization Anisotropy,” *Phys. Rev.* **D80** (2009) 023508, [arXiv:0905.1808 \[astro-ph.CO\]](#).
- [113] T. R. Slatyer, N. Padmanabhan, and D. P. Finkbeiner, “CMB Constraints on WIMP Annihilation: Energy Absorption During the Recombination Epoch,” *Phys. Rev.* **D80** (2009) 043526, [arXiv:0906.1197 \[astro-ph.CO\]](#).

- [114] D. P. Finkbeiner, S. Galli, T. Lin, and T. R. Slatyer, “Searching for Dark Matter in the CMB: A Compact Parameterization of Energy Injection from New Physics,” *Phys. Rev.* **D85** (2012) 043522, [arXiv:1109.6322](#) [[astro-ph.CO](#)].
- [115] G. Huetsi, A. Hektor, and M. Raidal, “Constraints on leptonically annihilating Dark Matter from reionization and extragalactic gamma background,” *Astron. Astrophys.* **505** (2009) 999–1005, [arXiv:0906.4550](#) [[astro-ph.CO](#)].
- [116] C. Evoli, S. Pandolfi, and A. Ferrara, “CMB constraints on light dark matter candidates,” *Mon. Not. Roy. Astron. Soc.* **433** (2013) 1736, [arXiv:1210.6845](#) [[astro-ph.CO](#)].
- [117] S. Galli, T. R. Slatyer, M. Valdes, and F. Iocco, “Systematic Uncertainties In Constraining Dark Matter Annihilation From The Cosmic Microwave Background,” *Phys. Rev.* **D88** (2013) 063502, [arXiv:1306.0563](#) [[astro-ph.CO](#)].
- [118] S. Seager, D. D. Sasselov, and D. Scott, “A New Calculation of the Recombination Epoch,” *Astrophysical Journal Letters* **523** (Sept., 1999) L1–L5, [astro-ph/9909275](#).
- [119] S. Galli, F. Iocco, G. Bertone, and A. Melchiorri, “Updated CMB constraints on Dark Matter annihilation cross-sections,” *Phys. Rev.* **D84** (2011) 027302, [arXiv:1106.1528](#) [[astro-ph.CO](#)].
- [120] M. Kawasaki, K. Kohri, T. Moroi, and Y. Takaesu, “Revisiting Big-Bang Nucleosynthesis Constraints on Dark-Matter Annihilation,” *Phys. Lett.* **B751** (2015) 246–250, [arXiv:1509.03665](#) [[hep-ph](#)].
- [121] R. Cooke, M. Pettini, R. A. Jorgenson, M. T. Murphy, and C. C. Steidel, “Precision measures of the primordial abundance of deuterium,” *Astrophys. J.* **781** no. 1, (2014) 31, [arXiv:1308.3240](#) [[astro-ph.CO](#)].
- [122] E. Aver, K. A. Olive, and E. D. Skillman, “The effects of He I λ 10830 on helium abundance determinations,” *JCAP* **1507** no. 07, (2015) 011, [arXiv:1503.08146](#) [[astro-ph.CO](#)].
- [123] J. Geiss and G. Gloeckler, “Isotopic Composition of H, HE and NE in the Protosolar Cloud,” *Space Science Reviews* **106** (2003) 3–18.

- [124] J. Hisano, M. Kawasaki, K. Kohri, T. Moroi, and K. Nakayama, “Cosmic Rays from Dark Matter Annihilation and Big-Bang Nucleosynthesis,” *Phys. Rev.* **D79** (2009) 083522, [arXiv:0901.3582 \[hep-ph\]](#).
- [125] L. Sbordone *et al.*, “The metal-poor end of the Spite plateau. 1: Stellar parameters, metallicities and lithium abundances,” *Astron. Astrophys.* **522** (2010) A26, [arXiv:1003.4510 \[astro-ph.GA\]](#).
- [126] B. Henning, X. Lu, and H. Murayama, “How to use the Standard Model effective field theory,” [arXiv:1412.1837 \[hep-ph\]](#).
- [127] M. Baak *et al.*, “Working Group Report: Precision Study of Electroweak Interactions,” in *Community Summer Study 2013: Snowmass on the Mississippi (CSS2013) Minneapolis, MN, USA, July 29-August 6, 2013*. 2013. [arXiv:1310.6708 \[hep-ph\]](#). <http://www.slac.stanford.edu/econf/C1307292/docs/EnergyFrontier/Electroweak-19.pdf>.
- [128] M. E. Peskin and T. Takeuchi, “Estimation of oblique electroweak corrections,” *Phys. Rev.* **D46** (1992) 381–409.
- [129] I. Maksymyk, C. P. Burgess, and D. London, “Beyond S, T and U,” *Phys. Rev.* **D50** (1994) 529–535, [arXiv:hep-ph/9306267 \[hep-ph\]](#).
- [130] R. Barbieri, A. Pomarol, R. Rattazzi, and A. Strumia, “Electroweak symmetry breaking after LEP-1 and LEP-2,” *Nucl. Phys.* **B703** (2004) 127–146, [arXiv:hep-ph/0405040 \[hep-ph\]](#).
- [131] S. P. Martin, K. Tobe, and J. D. Wells, “Virtual effects of light gauginos and higgsinos: A Precision electroweak analysis of split supersymmetry,” *Phys. Rev.* **D71** (2005) 073014, [arXiv:hep-ph/0412424 \[hep-ph\]](#).
- [132] T. Behnke, J. E. Brau, B. Foster, J. Fuster, M. Harrison, J. M. Paterson, M. Peskin, M. Stanitzki, N. Walker, and H. Yamamoto, “The International Linear Collider Technical Design Report - Volume 1: Exefcutive Summary,” [arXiv:1306.6327 \[physics.acc-ph\]](#).
- [133] H. Baer, T. Barklow, K. Fujii, Y. Gao, A. Hoang, S. Kanemura, J. List, H. E. Logan, A. Nomerotski, M. Perelstein, *et al.*, “The International Linear Collider Technical Design Report - Volume 2: Physics,” [arXiv:1306.6352 \[hep-ph\]](#).
- [134] C. Adolphsen, M. Barone, B. Barish, K. Buesser, P. Burrows, J. Carwardine, J. Clark, H. M. Durand, G. Dugan, E. Elsen, *et al.*, “The International

Linear Collider Technical Design Report - Volume 3.I: Accelerator & in the Technical Design Phase,” [arXiv:1306.6353](#) [[physics.acc-ph](#)].

- [135] C. Adolphsen, M. Barone, B. Barish, K. Buesser, P. Burrows, J. Carwardine, J. Clark, H. M. Durand, G. Dugan, E. Elsen, *et al.*, “The International Linear Collider Technical Design Report - Volume 3.II: Accelerator Baseline Design,” [arXiv:1306.6328](#) [[physics.acc-ph](#)].
- [136] H. Abramowicz *et al.*, “The International Linear Collider Technical Design Report - Volume 4: Detectors,” [arXiv:1306.6329](#) [[physics.ins-det](#)].
- [137] A. Lorca and T. Riemann, “An Integrated tool for loop calculations: aITALC,” *Comput. Phys. Commun.* **174** (2006) 71–82, [arXiv:hep-ph/0412047](#) [[hep-ph](#)].
- [138] P. Nogueira, “Automatic Feynman graph generation,” *J. Comput. Phys.* **105** (1993) 279–289.
- [139] M. Tentyukov and J. Fleischer, “A Feynman diagram analyzer DIANA,” *Comput. Phys. Commun.* **132** (2000) 124–141, [arXiv:hep-ph/9904258](#) [[hep-ph](#)].
- [140] J. A. M. Vermaseren, “New features of FORM,” [arXiv:math-ph/0010025](#) [[math-ph](#)].
- [141] T. Hahn and M. Perez-Victoria, “Automatized one loop calculations in four-dimensions and D-dimensions,” *Comput. Phys. Commun.* **118** (1999) 153–165, [arXiv:hep-ph/9807565](#) [[hep-ph](#)].
- [142] G. J. van Oldenborgh, “FF: A Package to evaluate one loop Feynman diagrams,” *Comput. Phys. Commun.* **66** (1991) 1–15.
- [143] M. Cirelli, N. Fornengo, and A. Strumia, “Minimal dark matter,” *Nucl. Phys.* **B753** (2006) 178–194, [arXiv:hep-ph/0512090](#) [[hep-ph](#)].
- [144] M. Cirelli and A. Strumia, “Minimal Dark Matter: Model and results,” *New J. Phys.* **11** (2009) 105005, [arXiv:0903.3381](#) [[hep-ph](#)].
- [145] **CALET** Collaboration, S. Torii, “Calorimetric electron telescope mission. Search for dark matter and nearby sources,” *Nucl. Instrum. Meth.* **A630** (2011) 55–57.
- [146] see the website <http://dpnc.unige.ch/dampe/> and the conference talks of ICRC2015.

- [147] **HESS** Collaboration, J. A. Hinton, “The Status of the H.E.S.S. project,” *New Astron. Rev.* **48** (2004) 331–337, [arXiv:astro-ph/0403052](#) [astro-ph].
- [148] A. J. Smith, “HAWC: Design, Operation, Reconstruction and Analysis,” in *Proceedings, 34th International Cosmic Ray Conference (ICRC 2015)*. 2015. [arXiv:1508.05826](#) [astro-ph.IM].
<http://inspirehep.net/record/1389748/files/arXiv:1508.05826.pdf>.
- [149] **CTA Consortium** Collaboration, M. Actis *et al.*, “Design concepts for the Cherenkov Telescope Array CTA: An advanced facility for ground-based high-energy gamma-ray astronomy,” *Exper. Astron.* **32** (2011) 193–316, [arXiv:1008.3703](#) [astro-ph.IM].
- [150] A. M. Galper *et al.*, “Status of the GAMMA-400 Project,” *Adv. Space Res.* **51** (2013) 297–300, [arXiv:1201.2490](#) [astro-ph.IM].
- [151] X. Wu, M. Su, A. Bravar, J. Chang, Y. Fan, M. Pohl, and R. Walter, “PANGU: A High Resolution Gamma-ray Space Telescope,” *Proc. SPIE Int. Soc. Opt. Eng.* **9144** (2014) 91440F, [arXiv:1407.0710](#) [astro-ph.IM].
- [152] see the website: <http://herd.ihep.ac.cn/>.
- [153] **CTA Consortium** Collaboration, J. Carr *et al.*, “Prospects for Indirect Dark Matter Searches with the Cherenkov Telescope Array (CTA),” in *Proceedings, 34th International Cosmic Ray Conference (ICRC 2015)*. 2015. [arXiv:1508.06128](#) [astro-ph.HE].
<http://inspirehep.net/record/1389681/files/arXiv:1508.06128.pdf>.
- [154] see the website: <http://www.skatelescope.org/>.
- [155] T. Takahashi *et al.*, “The ASTRO-H X-ray Observatory,” *Proc. SPIE Int. Soc. Opt. Eng.* **8443** (2012) 1Z, [arXiv:1210.4378](#) [astro-ph.IM].
- [156] G. Beck and S. Colafrancesco, “A Multi-frequency analysis of dark matter annihilation interpretations of recent anti-particle and gamma-ray excesses in cosmic structures,” [arXiv:1508.01386](#) [astro-ph.CO].
- [157] J. A. R. Cembranos, A. de la Cruz-Dombriz, V. Gammaldi, R. A. Lineros, and A. L. Maroto, “Reliability of Monte Carlo event generators for gamma ray dark matter searches,” *JHEP* **09** (2013) 077, [arXiv:1305.2124](#) [hep-ph].
- [158] L. Hernquist, “An Analytical Model for Spherical Galaxies and Bulges,” *Astrophys. J.* **356** (1990) 359.

- [159] J. F. Navarro, C. S. Frenk, and S. D. M. White, “A Universal density profile from hierarchical clustering,” *Astrophys. J.* **490** (1997) 493–508, [arXiv:astro-ph/9611107](#) [astro-ph].
- [160] M. G. Walker and J. Penarrubia, “A Method for Measuring (Slopes of) the Mass Profiles of Dwarf Spheroidal Galaxies,” *Astrophys. J.* **742** (2011) 20, [arXiv:1108.2404](#) [astro-ph.CO].
- [161] A. Burkert, “The Structure of dark matter halos in dwarf galaxies,” *IAU Symp.* **171** (1996) 175, [arXiv:astro-ph/9504041](#) [astro-ph]. [Astrophys. J.447,L25(1995)].
- [162] A. Charbonnier *et al.*, “Dark matter profiles and annihilation in dwarf spheroidal galaxies: prospectives for present and future gamma-ray observatories - I. The classical dSphs,” *Mon. Not. Roy. Astron. Soc.* **418** (2011) 1526–1556, [arXiv:1104.0412](#) [astro-ph.HE].
- [163] J. S. Bullock, T. S. Kolatt, Y. Sigad, R. S. Somerville, A. V. Kravtsov, A. A. Klypin, J. R. Primack, and A. Dekel, “Profiles of dark haloes. Evolution, scatter, and environment,” *Mon. Not. Roy. Astron. Soc.* **321** (2001) 559–575, [arXiv:astro-ph/9908159](#) [astro-ph].
- [164] G. D. Martinez, “A robust determination of Milky Way satellite properties using hierarchical mass modelling,” *Mon. Not. Roy. Astron. Soc.* **451** no. 3, (2015) 2524–2535, [arXiv:1309.2641](#) [astro-ph.GA].
- [165] J. Wolf, G. D. Martinez, J. S. Bullock, M. Kaplinghat, M. Geha, R. R. Munoz, J. D. Simon, and F. F. Avedo, “Accurate Masses for Dispersion-supported Galaxies,” *Mon. Not. Roy. Astron. Soc.* **406** (2010) 1220, [arXiv:0908.2995](#) [astro-ph.CO].
- [166] R. R. Munoz, P. M. Frinchaboy, S. R. Majewski, J. R. Kuhn, M.-Y. Chou, C. Palma, S. T. Sohn, R. J. Patterson, and M. H. Siegel, “Exploring halo substructure with giant stars. 8. The Velocity dispersion profiles of the Ursa Minor and Draco dwarf spheroidals at large angular separations,” *Astrophys. J.* **631** (2005) L137–L142, [arXiv:astro-ph/0504035](#) [astro-ph].
- [167] M. G. Walker, M. Mateo, and E. Olszewski, “Stellar Velocities in the Carina, Fornax, Sculptor and Sextans dSph Galaxies: Data from the Magellan/MMFS Survey,” *Astron. J.* **137** (2009) 3100, [arXiv:0811.0118](#) [astro-ph].

- [168] V. Bonnavard *et al.*, “Dark matter annihilation and decay in dwarf spheroidal galaxies: The classical and ultrafaint dSphs,” *Mon. Not. Roy. Astron. Soc.* **453** no. 1, (2015) 849–867, [arXiv:1504.02048](#) [astro-ph.HE].
- [169] G. D. Martinez, J. S. Bullock, M. Kaplinghat, L. E. Strigari, and R. Trotta, “Indirect Dark Matter Detection from Dwarf Satellites: Joint Expectations from Astrophysics and Supersymmetry,” *JCAP* **0906** (2009) 014, [arXiv:0902.4715](#) [astro-ph.HE].
- [170] V. Springel, J. Wang, M. Vogelsberger, A. Ludlow, A. Jenkins, A. Helmi, J. F. Navarro, C. S. Frenk, and S. D. M. White, “The Aquarius Project: the subhalos of galactic halos,” *Mon. Not. Roy. Astron. Soc.* **391** (2008) 1685–1711, [arXiv:0809.0898](#) [astro-ph].
- [171] J. D. Simon *et al.*, “A Complete Spectroscopic Survey of the Milky Way Satellite Segue 1: The Darkest Galaxy,” *Astrophys. J.* **733** (2011) 46, [arXiv:1007.4198](#) [astro-ph.GA].
- [172] J. D. Simon and M. Geha, “The Kinematics of the Ultra-Faint Milky Way Satellites: Solving the Missing Satellite Problem,” *Astrophys. J.* **670** (2007) 313–331, [arXiv:0706.0516](#) [astro-ph].
- [173] B. Willman, M. Geha, J. Strader, L. E. Strigari, J. D. Simon, E. Kirby, and A. Warres, “Willman 1 - a probable dwarf galaxy with an irregular kinematic distribution,” *Astron. J.* **142** (2011) 128, [arXiv:1007.3499](#) [astro-ph.GA].
- [174] M. Su, T. R. Slatyer, and D. P. Finkbeiner, “Giant Gamma-ray Bubbles from Fermi-LAT: AGN Activity or Bipolar Galactic Wind?,” *Astrophys. J.* **724** (2010) 1044–1082, [arXiv:1005.5480](#) [astro-ph.HE].
- [175] E. Berkhuijsen, C. Haslam, and C. Salter *Astron. Astrophys.* **14** (1971) 252.
- [176] Here is the web site. See also A. E. Vladimirov, S. W. Digel, G. Johannesson, P. F. Michelson, I. V. Moskalenko, P. L. Nolan, E. Orlando and T. A. Porter *et al.*, *Comput. Phys. Commun.* **182**, 1156 (2011) [[arXiv:1008.3642](#) [astro-ph.HE]], and references therein.
- [177] **Fermi-LAT** Collaboration, A. A. Abdo *et al.*, “The Spectrum of the Isotropic Diffuse Gamma-Ray Emission Derived From First-Year Fermi Large Area Telescope Data,” *Phys. Rev. Lett.* **104** (2010) 101101, [arXiv:1002.3603](#) [astro-ph.HE].
- [178] See <http://fermi.gsfc.nasa.gov/ssc/data/access/lat/BackgroundModels.html>.

- [179] **Fermi-LAT** Collaboration, M. Ackermann *et al.*, “The Fermi Large Area Telescope On Orbit: Event Classification, Instrument Response Functions, and Calibration,” *Astrophys. J. Suppl.* **203** (2012) 4, arXiv:1206.1896 [astro-ph.IM].
- [180] **Fermi-LAT** Collaboration, J. Bregeon, E. Charles, and M. Wood, “Fermi-LAT data reprocessed with updated calibration constants,” 2013. arXiv:1304.5456 [astro-ph.HE].
- [181] I. Cholis and P. Salucci, “Extracting limits on Dark Matter annihilation from gamma-ray observations towards dwarf spheroidal galaxies,” *Phys. Rev.* **D86** (2012) 023528, arXiv:1203.2954 [astro-ph.HE].
- [182] **Fermi-LAT** Collaboration, W. B. Atwood *et al.*, “The Large Area Telescope on the Fermi Gamma-ray Space Telescope Mission,” *Astrophys. J.* **697** (2009) 1071–1102, arXiv:0902.1089 [astro-ph.IM].
- [183] **MAGIC** Collaboration, J. Cortina, F. Goebel, and T. Schweizer, “Technical Performance of the MAGIC Telescopes,” arXiv:0907.1211 [astro-ph.IM].
- [184] **VERITAS** Collaboration, J. S. Perkins and G. Maier, “VERITAS Telescope 1 Relocation: Details and Improvements,” arXiv:0912.3841 [astro-ph.IM].
- [185] See the performance page.
- [186] P. Cumani, “TeV particle astrophysics 2013.” The reference slide can be found here.
- [187] S. Baker and R. D. Cousins, “Clarification of the Use of Chi Square and Likelihood Functions in Fits to Histograms,” *Nucl. Instrum. Meth.* **221** (1984) 437–442.
- [188] C. He, K. Bechtol, A. P. Hearin, and D. Hooper, “Prospects for detecting gamma rays from annihilating dark matter in dwarf galaxies in the era of the Dark Energy Survey and Large Synoptic Survey Telescope,” *Phys. Rev.* **D91** no. 6, (2015) 063515, arXiv:1309.4780 [astro-ph.HE].
- [189] L. Baldini, “The Large Area Telescope in the context of the extended Fermi mission,” *Nucl. Phys. Proc. Suppl.* **243-244** (2013) 125–130.
- [190] **PFS Team** Collaboration, R. Ellis *et al.*, “Extragalactic science, cosmology, and Galactic archaeology with the Subaru Prime Focus Spectrograph,” *Publ. Astron. Soc. Jap.* **66** no. 1, (2014) R1, arXiv:1206.0737 [astro-ph.CO].

- [191] S. M. Faber *et al.*, “The DEIMOS spectrograph for the Keck II Telescope: integration and testing,” *Proc. SPIE Int. Soc. Opt. Eng.* **4841** (1969) 1657–1669.
- [192] J. Binney and S. Tremaine, *Galactic Dynamics: Second Edition*. Princeton University Press, 2008.
- [193] M. Baes and E. Van Hese, “Dynamical models with a general anisotropy profile,” *Astron. Astrophys.* **471** (2007) 419, [arXiv:0705.4109 \[astro-ph\]](#).
- [194] P. Ullio, “TeV particle astrophysics 2015.” The talk slide can be found here.
- [195] A. Geringer-Sameth, S. M. Koushiappas, and M. Walker, “Dwarf galaxy annihilation and decay emission profiles for dark matter experiments,” *Astrophys. J.* **801** no. 2, (2015) 74, [arXiv:1408.0002 \[astro-ph.CO\]](#).
- [196] K. Hayashi, K. Ichikawa, S. Matsumoto, M. Ibe, M. N. Ishigaki, and H. Sugai in preparation.
- [197] V. Bonnivard, D. Maurin, and M. G. Walker, “Sensitivity to interlopers in stellar-kinematic samples for ultrafaint dwarf galaxies: Uncertainty about the dark matter annihilation profile of Segue I,” [arXiv:1506.08209 \[astro-ph.GA\]](#).
- [198] H. C. Plummer, “On the problem of distribution in globular star clusters,” *Mon. Not. Roy. Astron. Soc.* **71** (Mar., 1911) 460–470.
- [199] A. W. McConnachie, “The observed properties of dwarf galaxies in and around the Local Group,” *Astron. J.* **144** (2012) 4, [arXiv:1204.1562 \[astro-ph.CO\]](#).
- [200] A. Bressan, P. Marigo, L. Girardi, B. Salasnich, C. Dal Cero, S. Rubele, and A. Nanni, “PARSEC: stellar tracks and isochrones with the PAdova and TRieste Stellar Evolution Code,” *MNRAS* **427** (2012) 127, [arXiv:1208.4498 \[astro-ph\]](#).
- [201] E. N. Kirby, G. A. Lanfranchi, J. D. Simon, J. G. Cohen, and P. Guhathakurta, “Multi-element Abundance Measurements from Medium-resolution Spectra. III. Metallicity Distributions of Milky Way Dwarf Satellite Galaxies,” *ApJ* **727** (2011) 78, [arXiv:1011.4937 \[astro-ph\]](#).
- [202] A. W. McConnachie, “The Observed Properties of Dwarf Galaxies in and around the Local Group,” *AJ* **144** (2012) 4, [arXiv:1204.1562 \[astro-ph\]](#).
- [203] P. Cuddeford, “An analytic inversion for anisotropic spherical galaxies,” *Mon. Not. Roy. Astron. Soc.* **253** (Dec., 1991) 414–426.

- [204] M. G. Walker, E. W. Olszewski, and M. Mateo, “Bayesian analysis of resolved stellar spectra: application to MMT/Hectochelle observations of the Draco dwarf spheroidal,” *Mon. Not. Roy. Astron. Soc.* **448** (Apr., 2015) 2717–2732, [arXiv:1503.02589](#).
- [205] A. C. Robin, C. Reyle, S. Derriere, and S. Picaud, “A Synthetic view on structure and evolution of the Milky Way,” *Astron. Astrophys.* **409** (2003) 523, [arXiv:astro-ph/0401052](#) [astro-ph].
- [206] R. P. van der Marel, “Velocity Profiles of Galaxies with Claimed Black-Holes - Part Three - Observations and Models for M87,” *Mon. Not. Roy. Astron. Soc.* **270** (Sept., 1994) 271.
- [207] G. A. Mamon and E. L. Lokas, “Dark matter in elliptical galaxies - II. Estimating the mass within the virial radius,” *Mon. Not. Roy. Astron. Soc.* **363** (Nov., 2005) 705–722, [astro-ph/0405491](#).
- [208] N. Metropolis, A. W. Rosenbluth, M. N. Rosenbluth, A. H. Teller, and E. Teller, “Equation of state calculations by fast computing machines,” *J. Chem. Phys.* **21** (1953) 1087–1092.
- [209] W. K. Hastings, “Monte Carlo Sampling Methods Using Markov Chains and Their Applications,” *Biometrika* **57** (1970) 97–109.